

# Contents

2	<b>1 Introduction</b>	<b>3</b>
3	<b>2 Pixel detectors</b>	<b>5</b>
4	2.1 Signal formation . . . . .	5
5	2.2 Charge Coupled Devices . . . . .	7
6	2.3 Hybrid pixels . . . . .	7
7	2.4 CMOS MAPS and DMPAS . . . . .	9
8	2.4.1 DMAPS: large and small fill factor . . . . .	10
9	2.4.2 A modified sensor . . . . .	11
10	2.5 Analog front end . . . . .	13
11	2.5.1 Preamplifier . . . . .	13
12	2.6 Readout logic . . . . .	14
13	<b>3 Use of pixel detectors</b>	<b>17</b>
14	3.1 Tracking in HEP . . . . .	17
15	3.1.1 Hybrid pixels at LHC and at SuperKEKB . . . . .	18
16	3.1.2 First attempts to MAPS . . . . .	21
17	3.2 Other applications . . . . .	23
18	3.2.1 Applicability to FLASH radiotherapy . . . . .	24
19	<b>4 TJ-Monopix1</b>	<b>29</b>
20	4.1 The sensor . . . . .	30
21	4.2 Front end . . . . .	32
22	4.2.1 ALPIDE-like . . . . .	33
23	4.3 Readout logic . . . . .	34
24	<b>5 Arcadia-MD1</b>	<b>38</b>
25	5.1 The sensor . . . . .	38
26	5.1.1 Two different FE flavor . . . . .	39
27	5.2 Readout logic and data structure . . . . .	39
28	5.2.1 Matrix division and data-packets . . . . .	39
29	<b>6 Characterization</b>	<b>43</b>
30	6.1 TJ-Monopix1 characterization . . . . .	43
31	6.1.1 Threshold and noise: figure of merit for pixel detectors . . . . .	43
32	6.1.2 Linearity of the ToT . . . . .	47
33	6.1.3 Calibration of the ToT . . . . .	48
34	6.1.4 Changing the bias . . . . .	52

35	6.1.5 Measurements with radioactive sources . . . . .	53
36	6.1.6 Dead time measurements . . . . .	56
37	6.2 ARCADIA-MD1 characterization . . . . .	57
38	<b>7 Test beam measurements</b>	<b>62</b>
39	7.1 Apparatus description . . . . .	62
40	7.1.1 Accelerator . . . . .	63
41	7.1.2 Mechanical carriers . . . . .	64
42	7.2 Measurements . . . . .	64
43	7.2.1 MIP spectrum using cosmic rays as source . . . . .	69
44	<b>A Pixels detector: a brief overview</b>	<b>70</b>
45	A.1 Radiation damages . . . . .	70
46	<b>Bibliography</b>	<b>73</b>
47	Characterization of monolithic CMOS pixel sensors for charged particle detectors and	
48	for high intensity dosimetry	

<sup>49</sup> **Chapter 1**

<sup>50</sup> **Introduction**

<sup>51</sup> Since the 1980s, when the fabrication of device with very small electrodes (50-100  $\mu\text{m}$ )  
<sup>52</sup> became a practical possibility, pixel detectors have been widely employed for imaging and  
<sup>53</sup> tracking charged particles in the vertex region of experiments at accelerators. Thanks to  
<sup>54</sup> their excellent spatial resolution, today even better than 10  $\mu\text{m}$ , they allow for true three  
<sup>55</sup> dimensional space-point determination even at high particle fluxes and in particular for  
<sup>56</sup> the identification of secondary vertices of short-lived particles such as  $\tau$  and B mesons.  
<sup>57</sup> Requirement imposed by accelerators are stringent and they will become even more so  
<sup>58</sup> with the increase of luminosity; in this scenario CMOS Monolithic Active Pixel Sensors  
<sup>59</sup> (MAPS), based on the technology of CMOS cameras, are being developed to improve  
<sup>60</sup> the performance of the hybrid pixel detectors, which currently constitute the state-of-art  
<sup>61</sup> for large scale pixel detector, in particular by reducing the amount of material, power  
<sup>62</sup> consumption and pixel dimension. Indeed, while hybrid pixels are made by two parts, the  
<sup>63</sup> sensor and the electronics, welded together through microconnections, the MAPS integrate  
<sup>64</sup> them all on the same wafer.

<sup>65</sup> Experiments such as ALICE at LHC and STAR at RHIC have already introduced the  
<sup>66</sup> CMOS MAPS technology in their detectors. ALICE Tracking System (ITS2), upgraded  
<sup>67</sup> during the LHC long shut down in 2019-20, was the first large-area ( $\sim 10 \text{ m}^2$ ) silicon vertex  
<sup>68</sup> detector based on CMOS MAPS. Thanks to the reduction of the material budget, ITS2,  
<sup>69</sup> which uses the ALPIDE chip developed by ALICE collaboration, obtained an amazing im-  
<sup>70</sup> provement both in the position measurement and in the momentum resolution, improving  
<sup>71</sup> the efficiency of track reconstruction for particle with very low transverse momentum (by  
<sup>72</sup> a factor 6 at  $p_T \sim 0.1 \text{ GeV}/c$ ). Further advancements in CMOS MAPS technology are  
<sup>73</sup> being aggressively pursued for the ALICE ITS3 and the Belle II vertex detector upgrades  
<sup>74</sup> (both foreseen around 2026-27), and by the R&D53 collaboration for the upgrade at HL-  
<sup>75</sup> LHC, with the goals of further reducing the sensor thickness and improving the readout  
<sup>76</sup> speed of the devices, while keeping power consumption at a minimum.

<sup>77</sup> Beside tracking, the development of pixel detectors is a very active field with many  
<sup>78</sup> applications: a noteworthy example of detector originally used in particle physics and later  
<sup>79</sup> employed for medical imaging, in space detectors and for art authentication, is Medipix,  
<sup>80</sup> a hybrid system developed at CERN within the Medipix collaboration. Among medical  
<sup>81</sup> applications, a possible use of CMOS MAPS could be in dosimetry: in the last few years  
<sup>82</sup> the search of radiotherapy oncological treatments with high intensity beams (FLASH  
<sup>83</sup> mode) is requiring new dosimeters, both for the therapies as well as new beam-monitors  
<sup>84</sup> (especially for focused very high energy electron beams), which are capable of deal with

85 extreme dose rate (up to 40 Gy/s).

86 I have studied the characteristics of two ALPIDE-like CMOS MAPS chips and tested  
87 them under different front end configuration. The first chip, the TJ-Monopix1 from the  
88 Monopix series, is a TowerJazz MAPS fabricated in 180 nm CMOS technology with an  
89 active area of  $1 \times 2 \text{ cm}^2$  (448×224 pixels) and is one of the prototypes for the Belle II vertex  
90 detector upgrade. The second chip, called Main Demonstrator-1, has an active area of  
91  $1.28 \times 1.28 \text{ cm}^2$  (512×512 pixels) is produced by LFoundry in 110 nm CMOS technology  
92 and designed by the ARCADIA (Advanced Readout CMOS Architectures with Depleted  
93 Integrated sensor Arrays) group; it is intended to be a general purpose device with possible  
94 use in medical scanners, space experiments, future lepton colliders and also possibly X-ray  
95 applications with thick substrates. The main differences between the two chips are in the  
96 output signal type and in the readout sequence of the matrix. Concerning the former,  
97 TJ-Monopix1 returns an analog output information, that is the time over threshold of the  
98 pulse, which can be related with the charge released by the particle in the sensor, while  
99 MD1 returns only a digital information; regarding the latter, instead, TJ-Monopix1 has  
100 a completely sequential readout, while MD1 roughly combines the information of the hits  
101 before the readout in order to reduce the data transmission time.

102 I have set up the test systems for the two chips in the INFN clean laboratories and char-  
103 acterized the devices electrically and with radioactive sources in terms of threshold, noise,  
104 dead time and analog response. The mean minimum stable threshold evolved through  
105 different generation of chips and nowadays it is less than  $500 \text{ e}^-$ , allowing thinner sensors  
106 with smaller signals: TJ-Monopix1 has proven to be in agreement with this trend, having  
107 a threshold of  $\sim 400 \text{ e}^-$ , to be compared with the  $2000 \text{ e}^-$  signal expected for a minimum  
108 ionizing particle in an epitaxial layer of  $25 \mu\text{m}$ . Moreover, since one of the main challenges  
109 of MAPS are the differences between pixels due to process parameters variation across  
110 the wafer, which make the sensor response nonuniform, I have measured the threshold  
111 and noise dispersion across the matrix, which I found to be  $40 \text{ e}^-$  and  $2 \text{ e}^-$  respectively. I  
112 have also studied the response of the analog signal recorded by TJ-Monopix1, that is the  
113 time over threshold, and performed a calibration of its absolute value using a Fe55 X-ray  
114 source. All these measurements are important to verify the design parameters of the chip  
115 and to validate the chip simulation.

116 As conclusion of the measurement campaign, we have tested TJ-Monopix1 at very  
117 high intensity using the electron beam of the new ElectronFlash accelerator designed for  
118 both medical research and R&D in FLASH-radiotherapy and recently installed at Santa  
119 Chiara hospital in Pisa. I have participated in the design of the setup needed for testbeam  
120 measurement and I am currently working on the analysis of the data collected.

<sub>121</sub> **Chapter 2**

<sub>122</sub> **Pixel detectors**

<sub>123</sub> Pixel detectors are semiconductor detectors which are segmented in two dimensions: this  
<sub>124</sub> distinguish them from the strip detectors, such that a single plane of detector already  
<sub>125</sub> provides both the coordinates of impact of the detected particle. Their operation is based  
<sub>126</sub> on the p-n junction (fig. 2.1). A p-n junction is built by bringing in contact two n  
<sub>127</sub> and p doped silicon crystals. At the boundary, recombination of both charge carriers  
<sub>128</sub> occurs forming a region, the depletion zone, which is free of charge carriers. The charged  
<sub>129</sub> donors<sup>+</sup> and acceptor<sup>-</sup>, that remain ionised in the n-type and p-type regions, features a  
<sub>130</sub> space charge and create an electric field across the junction, causing a drift current in the  
<sub>131</sub> opposite direction to the diffusion one, through which the junction reaches an equilibrium  
<sub>132</sub> state. Assuming a constant space change, the electric field is linear and reach a maximum  
<sub>133</sub> at the boundary of the *p* and *n* layers.

<sub>134</sub> **2.1 Signal formation**

<sub>135</sub> When a charged particle passes through a pixel and loses energy by ionization only a  
<sub>136</sub> part of that energy is used to generate electron-hole pairs, since another part is used for  
<sub>137</sub> other processes, as lattice excitation. The average energy needed to create a pair at 300 K  
<sub>138</sub> in silicon is  $w_i = 3.65 \text{ eV}$ , that is more than the mean ionization energy because of the  
<sub>139</sub> interactions with phonon, since for a minimum ionizing particle (MIP) the most probable  
<sub>140</sub> value (MPV) of charge released in the semiconductor is  $0.28 \text{ keV}/\mu\text{m}$ , hence the number  
<sub>141</sub> of electrons-vacuum pairs is:

$$\langle \frac{dE}{dx} \rangle \frac{1}{w_i} \sim 80 \text{ e/h} \sim \frac{1.28 \cdot 10^{-2} fC}{\mu\text{m}} \quad (2.1)$$

<sub>142</sub> Because of the splitting of the energy depositon between the two different processes, the  
<sub>143</sub> number  $N_{e/h}$  of couples generated undergoes fluctuations that usually follow a Poisson  
<sub>144</sub> distribution; thus the fluctuations of  $N_{e/h}$  is equal to  $\sigma_{e/h} = \sqrt{N_{e/h}}$ . Under the constraint  
<sub>145</sub> of complete absorption of a particle, the energy resolution improves of a factor  $\sqrt{F}$ , where  
<sub>146</sub> F is called the Fano factor and determines the ultimate limit of energy resolution for  
<sub>147</sub> semiconductors. F is a function of the material and temperature and for silicon is equal  
<sub>148</sub> to  $\sim 0.115$ .

<sub>149</sub> In order to avoid a loss signal, it is fundamental that pairs e/h are produced in the  
<sub>150</sub> depleted region of the semiconductor, where the probability of recombination with charge  
<sub>151</sub> carriers is low. For this reason pixel detectors are commonly reverse biased: a positive  
<sub>152</sub> bias is given to the *n* electrode and a negative to the *p* in order to grow the depletion zone

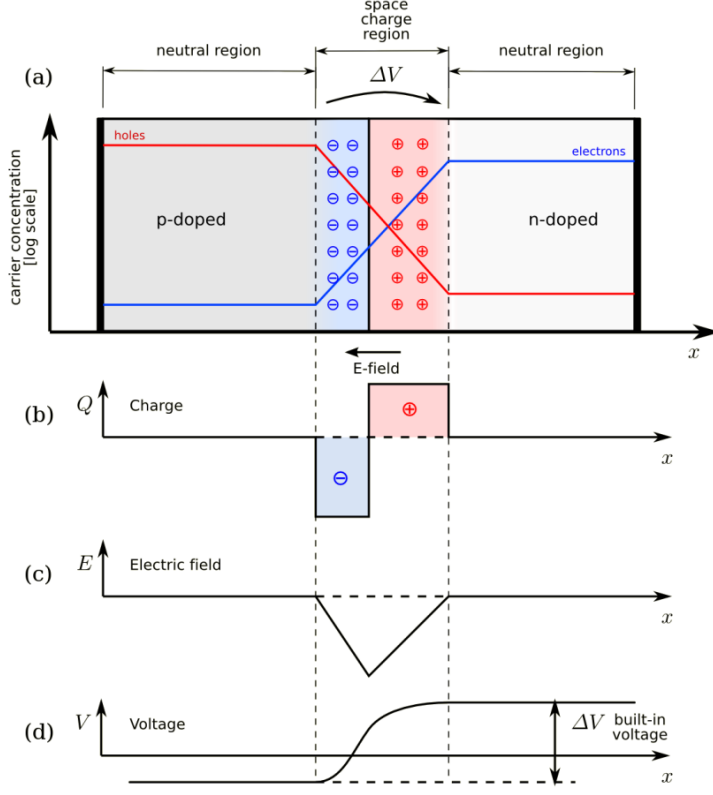


Figure 2.1: The structure of a p-n junction. (a) structure, (b) space charge density, (c) electric field distribution and (d) potential distribution.

in the epitaxial layer within the bulk. The width of the depletion region depends on the external bias  $V_{ext}$ , the resistivity  $\rho$  and also with the dopant:

$$d_n \sim 0.55 \sqrt{\frac{\rho}{\Omega cm} \frac{V_{ext}}{V}} \mu m \quad d_p \sim 0.32 \sqrt{\frac{\rho}{\Omega cm} \frac{V_{ext}}{V}} \mu m \quad (2.2)$$

Thus, high resistivity wafers ( $100 \Omega cm - k\Omega cm$ ) are typically preferred because they allow bigger depletion zone with smaller voltage bias.

The charges created within the sensor are separated by an electric field and collected at their respective electrodes ( $p$  for holes and  $n$  for electrons)<sup>1</sup>; by the drift of these charges, a signal  $i_e$  is generated on the electrode  $e$  as stated by the Shockley-Ramo's theorem:

$$i_e(t) = -q v(t) E_{WF,e} \quad (2.3)$$

where  $v(t)$  is the instantaneous velocity of the charge  $q$  and  $E_{WF}$  is the weighting field, that is the field obtained biasing the electrode  $e$  with 1V and all the others with 0V. The drift velocity of the charge depends on the electric field and on the mobility of the particle:

$$v = \mu(E) E \quad (2.4)$$

where  $\mu(E)$  is a function of the electric field and is linear in  $E$  only for small  $E$ : at higher values the probability of interactions with optical phonons increases, the mobility drops

<sup>1</sup>Even if in principle both the electrode can be used to read the signal, for pixel detectors, where the number of channel and the complexity of readout are high, only one is actually used. In strip and pad detectors, instead, is more common a dual-side readout

and this leads to a saturation of the velocity (fig. 2.2). Typical values for electrons and holes mobility in silicon at room temperature are  $\mu_n \sim 1450 \text{ cm}^2/\text{Vs}$ ,  $\mu_h = 500$ .

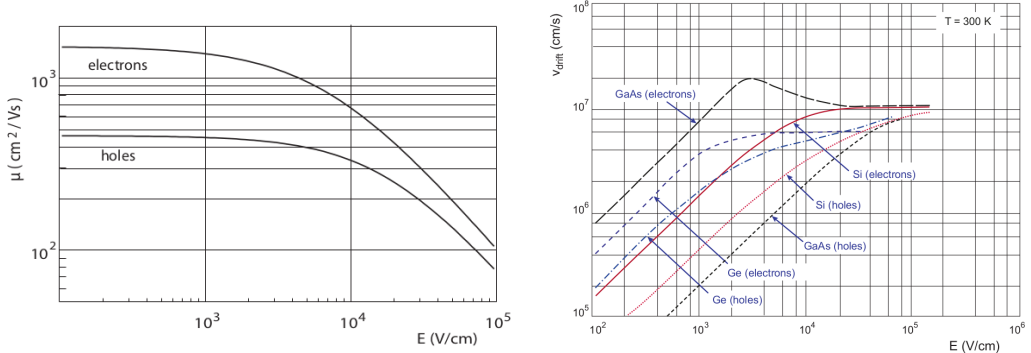


Figure 2.2: (a) Dependence of the mobility on the electric field. (b) Drift velocity at room temperature in different semiconductors

## 2.2 Charge Coupled Devices

In CCDs the charge is created in a very thin active epitaxial layer (typically 10  $\mu\text{m}$ , maximally about 30  $\mu\text{m}$ ) and then locally stored in a potential minimum which is created by a MOS structure. The size of the CCD cells is typically in the range 10  $\mu\text{m}$  to 20  $\mu\text{m}$  such that spatial resolutions are of the order of a few micrometres. The collected charges are moved stepwise from electrode to electrode (thus so called 'bucket chain') by applying a potential with a clock with frequency of  $\sim$ MHz; despite of such high frequency, the readout chain is completely sequential and this makes the entire process comparatively slow (tens of ms). A particular type of CCD, the pnCCDs, are typically used to detect low energy ( $<10$  keV) x-ray photons for their homogeneous spatial detection efficiency of photons. The pnCCDs have a sideward depletion similar to silicon drift chambers that makes the electric field stronger, compared with the normal CCDs. The pnCCDs designed for photon imaging are often fabricated with high Z materials, to increase absorption efficacy.

## 2.3 Hybrid pixels

Hybrid pixels, which currently are the state-of-art technology for large scale pixel detectors in most particle physics experiments, are made of two parts welded together through microconnection (bump bond): the sensor and the electronics (fig. 2.3a). They provide a practical system where the sensor and the ASIC (application specific integrated circuit) can be optimized separately, which makes them really fast, capable of handling with rate up to GHz. However a disadvantage of hybrid pixels is that they must be connected before testing. For reasons related with the historical development, the n<sup>+</sup>-in-n sensors were the first to be used; they demanded double-sided processing which guarantees the detector functionality both before and after the type inversion of the n<sup>-</sup> doped bulk into p-type after high quantity of radiation. The pn-diode is initially on the unstructured backside of the sensor, while after, the depletion zone grows from the electrode side into the bulk. This ensures that the signal can be sensed on the pixels even if the substrate is no longer fully depleted, even though the bias voltage required for a sufficient depletion increases,

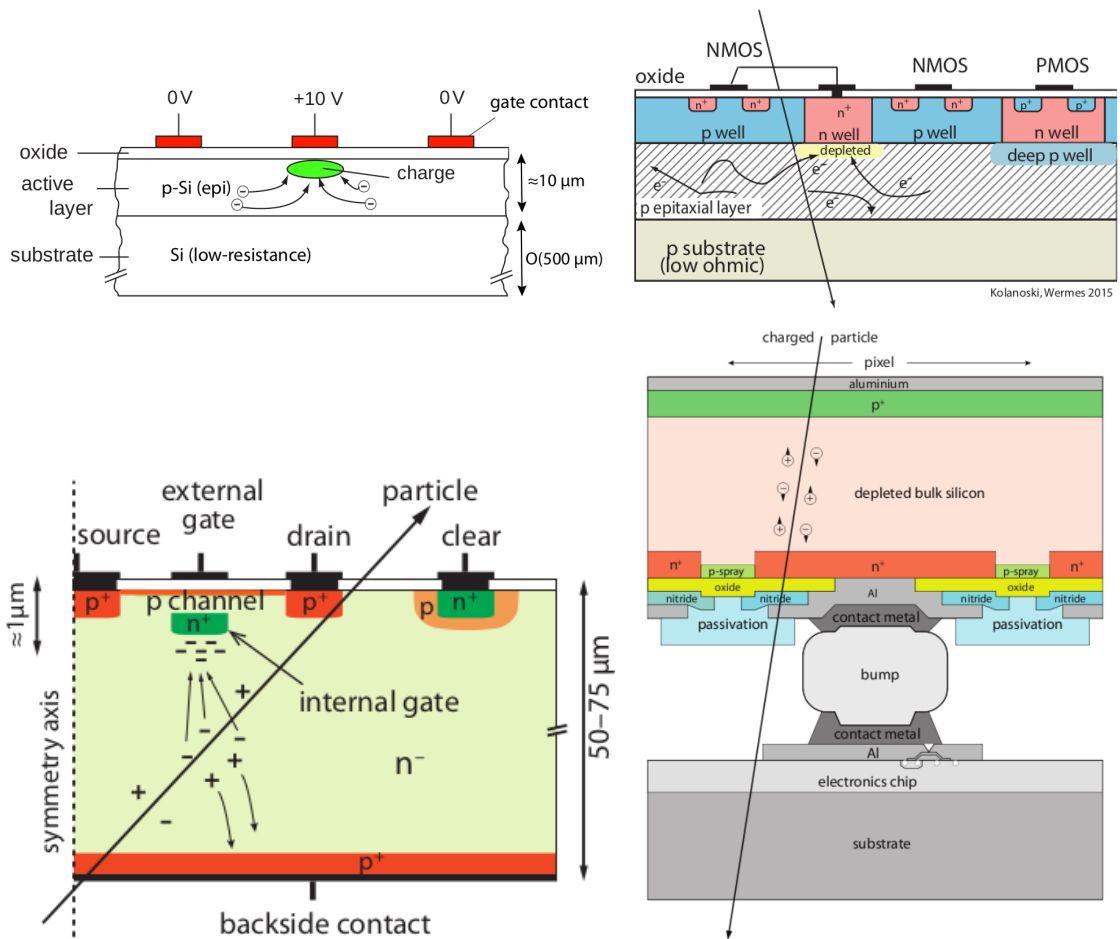


Figure 2.3: Concept cross-section of hybrid pixel (a) and of a DEPFET (b)

194 liming the detector lifetime up to a few years. With the availability of high quality p-  
195 substrate material ( $\gtrsim 2 \text{ k}\Omega\text{cm}$ ) the fabrication of n-in-p type sensors, which does not invert  
196 anymore, became the preferred choise leading also a huge advance in cost reduction due  
197 to no more need of double sided. However, the particular and sophisticated procedure to  
198 bond sensor and ASIC makes them difficult to produce, delicate (especially when exposed  
199 to high levels of radiation) and also expensive.

200 DEPFET are the first attempt towards the integration of the front end (FE) on the  
201 sensor bulk: they are typically mounted on a hybrid structure but the sensor also in-  
202 tegrates the first amplification stage. Each pixel implements a MOSFET (metal-oxide-  
203 semiconductor field-effect transistor) transistor (a p-channel in fig. 2.3b): a hole current  
204 flows from source to drain which is controlled by the external gate and the internal gate  
205 together. The internal gate is made by a deep  $n+$  implant towards which electrons drift  
206 after being created in the depletion region; the accumulation of electrons in the region  
207 underneath the n implant changes the gate potential and controls the transistor current;  
208 the removal of the signal charge from the internal gate is called "Clear". DEPFET typ-  
209 ically have a good S/N ratio: this is principally due to the amplification on-pixel, which  
210 guarantees any charge losses, and to the large depletion region. They can be operated in-  
211 dividually or integrated in the readout nodes of other detectors, as for example silicon drift  
212 chambers, but they always need to be connected to an ASIC with a readout circuit on it.  
213 In recent years, the sensor development was driven by an intensive R&D and prototyping  
214 for x-ray imagers and the ILC vertex detector.

## 215 2.4 CMOS MAPS and DMPAS

216 Monolithic active pixels accommodate on the same wafer both the sensor and the FE  
217 electronics, with the second one implanted on top within a depth of about  $1 \mu\text{m}$  below  
218 the surface. MAPS have been first proposed and realized in the 1990s and their practical  
219 usage has been enabled by the development of the electronic sector, which guarantees the  
220 halving of CMOS transistors dimension at least every two years, as stated by the Moore's  
221 law. As a matter of fact the dimension of components, their organization on the pixel  
222 area and logic density are important issues for the design and for the layout. Compared  
223 to CCDs, the readout time is dramatically reduced by the in-pixel amplification and  
224 discrimination, typically followed by a sparsified readout not requiring the signal to be  
225 transported anymore over thousands of pixels; as aside effect, the radiation tolerance is  
226 also greatly increased by sensing the signal charge directly within its own pixel.

227 A critical parameter for accelerator experiments is the material budget, which repre-  
228 sents the main limit factor for momentum measurement resolution in a magnetic field;  
229 since hybrid pixels are thicker ( $\sim$  hundreds of  $\mu\text{m}$ ) than monolithic ones (even less than  
230  $100 \mu\text{m}$ ). Using the latter the material budget can be down by a third: typical values for  
231 hybrid pixels is  $1.5 \% X_0$  per layer, while for monolithic  $0.5 \% X_0$ . Compared to MAPS,  
232 among other disadvantages of hybrid pixels there is the bigger power consumption, that  
233 requires also a bigger cooling system, leading to a futher increase of material.

234 Monolithic active pixel can be distinguished between two main categories: MAPS and  
235 depleted MAPS (DMPAS). MAPS (figure a ??) have typically an epitaxial layer in a from  
236 range  $1 \mu\text{m}$  to  $20 \mu\text{m}$  and, since they are not depleted, the charge is mainly collected by  
237 diffusion rather than by drift. This makes the path of charges created in the bulk longer  
238 than usual, making them slow (of order of  $100 \text{ ns}$ ). Moreover, the collection can be partial,

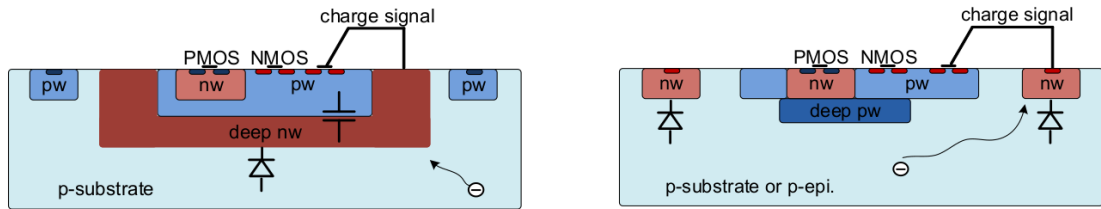


Figure 2.4: Concept cross-section with large and small fill factor

especially after irradiation of the detector (look at A for radiation damages), when the trapping probability becomes higher. In figure ?? it is shown as example of CMOS MAPS: the sensor implements an n well as collection diode; to prevent the others n wells (which contain PMOS transistor) of the electronic circuit competing in charge collection and to shield the CMOS circuit from the substrate, additional underlying deep p well are needed. DMAPS are instead MAPS depleted with  $d$  typically in  $\sim 25 \mu\text{m}$  to  $150 \mu\text{m}$  (eq. 2.2) which extends from the diode to the deep p-well, and sometimes also to the backside (in this case if one wants to collect the signal also on this electrode, additional process must be done).

#### 2.4.1 DMAPS: large and small fill factor

There are two different sensor-design approaches (figure 2.4) to DMAPS:

- large fill factor: a large collection electrode that is a large deep n-well and that host the embedded electronics
- small fill factor: a small n-well is used as charge collection node

To implement a uniform and stronger electric field, DMAPS often uses large electrode design that requires multiple wells (typically four including deep n and p wells); with this layout the total capacity of the sensor increases because of the addition of a new term (fig. 2.5), which contributes to the total amplifier input capacity ( $\sim 100 \text{ fF}$ ). In addition to the capacity between pixels ( $C_{pp}$ ) and between the pixel and the backside ( $C_b$ ), a non-negligible contribution comes from the capacities between wells ( $C_{SW}$  and  $C_{WW}$ ) needed to shield the embedded electronics. These capacities affect the thermal and  $1/f$  noise of the charge amplifier and the  $\tau_{CSA}$  too:

$$ENC_{thermal}^2 \propto \frac{4}{3} \frac{kT}{g_m} \frac{C_D^2}{\tau_{sh}} \quad \tau_{CSA} \propto \frac{1}{g_m} \frac{C_D}{C_f} \quad (2.5)$$

where  $g_m$  is the transconductance,  $\tau_{sh}$  is the shaping time. Among the disadvantages coming from this large input capacity there is a coupling between the sensor and the electronics resulting in cross talk noise on neighbouring electrodes; indeed, since digital switching in the FE electronics does a lot of oscillations, this problem is especially connected with the intra wells capacities. So, larger charge collection electrode sensors provide a uniform electric field in the bulk that results in short drift path and so in good collection properties, especially after irradiation, when trapping probability can become an issue.

The small fill-factor variant, instead, benefits from a small capacity (5 fF to 20 fF), but suffers from a non uniform electric field and from all the issue related to that (slowness and high trapping probability). As we'll see these two different types of sensor require

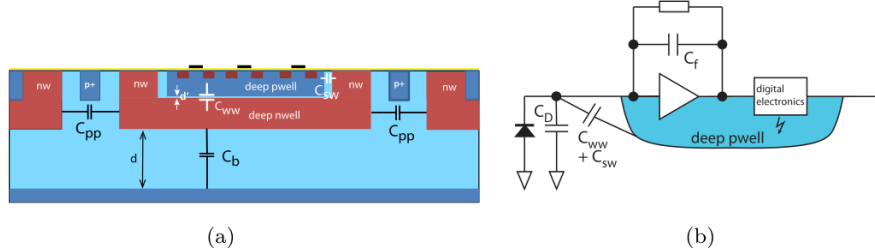


Figure 2.5:  $C_{pp}$ ,  $C_b$ ,  $C_{WW}$ ,  $C_{SW}$

	small fill factor	large fill factor
small sensor C	✓ (< 5 fF)	✗ ( $\sim 100$ 200 fF)
low noise	✓	✗
low cross talk	✓	✗
velocity performances	✓	✗ ( $\sim 100$ ns)
short drift paths	✗	✓
radiation hard	✗	✓

Table 2.1: Small and large fill factor DMAPS characteristics

271 different amplifier: the large electrode one is coupled with a charge sensitive amplifier,  
272 while the small one with a voltage amplifier (sec 2.5.1).

#### 273 2.4.2 A modified sensor

274 A process modification, developed by CERN in collaboration with the foundries, which  
275 has become the standard solution to combine the characteristics of a small fill factor  
276 sensor (small input amplifier capacity) and of a large fill factor sensor (uniform electric  
277 field), is the one carried out for ALICE upgrade about ten years [1]. A compromise  
278 between the two sensors could also be making smaller pixels, but this solution requires  
279 reducing the electronic circuit area, so a completely new pixel layout should be though.  
280 The modification consists in inserting a low dose implant under the electrode and one of  
281 its advantage lies in its versatility: in fact, both standard and modified sensor are often  
282 produced for testing.

283 Before the process modification, the depletion region extends below the diode towards  
284 the substrate, and it does not extend much laterally, even if a high bias is applied to the  
285 sensor (fig. 2.6). After the modification, two distinct pn junctions are built: one between  
286 the deep p well and the n<sup>-</sup> layer, and the other between the n<sup>-</sup> and the p<sup>-</sup> epitaxial  
287 layer, extending to the whole area of the sensor. Since deep p well and the p-substrate are  
288 separated by the depletion region, the two p electrodes can be biased separately<sup>2</sup> and this  
289 is beneficial to enhance the vertical electric field component. The doping concentration is  
290 a trimmer parameter: it must be high enough to be greater than in the epitaxial layer in  
291 order to prevent the punchthrough between p-well and the substrate, but it must also be  
292 low enough to allow the depletion for reasonable bias values.

<sup>2</sup>This is true in general, but it can be denied if other doping characteristics are implemented, and we will see that this is the case of TJ-Monopix1

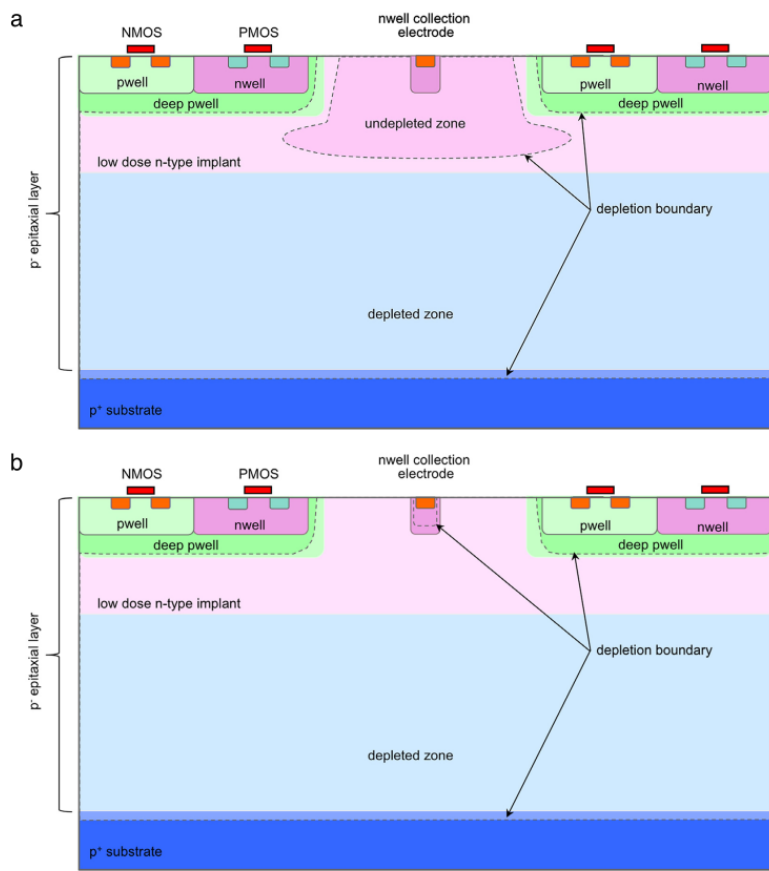


Figure 2.6: A modified process for ALICE tracker detector: a low dose n implant is used to create a planar junction. In (a) the depletion is partial, while in (b) the pixel is fully depleted.

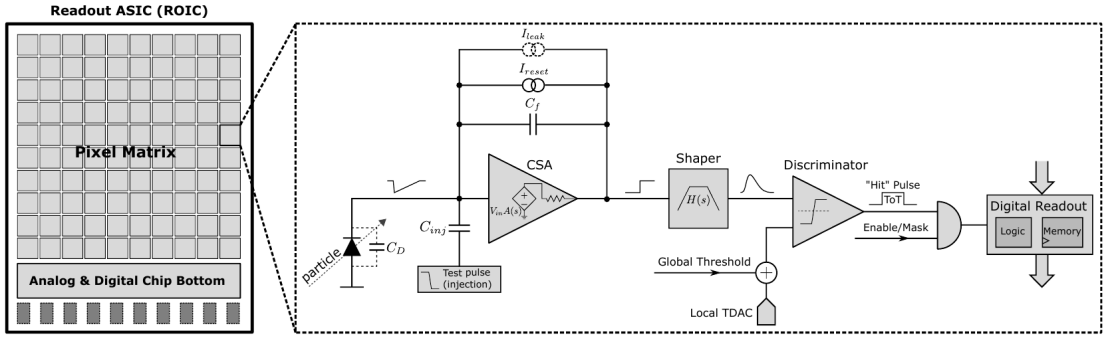


Figure 2.7: Readout FE scheme: in this example the preamplifier is a charge sensitive one (CSA) but changing the capacitive feedback into a resistive one, this can be converted in a voltage or current amplifier.

## 2.5 Analog front end

After the creation of a signal on the electrode, the signal enters the front end circuit (fig.2.7), ready to be molded and transmitted out of chip. Low noise amplification, fast hit discrimination and an efficient, high-speed readout architecture, consuming as low power as possible, are the goal of the readout integrated electronics (ROIC). The main parts of the analog front end chain are a preamplifier (that often is the only amplification stage) with a reset to the baseline mechanism and a leakage current compensation, a shaper (a band-pass filter) and finally a discriminator. The whole chain must be optimized and tuned to improve the S/N ratio. It is very important both not to have a large noise before the amplification stage in order to not multiply that noise, and chose a reasonable threshold of the discriminator to cut noise-hits much as possible.

### 2.5.1 Preamplifier

Even if circuits on the silicon crystal are only constructed by CMOS, a preamplifier can be processed as an operational amplifier (OpAmp) where the gain is determined by the input and feedback impedance (first step in figure 2.7):

$$G = \frac{v_{out}}{v_{in}} = \frac{Z_f}{Z_{in}} \quad (2.6)$$

Depending on whether a capacity or a resistance is used as feedback, respectively a charge or a voltage amplifier is used: if the voltage input signal is large enough and has a sharp rise time, the voltage sensitive preamplifier is preferred. Consequently, this flavor doesn't suit to large fill factor MAPS whose signal is already high enough:  $v_{in} = Q/C_D \approx 3 \text{ fC}/100 \text{ pF} = 0.03 \text{ mV}$ , but it's fine for the small fill factor ones:  $v_{in} = Q/C_D \approx 3 \text{ fC}/3 \text{ pF} = 1 \text{ mV}$ .

In the case of a resistor feedback, if the signal duration is longer than the discharge time ( $\tau = R_S C_D$ ) of the detector the system works as current amplifier, as the signal is immediately transmitted to the amplifier; in the complementary case (signal duration longer than the discharge time) the system integrates the current on the  $C_D$  and operates as a voltage amplifier.

## 319 2.6 Readout logic

320 The readout logic includes the part of the circuit which takes the FE output signal, pro-  
 321 cesses it and then transmit it out of pixel and/or out of chip; depending on the situation  
 322 of usage different readout characteristics must be provided. To store the analogical in-  
 323 formation (i.e. charge collected, evolution of signal in time, ...) big buffers and a large  
 324 bandwidth are needed; the problem that doesn't occur, or better occur only with really  
 325 high rate, if one wants record only digital data (if one pixel is hit 1 is recorded, and if not  
 326 0 is recorded).

327 A common compromise is to store the time over threshold (ToT) of the pulse in clock  
 328 cycle counts; this needs of relatively coarse requirement as the ToT can be trimmed down  
 329 to use only a dozen bits but, being correlated (and hopefully linear) with the deposited  
 330 charge, it provides a sufficient information. The ToT digitalization usually takes advantage  
 331 of the distribution of a clock (namely BCID, bunch crossing identification) on the pixels'  
 332 matrix. The required timing precision is better than  $\sim 25$  ns, that corresponds to the period  
 333 between bunch collisions at LHC; for such reason a reasonable BCID-clock frequency for  
 pixels detector is 40 MHz.

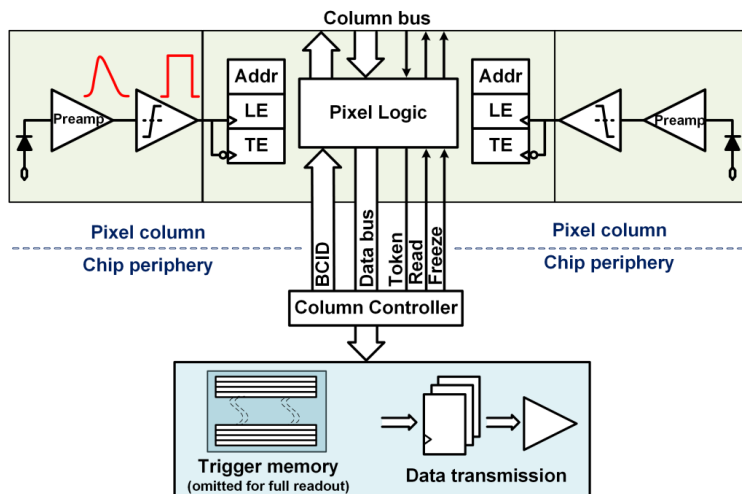


Figure 2.8: Column drain R/O scheme where ToT is saved

334 Moreover, the readout architecture can be full, if every hit is read, or triggered, if a  
 335 trigger system decides if the hit must be stored or not. On one hand the triggered-readout  
 336 needs buffers and storage memories, on the other the full readout, because there is no  
 337 need to store hit data on chip, needs an high enough bandwidth. A triggered readout is  
 338 fundamental in accelerator experiments where the quantity of data to store is very large  
 339 and some selection has to be applied by the trigger: to give an order of magnitude, at LHC  
 340 more than 100 TBit/s of data are produced, but the storage limit is about 100 MBit/s  
 341 [2](pag. 797). Typically, the trigger signal is processed in a few  $\mu s$ , so the pixel gets it  
 342 only after a hundred clock cycles from the hit arrival time: the buffer depth must be able  
 343 to handle such high trigger latency.

345 After having taken out the data from the pixel, it has to be transmitted to the end  
 346 of column (EoC) where a serializer delivers it out of chip, typically to an FPGA. There  
 347 are several ways of transmitting data from a pixel to the EoC: one of the most famous  
 348 is the column-drain read out, developed for CMS and ATLAS experiments [3]. All the

349 pixels in a double-column share a data bus and only one pixel at a time, according to  
 350 a priority chain, can be read. The reading order circuit is implemented by shift register  
 351 (SR): when a hit arrives, the corresponding data, which can be made of timestamp and  
 352 ToT, is temporarily stored on a RAM until the SR allows the access to memory by data  
 353 bus. Even if many readout architectures are based on the column-drain one, it doesn't suit  
 354 for large size matrices. The problem is the increasing number of pixels on a column would  
 355 also raise the number of pixels in the priority chain, which would result in a slowdown of  
 356 the readout.

357 If there isn't any storage memory, the double-column behaves as a single server queue  
 358 and the probability for a pixel of waiting a time  $T$  greater than  $t$ , with an input hit rate  
 359 on the column  $\mu$  and an output bandwidth  $B_W$  is [4]:

$$P(T > t) = \frac{\mu}{B_W} e^{-(B_W - \mu)t} \quad (2.7)$$

360 To avoid hit loss (let's neglect the contribution to the inefficiency of the dead time  $\tau$  due  
 361 to the AFE), for example imposing  $P_T > t \sim 0.001$ , one obtains  $(B_W - \mu) t_t \sim 6$ , where  
 362  $t_t$  is the time needed to transfer the hit; since  $t_t$  is small, one must have  $B_W \gg \mu$ , that  
 means a high bandwidth [4].

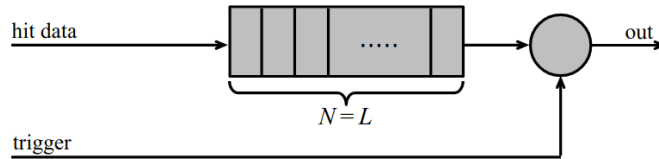


Figure 2.9: Block diagram of a pipeline buffer: N is the dimension of memory buffer and L is the trigger latency expressed in BCID cycles

363 Eq.2.7 is actually an approximation, since each pixel sees a different bandwidth de-  
 364 pending on the position on the queue: the first one sees the full bandwidth, while the next  
 365 sees a smaller one because it can be occasionally blocked by the previous pixel. Then,  
 366 the bandwidth seen by the pixel  $i$  is  $B_i = B - \sum_j \mu_j$ , where  $\mu_j$  is the hit rate of the  $j$ th  
 367 pixel. The efficiency requirement on the bandwidth and the hit rate becomes:  $B_{W,i} > \mu_i$ ,  
 368 where the index  $i$  means that the constraint is for a single pixel; if all the N pixels on a  
 369 column have the same rate  $\mu = N\mu_i$ , the condition reduces to  $B_W > \mu$ . The bandwidth  
 370 must be chosen such that the mean time between hits of the last pixel in the readout chain  
 371 is bigger than that. In order to reduce the bandwidth, a readout with zero suppression  
 372 on pixel is typically employed; this means that only information from channels where the  
 373 signal exceeds the discriminator threshold are stored.

375 If, instead, the signal is locally stored until a trigger signal arrives, the input rate to  
 376 column bus  $\mu'$  is reduced compared to the hit rate  $\mu$  as:  $\mu' = \mu \times r \times t$ , where  $r$  is the  
 377 trigger rate and  $t$  is the bunch crossing period. In this situation there is a more relaxed  
 378 constraint on the bandwidth, but the limiting factor is the buffer depth: the amount of  
 379 memory designed depends both on the expected rate  $\mu$  and on the trigger latency  $t$  as  
 380  $\propto \mu \times t$ , which means that the higher the trigger latency the lower the hit rate to cope  
 381 with.

382 In order to have an efficient usage of memory on pixels' area it's convenient grouping  
 383 pixels into regions with shared storage. Let's compare two different situations: in the first  
 384 one a buffer is located on each pixel area, while in the second one a core of four pixels

385 share a common buffer (this architecture is commonly called FE-I4).

Consider a 50 kHz single pixel hits rate and a trigger latency of 5  $\mu$ s, the probability of

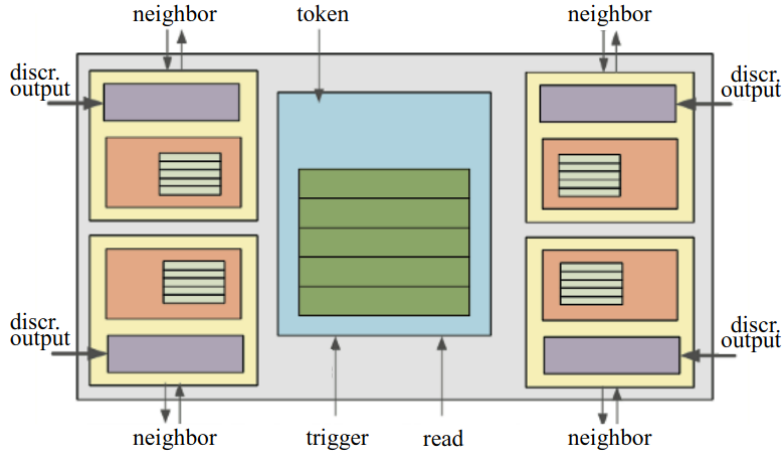


Figure 2.10: Block diagram of the FE-I4 R/O. Read and memory management section is highlighted in light blue; latency counters and trigger management section are highlighted in green; hit processing blocks are highlighted in purple; ToT counters and ToT management units are highlighted in orange

386

387 losing hits is:

$$P(N > 1|\nu) = 1 - P(N = 0|\nu) - P(N = 1|\nu) = 1 - e^{-\nu}(1 + \nu) \approx 2.6\% \quad (2.8)$$

388 where I have assumed a Poissonian distribution with mean  $\nu = 0.25$  to describe the counts  
389 N.

390 To get an efficiency  $\epsilon$  greater than 99.9 % a 3 hit depth buffer is needed:

$$P(N > 3|\nu) = 1 - \sum_{i=0}^3 P(N = i|\nu) < 0.1\% \quad (2.9)$$

391 Consider the second situation: if the average single pixel rate is still 50 kHz, grouping four  
392 pixels the mean number of hits per trigger latency is  $\nu = 0.25 \times 4 = 1$ . To get an efficiency  
393 of 99.9% (eq. 2.9) a buffer depth of 5 hits in the four-pixels region, instead of 3 per pixels,  
394 is needed.

395 **Chapter 3**

396 **Use of pixel detectors**

397 The relation between the development of cameras and that of pixel detectors dates back  
398 to 1969, when the idea of CCDs, for which Boyle and Smith were awarded the Nobel Prize  
399 in Physics in 2009, revolutionized photography allowing light to be captured electronically  
400 instead of on film. Even though the CMOS technology already existed at the time the  
401 CCDs spread, the costs of productions were too high to allow the diffusion of these sensors  
402 for the following 20 years. From that moment on, the fast diffusion of CMOS was mainly  
403 due to the less cost than CCD, and the less power supply required. Nowadays CCDs  
404 are still preferred over MAPS in astronomy, where the astronomical sources' rate are low  
405 enough to cope with slow readout time (tens of ms).

406 The principal use cases of pixel detectors are particle tracking and imaging: in the  
407 former case individual charged particles have to be identified, in the latter instead an  
408 image is obtained by the usually un-triggered accumulation of the impinging radiation.  
409 Also the demands on detectors performance depends on their usage, in particular tracking  
410 requires high spatial resolution, fast readout and radiation hardness.

411 **3.1 Tracking in HEP**

412 At first the physics world overlooked the CCDs, and all pixel in general, as against the  
413 gaseous detector for tracking: there was no need to replace these ones which had a sufficient  
414 good resolution ( $100\text{ }\mu\text{m}$ ). Since 1974, with the measurement of the invariant mass of the  
415 J/Psi and the affirmation of the quark model, all experiments start to look for better  
416 spatial resolutions in order to achieve the possibility of reconstructing short lived particle.

417 Historically, the first pixel detector employed in particle physics was a CCD: it was  
418 installed in the spectrometer at the CERN's Super Proton Synchrotron (SPS) by the  
419 ACCMOR Collaboration (Amsterdam, CERN, Cracow, Munich, Oxford, RAL) at mid  
420 1980s, with the purpose of studying the (at the time) recently-discovered charm particles.  
421 The second famous usage of CCDs took place at SLAC in the Large Detector (SLD) during  
422 the two years 1996-98, where the CCD technology was adopted instead of the microstrip  
423 detectors for their excellent spatial resolution (cell size  $22\times 22\text{ }\mu\text{m}^2$  giving a resolution of  
424  $\sim 5\text{ }\mu\text{m}$ ) thanks to the sufficient time for readout between two successive collisions (160 ms).

425 From that period on, particle tracking in HEP experiments have been transformed  
426 radically. It became mandatory to build an inner vertex detector, with the following tasks:

- 427 • pattern recognition with the identification of particle tracks at large backgrounds and  
428 pile-up

- measurement of vertices (primary and secondary)
- multi-track and vertex separation in the core of jets
- measurement of specific ionization
- momentum measurement combining with other detectors informations

In 1991, the more demanding environments led to the development of hybrid pixel detectors: a dedicated collaboration, RD19, was established at CERN with the specific goal of defining a semiconductor micropattern detector with an incorporated signal processing at a microscopic level. In those years a wide set of prototypes of hybrid pixel has been manufactured; among the greatest productions a mention goes to the huge ATLAS and CMS vertex detectors. From the middle of 2013 a second collaboration, RD53, has been established with the new goal of finding a pixel detector suitable for the phase II in future upgrades of those experiments. Even if the collaboration is specifically focused on the design of hybrid pixel readout chips (aiming to 65 nm technique), also other options have been taken in account and many test have been done on MAPS. Requirements imposed by LHC are stringent and they will become even more with the increase of luminosity at HL-LHC: for example, a dose and radiation of 5 Mrad and  $10^{16}$ NIEL are expected after 5 years of operation. Time resolution, material budget and power consumption are also issues for the upgrade: to distinguish different events from different bunches a time resolution better than 25 ns for a bunch crossing frequency of 40 MHz is required, a material budget lower than 2% and a power consumption lower than  $500\text{ mW/cm}^2$  are required.

Amidst the solutions proposed 3D silicon detector, invented by Sherwood Parker in 1995, and MAPS are the most promising. In 3D sensors the electrode is a narrow column of n-type implanted vertically across the bulk instead of being implanted on the wafer's surface. The charge produced by the impinging particle is then drifted transversally within the pixel, and, as the mean path between two electrode can be sufficient low, the trap probability is not an issue. Even if 3D detector are adequately radiation hard and are a strong contender for hybrid pixel modules, especially in the innermost pixel detector layer, their fabrication process is currently low volume, making them unlikely to cover large areas.

### 3.1.1 Hybrid pixels at LHC and at SuperKEKB

#### ATLAS

With CMS, ATLAS is one of two general-purpose detectors at the LHC and has the largest volume detector ever constructed for a particle collider (46 m long and 25 m in diameter). The Inner Tracker (ITk) consists of three different systems all immersed in a magnetic field parallel to the beam axis whose main components are: the pixel, the micro-strips and transition radiation trackers. Concerning the pixel detector, they installed a 3-layer hybrid pixel detector in 2007 and an additional one inserted within the original detector envelope and therefore called insertable B-layer (IBL) in 2014. 92 million pixels are divided in 4 barrel layers and 3 disks in each end-cap region, covering a total area of  $1.9\text{ m}^2$  and having a 15 kW of power consumption.

As stated by the ATLAS collaboration the pixel detector is exposed by an extreme particle flux: "By the end of Run 3<sup>1</sup>, the number of particles that will have hit the

---

<sup>1</sup>Run 3 start in June 2022

471 innermost pixel layers will be comparable to the number it would receive if it were placed  
 472 only a few kilometres from the Sun during a solar flare". Considering that the particle  
 473 density will increase even more with HL-LHC, radiation hardness is definitively target to  
 474 achieve. The most ambitious goal is employ a MAPS-based detector for the inner-layer  
 475 barrels, and for this reason the RD53 collaboration is designing many MAPS prototypes  
 476 (as for example TJ-Monopix1, which I will talk about in chapter 4) and performing test.  
 477 Up to now this possibility will be eventually implemented during the second phase of the  
 478 HL-LHC era, as at the start of high-luminosity operation the selected option is the hybrid  
 479 one. The sensor will be bonded with ITkPix, the first full-scale 65 nm hybrid pixel-readout  
 480 chip developed by the RD53 collaboration. Regarding the sensor, a valuable option is  
 481 using 3D pixels, which have already proved themselves in ATLAS, for the IBL, where they  
 482 were introduced in a limited acceptance range and introduced a new readout integrated  
 483 circuit called FE-I4. Also the complexity of the readout will be raised, as the number of  
 484 pixels will be increased of a factor about 7, passing from 92 millions to 6 billion.

## 485 CMS

486 The CMS hybrid pixel detector has been upgraded in 2017, when, with the replacement  
 487 of a piece of the beam pipe, a layer has been added to the detector at 3 cm from it.  
 488 124 million pixels are divided between the barrel pixel detector (BPIX) and the forward  
 489 disks (FPIX), with sensors which are different from each other and produced by different  
 490 foundries. The sensors have an area equal to 100  $\mu\text{m}$  by 150  $\mu\text{m}$  and have been produced  
 491 on 285  $\mu\text{m}$  to 300  $\mu\text{m}$  thick wafers.

492 The time resolution is 25 ns, and the information coming from the detector are stored on  
 493 chip for the Level-1 trigger latency ( $\sim 4 \mu\text{s}$ ). The upgrade baseline ROIC was redesigned for  
 494 the outer 3 layers, replacing analog signal readout with on-chip ADCs and digital readout  
 495 at higher rate. reads out the pulse height information for each pixel.

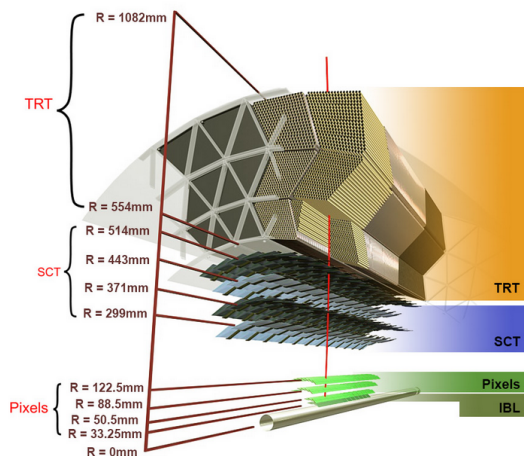


Figure 3.1: ATLAS tracker detector

## 496 LHCb

497 LHCb is a dedicated heavy-flavour physics experiment that exploits pp interactions at  
 498 14 TeV at LHC. It was the last experiment to upgrade the vertex detector, the Vertex

499 Locator (VELO), replacing the silicon-strip with 26 plane pixel detector (because of the  
 500 fixed target geometry) in May 2022. As the instantaneous luminosity in Run3 is increased  
 501 by a factor  $\lesssim 10$ , much of the readout electronics and of the trigger system have been  
 502 developed in order to cope with the large interaction rate. To place the detector as close as  
 503 possible to the beampipe and reach a better track reconstruction efficiency and resolution,  
 504 the VELO has a surprising feature: during the injection of LHC protons it is parked at  
 505 3 cm from the beams and only when the stability is reached it is moved at  $\sim 5$  mm. Readout  
 506 speed is a priority for the detector that uses a triggerless readout at 40 MHz collision rate,  
 507 producing 20 Gbps per ROIC. The Velopix, which is the hybrid system designed for LHCb,  
 508 is made bonding sensors, each measuring  $55 \times 55$  micrometers, 200  $\mu\text{m}$ -thick to a 200  $\mu\text{m}$ -  
 509 thick ASIC specially developed for LHCb and coming from the Medipix family (sec. ??),  
 510 which can handle hit rates up to 900 MHz per chip. Since the detector is operated under  
 511 vacuum near the beam pipe, the heat removal is particularly difficult and evaporative CO<sub>2</sub>  
 512 microchannel cooling are used.

### 513 **BelleII**

514 Due to the high background level coming from the nanobeam used at SuperKEKB in  
 515 order to achieve a such high luminosity ( $4.7 \times 10^{34} \text{ cm}^{-2}/\text{s}$ ), silicon strip cannot be used  
 516 in the inner layer of the tracker. The occupancy is too high to allow the usage of strips up  
 517 to 40 mm from the beam pipe. Moreover for a precise reconstruction of B-decay vertices,  
 518 the usage of thin detector is mandatory at the low energy (4 GeV to 7 GeV) of the beam,  
 in order to minimize the multiple scattering of particles. The current vertex detector of

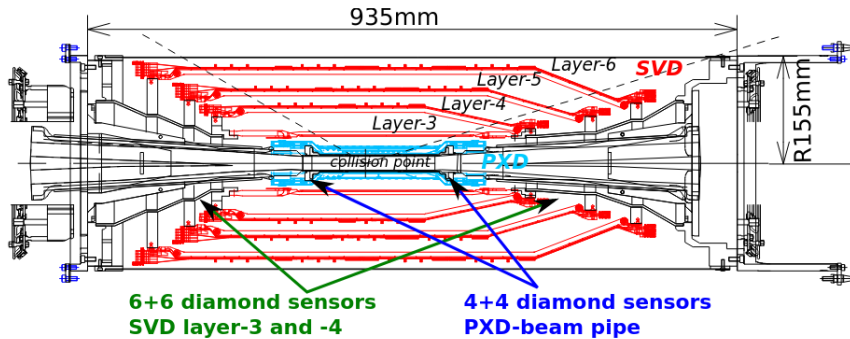


Figure 3.2: Belle2 vertex detector. Since an accidental beam background enhancement can damage the VXD, diamond detectors are installed in order to monitor it.

519  
 520 BelleII, VXD, is made of a pixel detector (PXD), fabricated with 2 layers of DEPFET-  
 521 based pixels, and 4 layers of a double-sided silicon strip detectors (SVD)[5]. Due to the  
 522 small capacitance of the collection node, DEPFET presents a high signal-to-noise ratio  
 523 (in 30-50) thanks to the low intrinsic noise and to the large signal achieved with the fully  
 524 depleted bulk: pixels are thinned to 75  $\mu\text{m}$  in the active region, then a MIP is supposed  
 525 to create a signal of  $\sim 6000 \text{ e}^-$ , while the typical noise of DEPFET is around 200  $\text{e}^-$ . The  
 526 ASIC read out is still based on a rolling shutter logic, with an integration time of 20  $\mu\text{s}$ .  
 527 In order to reduce the data-storage memory PXD hits are only used to improve spatial  
 528 resolution of tracks: the SVD informations are used by the High Level Trigger (HLT) to  
 529 look for regions of interest in the pixel ladders just by extrapolating back the tracks found  
 530 in the tracker detector, and this method allows to store only data belonging to these areas;



Figure 3.3: (a) Block-diagram of the ULTIMATE-2 sensor. (b) The HFT pixel detector of STAR;

531 the PXD hits are then used in offline track fit to improve the vertex resolution.

532 MAPS have been proposed for the replacement of VXD during the Long Shut Down  
 533 2 (LSD2) foreseen around 2026-27; the new vertex detector, VTX, should be made of 5  
 534 layers fabricated by the optimized Belle II pixel sensor (OBELIX), a detector based on  
 535 TJ-Monopix have been selected (look at chapter ??). The main advantages VTX should  
 536 bring are a obvious improving in the track and vertex resolution (14 μm before upgrade,  
 537  $\lesssim 10 \mu\text{m}$  expected after upgrade) and a reduction in the  $X_0$  (da.. a..), a higher background  
 538 tolerance because of the smaller sensor than strips dimension and a low bandwidth due to  
 539 the on-chip sparsification.

### 540 3.1.2 First attempts to MAPS

#### 541 MIMOSA at EUDET and STAR

542 MIMOSA [6][7] (standing for Minimum Ionizing MOS Active pixel sensor), designed in  
 543 2008, prefigured the architecture of MAPS for coming vertex detector being the first large  
 544 scale sensor to be employed as detector. MIMOSA-26 equiped the final version of EUDET  
 545 high resolution beam telescope both at CERN-SPS and at DESY while the MIMOSA-  
 546 28 devices are used for the first MAPS-based vertex detector at the STAR experiment.  
 547 MIMOSA-26 is fabricated in a 350 nm, and a module features 1152 columns, split into  
 548 18 independent groups, and 576 rows, with square pixels having a side of 18.4 μm lenght;  
 549 the epitaxial layer is not fully depleted and the charge collection is mostly by diffusion,  
 550 resulting in charge sharing between pixels and collection time bigger than 100 ns.

551 The readout is done in a rolling shutter mode and it is the first MAPS integrating on  
 552 chip the zero suppression: the chip is an Active Pixels (APS) and therefore it incorporates  
 553 the amplification on pixel, while the signal discrimination and zero-suppression logic are  
 554 placed at the EoC, where is also placed a memory. The chip is an Active Pixels (APS)  
 555 and therefore it incorporates the amplification on pixel, while the signal discrimination  
 556 and zero-suppression logic are placed at the EoC: the readout is done in a rolling shutter

557 mode with a frame integration time that can be lowered down to 85 ms, and a memory  
558 allowing to store up to six hits is.

559 The EUDET telescope, equipped with six sensor planes, requires highly granular and  
560 thin pixel detectors in order to achieve an excellent track resolution (around 2  $\mu\text{m}$ ) even at  
561 the rather low particle energies of up to 6 GeV. The STAR experiment at the Relativistic  
562 Heavy Ion Collide (RHIC) accelerator at the Brookhaven National Laboratory (BNL) is  
563 the first to include MAPS in the vertex detector[8]. The main tracking detector in STAR is  
564 a TPC with radii 60-190 cm embedded in a 0.5 T solenoidal magnetic field, that provides  
565 a pointing resolution of approximately 1 mm. The pixel detector, PXL, is a part of a  
566 3-detector system, Heavy Flavor Tracker (HFT), that has been added to the pre-existing  
567 STAR apparatus just before the 2014 Run in order to improve the impact parameter  
568 resolution and to enable the direct reconstruction of hadronic decays of heavy flavor mesons  
569 and baryons. The Heavy Flavor Tracker (HFT) is composed by the Silicon Strip Detector  
570 (SSD), the Intermediate Silicon Tracker (IST) and the Pixel Detector (PXL); the first  
571 one is placed at 22 cm from the beam pipe and consists of double sided strips with 95  $\mu\text{m}$   
572 inter-strip pitch, the second one, placed at 14 cm, is made of single sided silicon pads  
573 with  $600 \mu\text{m} \times 6 \text{ mm}$  pitch and the last one made by two layers is placed at 2.8 cm and 8 cm  
574 fabricated with ULTIMATE2 (also known as MIMOSA-28), a successor of MIMOSA-26  
575 sensor, with pitch 20.7  $\mu\text{m}$  and thinned down to 50  $\mu\text{m}$ . An area of  $0.16 \text{ m}^2$  are covered  
576 by 400 MAPS sensor, corresponding to 356 millions of pixels divided into array size of  $928$   
577  $\times$  960. Each pixel includes circuitry for readout, amplification, and Correlated Double  
578 Sampling (CDS) for signal extraction and noise subtraction and the frame integration time  
579 is 185.6  $\mu\text{s}$ ; after the subtraction the signal to noise ratio is  $\sim 30$ , with a noise between  
580 10-12 electrons and a signal of  $1000 \text{ e}^-$ . Thanks to the HFT system and the PXL, STAR  
581 achieved a track pointing resolution 46  $\mu\text{m}$  for 750 MeV/c kaons, and better than 30  $\mu\text{m}$  for  
582 particle momenta bigger than 1 GeV/c: this performance enabled the study of D-meson  
583 production with a high significance signal.

584 **ALPIDE at ALICE**

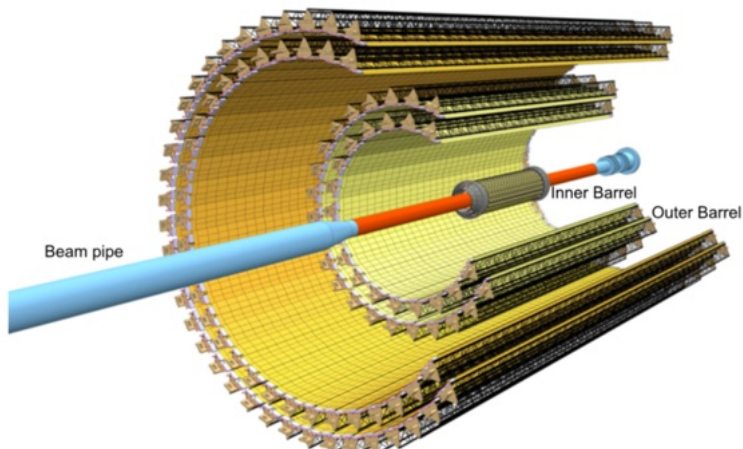


Figure 3.4

585 ALICE (A Large Ion Collider Experiment) is a detector dedicated to heavy-ion physics  
586 at the LHC. The tracking detector consists of the Inner Tracking System (ITS), the gaseous

587 Time Projection Chamber (TPC) and the Transition Radiation Detector (TRD), and all  
588 those are embedded in a magnetic field of 0.5 T. The ITS is made by six layers of detectors,  
589 two for each type, from the interaction point outwards: Silicon Pixel Detector (SPD),  
590 Silicon Drift Detector (SDD) and Silicon Strip Detector (SSD). Contrary to the others  
591 LHC experiments, ALICE tracker is placed in a quite different environments: the expected  
592 dose is smaller by two order of magnitude and the rate of interactions is few MHz instead  
593 of 40 MHz, but the number of particles comes out of each interaction is higher (the SPS is  
594 invested by a density of particles of  $\sim 100 \text{ cm}^{-2}$ ). The reconstruction of very complicated  
595 events with a large number of particle is a challenge, hence to segment and to minimize  
596 the amount of material, which may cause secondary interaction complicating further the  
597 event topology, is considered a viable strategy.

598 ITS2, upgraded during the LHC long shut down in 2019-20, was the first large-area  
599 ( $\sim 10 \text{ m}^2$  covered by 2.5 Gpixels) silicon vertex detector based on CMOS MAPS. The  
600 detector employs the ALPIDE chip, developed by ALICE collaboration, fabricated in the  
601 180 nm CMOS Imaging Sensor process of TowerJazz, whose design takes full advantage  
602 of process feature which allows full circuitry within the pixel matrix. Thanks to the  
603 reduction of the material budget, ITS2 obtained an amazing improvement both in the  
604 position measurement and in the momentum resolution, improving the efficiency of track  
605 reconstruction for particle with very low transverse momentum (by a factor 6 at  $pT \sim$   
606 0.1 GeV/c). Further advancements in CMOS MAPS technology are being aggressively  
607 pursued for the ALICE ITS3 vertex detector upgrades (foreseen around 2026-27), with  
608 the goals of further reducing the sensor thickness and improving the readout speed (which  
609 now is completely asynchronous) of the devices, while keeping power consumption at a  
610 minimum.

### 611 3.2 Other applications

612 Historically for imaging purpose the CCDs were the favoured device: they can be used as  
613 single photon counter or integrating and collecting the charge released by more impinging  
614 particles. The utilisation in the first case is similar to the tracking one, except that the  
615 requirements are less tight, so much that two noteworthy of microchips originally meant  
616 for detectors in particle physics at the LHC, and later employed in other fields are Medipix  
617 and Timepix. They are read-out chips developed by the Medipix Collaborations since early  
618 1990s. For two decades, different Medipix generations have been produced, having a rough  
619 correlation with the feature size used: Medipix2 (1999) used 250 nm feature size CMOS  
620 while Medipix3 (2005) 130 nm. For photons imaging other materials with higher atomic  
621 charge than silicon could be preferred, as a high photon absorption efficiency is needed: it  
622 was for this reason that Medipix2 was bump bonded to identically segmented sensors of  
623 both silicon and GaAs.

624 The applications in scientific imaging vary from astrophysics and medical imaging and  
625 dosimetry to more exotic domains as studies of protein dynamics, material science, art  
626 authentication and archaeology. One of the most important employment of Medipix is as  
627 X-ray single photon counting in industrial and medical radiography and in 3D computed  
628 tomography<sup>2</sup>. Thanks to a New-Zealand company, the MARS Bioimaging detector has  
629 been fabricated, which is capable of resolving the photons energy and produce 3D coloured

---

<sup>2</sup>The analysis of the direction dependence of X-ray absorption is performed, for example, in order to obtain an image in Computed Tomography (CT)

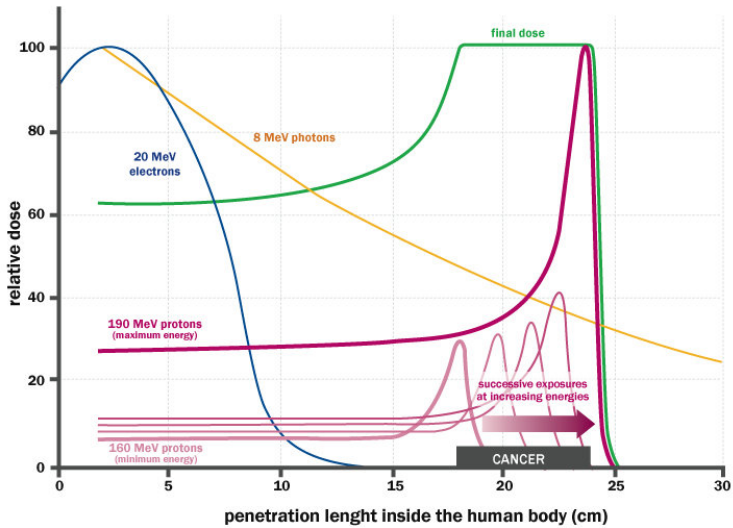


Figure 3.5: The Spread Out Bragg Peak (SOBP) curve (green), which is a constant dose distribution, is obtained from the superposition of many Bragg peak of hadrons with different energy.

630 images. Besides tracking in HEP (I have already cited the use of Timepix3 is in the beam  
 631 telescope of the LHCb VELO), an important use of Timepix is in dosimetry. [Timepix](#)  
 632 [Detector for Imaging in Ion Beam Radiotherapy- articolo e qualche info](#). A small-Timepix  
 633 detector with the dimension of a USB can also be found at the International Space Station,  
 634 where it is exploited for radiation, principally made of heavy-ion, monitoring.

### 635 3.2.1 Applicability to FLASH radiotherapy

636 A possible new application of pixels detector is dosimetry or beam monitoring of charge  
 637 particles in high intensity radiography. Recently<sup>3</sup> a promising method for RT at ultra high  
 638 dose rate (at least 40 Gy/s) and for this reason called FLASH-RT[9], instead of CONV-RT  
 639 (0.03 Gy/s), came out. However, finding dosimeters suitable at ultra high dose rate is still  
 640 an open issue since almost all standard online dosimeters have shown saturation problems.

### 641 Radiotherapy

642 The radiological treatment is a common method used in 60% of tumors both as palliative  
 643 care and as treatment. It can be given before, after or during a surgery, (Intra operative  
 644 radiation therapy-IORT) and many different types of radiations (photons, electrons,  
 645 protons and ions, which mainly are hydrogen and carbon) can be used to irradiate the  
 646 affected tissues. Exploiting the ionizing energy loss, that can be parametrized by the  
 647 Linear Energy Transfer (LET), a biological damage can be delivered to the tissue: while  $\alpha$   
 648 and  $\beta$  particles are high LET radiations with values in  $100 \text{ keV}/\mu\text{m}$  to  $200 \text{ keV}/\mu\text{m}$ , x-rays  
 649 and gamma-rays are low LET radiations with values in range  $0.2 \text{ keV}/\mu\text{m}$  to  $2 \text{ keV}/\mu\text{m}$ . If  
 650 x-ray photons, with energy in  $4 \text{ MeV}$  to  $25 \text{ MeV}$  are used, the ionization is caused by the

<sup>3</sup>The first evidences has been observed on a mice experiments in 1966 and in 2014 by the group of Favaudon and Vozenin. After this, many test on cats and pigs have been performed, and also there has been a clinical trial on a cutaneous tumor-patient

	CONV-RT	FLASH-RT
Dose rate	0.03 Gy/s	40 Gy/s
Intra pulse dose rate	100 Gy/s	106 Gy/s
Treatment duration	~minutes	$\lesssim 500$ ms
Dose Per Pulse	0.3 mGy	1 Gy to 10 Gy
Pulse width	3 $\mu$ s	$\sim 2 \mu$ s

Table 3.1: Typical value of treatment parameters

651 Compton electrons and is more in the superficial layers of the tissue due to the exponential  
 652 attenuation of the beam. The hardrons energy loss, instead, is strongly localized in  
 653 the last region of the track, that is the Bragg peak, such as the the treatment typically  
 654 requires the scanning of the target. The Relative Biological Effectiveness (RBE) of ions  
 655 near th Bragg peak depends on their mass, and in particular it increases with the ion's  
 656 mass; even though, too heavy ions generally increases the damage produced also in the  
 657 entrance region. Carbon is considered the optimum between the two trends.

658 Electrons, instead, of energy in range of a dozen of MeV tend to spread out on a  
 659 bigger region of a few centimeters in both the diameter and thickness. Using Very High  
 660 Energy Electrons (VHEE) has been taken into account for irradiation of deeper tissues,  
 661 however, to date, the FLASH effect has been tested and demostrated only using low-energy  
 662 electrons.

### 663 **FLASH effect**

664 This treatment takes advantages of biological differences between tumors and healthy  
 665 tissues: it is characterized by reducing normal tissue toxicity and maintaining equivalent  
 666 tumor damage. The response to dose can be described by the survival fraction probability,  
 667 describing the fraction of surviving cell as a function of the dose:

$$S(D) = S(0) e^{-(\alpha D + \beta D^2)} \quad (3.1)$$

668 where  $\alpha$  and  $\beta$  respectively represents the rate of cell killing by single ionizing events and  
 669 by double hits. Hence, at high doses the density of damages increases and the cells repair  
 670 becomes more difficult. Even if the FLASH effect is not yet completely understood and  
 671 the underlying mechanisms are not clear, it looks like there are two different recipes which  
 672 are involved:

- 673 • **The dose rate:** higher dose rate produce bigger damages (fig. 3.6(a)) since this  
 674 prevent cells from sparing.
- 675 • **The presence or absence of oxygen:** while hypoxic cells are very resistant to radi-  
 676 ation, normal oxygenated cells are highly radiosensitive. This is because if molecules  
 677 containing  $O_2$  break due to the impinging radiation, then the oxygen can build Re-  
 678 active Oxygen Species (ROS) (fig.3.6(b))

679 The Tumor Control Probability (TCP) and the Normal Tissue Complication (NTC) func-  
 680 tions parametrize respectively the efficiency of damaging on the tumor after having released  
 681 a certain dose and the probability of not affecting the healthy tissues. The intermediate  
 682 zone between the increase of the TC and of the NTC is called therapeutic window, and  
 683 the wider it is and the more effective the treatment is.

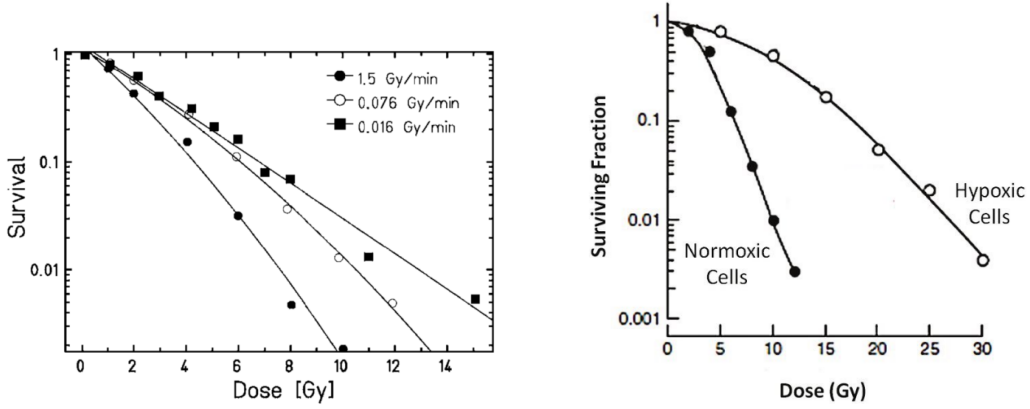


Figure 3.6: (a) Survival curve for different dose rate and (b) for different oxygen cell content

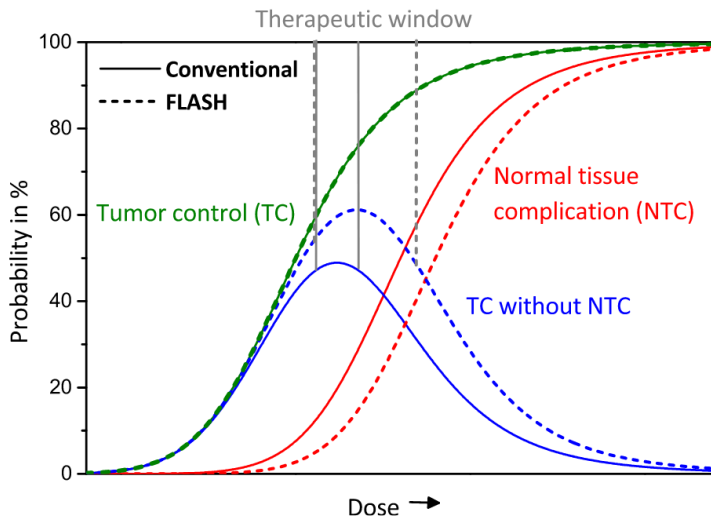


Figure 3.7: Illustration of dependence of TCP, NTCP and therapeutic window on dose, for CONV-RT ad FLASH-RT.

#### 684 Dosimetric problems

685 Up to now, all online dosimeters have shown saturation problems at high DDP, differently  
 686 from radiochromic films, which are the standard passive dosimeters and have shown a  
 687 dose-rate independence up to 100 Gy/s. Even though the linear response in wide dynamic  
 688 range, they do not provide any online dosimetric informations, since the time required to  
 689 extract the physical value from the reading is not instantaneous<sup>4</sup>.

690 Ionization Chambers (ICs), which are the online reference dosimeter also according  
 691 to law protocols, at high level of radiation (already at dose per pulse two orders of mag-  
 692 nitude lower than the ones used for FLASH-RT) show both problems of saturation and  
 693 recombination. When a high density of ions and electrons is produced in the gas, a high  
 694 counter electric field opposed to the drift one might be generated; if a neutral region build  
 695 up, both the recombination of i/e pairs, with a subsequent photoemission and abrupt dis-  
 696 charge can happen. A correction factors,  $k_{sat}$ , can be introduced for sufficient low level of  
 697 radiation and in this case a precise dose measurement can still be done: under conventional

<sup>4</sup>The radiation produces a polymerization of an active layer, resulting in a different density of coloration.

Commercial detector	Detector type	saturation [Gy/p]
PTW TW34045 Advanced Markus EC	ionization chamber	0.3
PTW TM60017 Dosimetry Diode E	silicon diode	0.15
PTW TW60019 microDiamond	diamond	0.15
DoseVue DoseWireTM Series 100	scintillator fiber	11-26

Table 3.2: Results obtain in [10]

698 operation, with Dose Per Pulse (DDP) lower than 1 mGy the correction factor is <5%.

699 Concerning the conventional semiconductor, if exposed to high dose rate, they suffer  
700 of saturation problems just as the ICs, but thin sensors as silicon MAPS are expected  
701 to reduce the saturation problem. Indeed a thin planar sensor could allow for a constant  
702 electric field even at high dose rate which, together with the short mean path the e/h must  
703 cover to get the electrode (the epitaxial layer typically is  $\sim 30 \mu\text{m}$ ), could result in a non-  
704 saturated response of the signal. Besides the thinness, also the small capacity typical of  
705 MAPS is beneficial for reducing the readout time: a reduced  $C_d$  enables for a fast discharge  
706 and then for a fast readout. Finally, the high spatial resolution requirement obviously  
707 imposed by beam monitor is one of the main reasons which makes MAPS attractive.  
708 Among the semiconductors, also diamond detectors present a high promising alternative  
709 thanks to their high radiation hardness, response stability and linearity in a wide range.  
710 Also other detector types, such as plastic scintillators, optical fiber and alanine dosimeters  
711 have been proposed for high dose environments and many groups are going on studies on  
712 their applicability on FLASH-RT.

713 In reference [10] are presented some results related with saturation problems at high  
714 DDP of different types of detectors. The dosimeters tested and their value at which satura-  
715 tion becomes are reported in table 3.2, while in figure 3.8 are reported the measurements.  
716 The DrR is then defined as the ratio between the signal response of each dosimeters at a  
717 fixed DDP of 1 cGy/p and is called dosimeter reading ratio (DrR):

$$DrR = \frac{R}{R|_{Dp=1cGy/p}} = \frac{R}{R_{ref}} \quad (3.2)$$

718 Then, for a saturation not affected by saturation problems DrR should be a straight line  
719 with a slope equal to 1; since the reference measurements of dose has been performed with  
720 radiochromic films (GAFCHROMIC EBT-XD), whose dose indipendece has been tested<sup>5</sup>  
721 in range from 0 Gy to 15 Gy, the dotted black line in figure 3.8 represents the reference  
722 measurment done with it.

---

<sup>5</sup>The radiochromic films calibration has been obtained by irradiating the films with dose values in range from 0 Gy to 15 Gy, by positioning the films in a polymethylmethacrylate (PMMA) phantom at  $R_{100}$  depth, corresponding to 10 cm

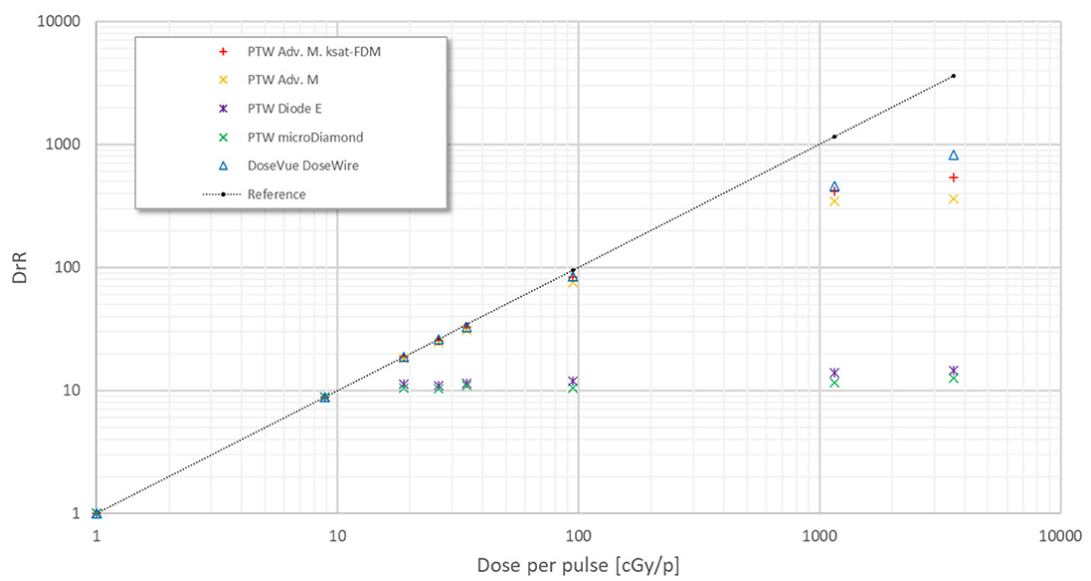


Figure 3.8: Saturation problems underlyed in [10].

<sup>723</sup> **Chapter 4**

<sup>724</sup> **TJ-Monopix1**

<sup>725</sup> TJ-Monopix1 is a small electrode DMAPS with fast R/O capability, fabricated by Tow-  
<sup>726</sup> erJazz foundry in 180 nm CMOS imaging process. It is part, together with prototypes  
<sup>727</sup> from other series such as TJ-MALTA, of the ongoing R&D efforts aimed at developing  
<sup>728</sup> DMAPS in commercial CMOS processes, that could cope with the requirements at ac-  
<sup>729</sup> celerator experiments. Both TJ-Monopix and TJ-MALTA series [11], produced with the  
<sup>730</sup> same technology by TowerJazz (the timeline of the foundry products is shown in figure  
<sup>731</sup> 4.1), are small electrode demonstrators and principally differ in the readout design: while  
<sup>732</sup> Monopix implements a column-drain R/O, an asynchronous R/O without any distribution  
<sup>733</sup> of BCID has been used by TJ-Malta in order to reduce power consumption.



Figure 4.1: Timeline in TowerJazz productions in 180 nm CMOS imaging process

<sup>734</sup> Another Monopix series, but in 150 nm CMOS technology, has been produced by  
<sup>735</sup> LFoundry [12]. The main differences between the LF-Monopix1 and the TJ-Monopix1  
<sup>736</sup> (summarized in table 4.2), lay in the sensor rather than in the readout architecture, as  
<sup>737</sup> both chips implements a fast column drain R/O with ToT capability [13][14]. Concerning  
<sup>738</sup> the sensors, either are based on a p-type substrate, but with slightly different resistivities;  
<sup>739</sup> in addition LFoundry pixels are larger, thicker and have a large fill factor (the very deep n-  
<sup>740</sup> well covers ~55% of the pixel area). The primary consequence is that LF-Monopix1 pixels  
<sup>741</sup> have a higher capacity resulting in higher consumption and noise. As I discussed in section  
<sup>742</sup> 2.4.1, the fact that LF-Monopix has a large fill factor electrode is expected to improve its  
<sup>743</sup> radiation hardness. Indeed, a comparison of the performance of the two chips showed that  
<sup>744</sup> TJ-Monopix suffers a comparatively larger degradation of efficiency after irradiation, due  
<sup>745</sup> to the low electric field in the pixel corner; on the other hand, a drawback of the large fill  
<sup>746</sup> factor in LF-Monopix is a significant cross-talk.

	LF-Monopix1	TJ-Monopix1
Resistivity	$>2 \text{ k}\Omega\text{cm}$	$>1 \text{ k}\Omega\text{cm}$
Pixel size	$50 \times 250 \mu\text{m}^2$	$36 \times 40 \mu\text{m}^2$
Depth	$100\text{-}750 \mu\text{m}$	$25 \mu\text{m}$
Capacity	$\sim 400 \text{ fF}$	$\sim 3 \text{ fF}$
Preamplifier	charge	voltage
Threshold trimming	on pixel (4-bit DAC)	global threshold
ToT	8 bits	6 bits
Consumption	$\sim 300 \text{ mW/cm}^2$	$\sim 120 \text{ mW/cm}^2$
Threshold	$1500 e^-$	$\sim 270 e^-$
ENC	$100 e^-$	$\sim 30 e^-$

Table 4.1: Main characteristics of Monopix1 produced by TowerJazz and LFoundry [13][14]

747        The TJ-Monopix1 chip contains, apart from the pixels matrix, all the required support  
 748        blocks used for configuration and testing:

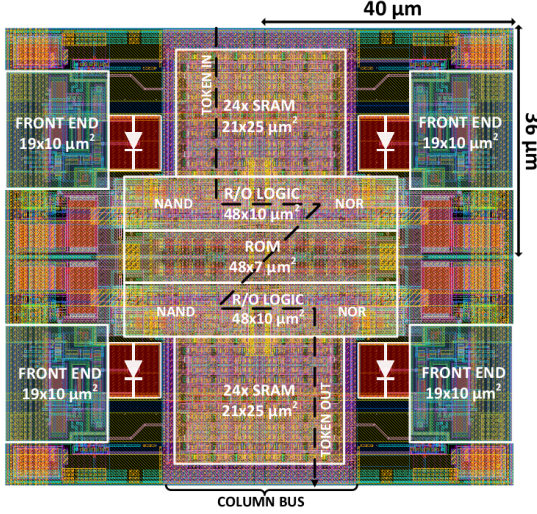
- 749        • the whole matrix contains  $224 \times 448$  pixels, yielding a total active area approximately  
 750        equal to  $145 \text{ mm}^2$  over a total area of  $1 \times 2 \text{ cm}^2$ ;
- 751        • at the chip periphery are placed some 7-bit Digital to Analog Converter (DAC), used  
 752        to generate the analog bias voltage and current levels and to configuire the FE;
- 753        • at the EoC is placed a serializer to transferred datas immediately, indeed no trigger  
 754        memory is implemented in this prototypes;
- 755        • the matrix power pads are distributed at the sides
- 756        • four pixels which have analog output and which can be monitored with an oscillo-  
 757        scope, and therefore used for testing

758        Pixels are grouped in  $2 \times 2$  cores (fig. 4.2a): this layout allows to separate the analog  
 759        and the digital electronics area in order to reduce the possible interference between the  
 760        two parts. In addition it semplifies the routing of data as pixels on double column share  
 761        the same column-bus to EoC. Therefore pixels can be addressed through the physical  
 762        column/row or through the logical column/row, as shown in fig. 4.2b: in figure is also  
 763        highlighted the token propagaion path, whose I will discuss later.

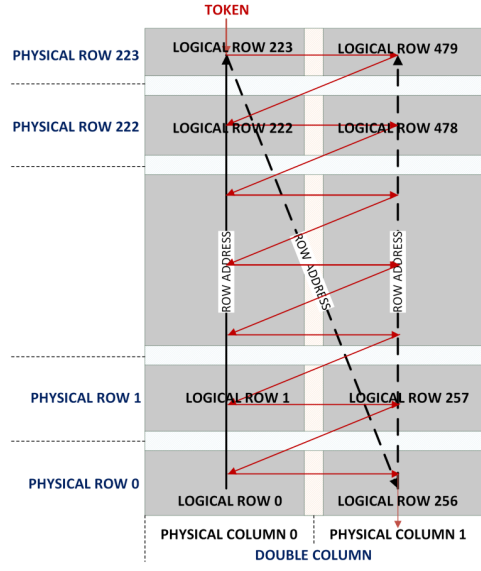
764        Concerning the integration7.7 of the chip in a readout path, TJ-Monopix1 chips have  
 765        been wire-bonded on a dedicated carrier board , the Printed Circuit Board (PCB). Two  
 766        other board between the DAQ and the chip: the General Purpose Analog Card (GPAC),  
 767        which provides power supply channels, current/voltage bias sources and I/O buffer, and  
 768        the MIO3 FPGA, which strictly interacts with the DAQ.

## 769        4.1 The sensor

770        As already anticipated, TJ-Monopix1 has a p-type epitaxial layer and a n doped small  
 771        collection electrode ( $2 \mu\text{m}$  in diameter); to avoid the n-wells housing the PMOS transistors  
 772        competing for the charge collection, a deep p-well substrate, common to all the pixel FE



(a) Layout of a core containing 4 pixels. The analog FE and the digital part are separated in order to reduce cross-talk be



(b)

Parameter	Value
Matrix size	$1 \times 2 \text{ cm}^2$
Pixel size	$36 \times 40 \mu\text{m}^2$
Depth	$25 \mu\text{m}$
Electrode size	$2 \mu\text{m}$
BCID	40 MHz
ToT-bit	6
Power consumption	$\sim 120 \text{ mW/cm}^2$

Table 4.2

area, is used. TJ-Monopix1 adopts the modification described in section 2.4.2 that allows to achieve a planar depletion region near the electrode applying a relatively small reverse bias voltage. This modification improves the efficiency of the detector, especially after irradiation, however a simulation of the electric field in the sensor, made with the software TCAD (Technology Computer Aided Design), shows that a nonuniform field is still produced in the lateral regions of the pixel compromising the efficiency at the corner. Two variations to the process have been proposed in order to further enhance the transversal component of electric field at the pixel borders: on a sample of chip, which includes the one in Pisa, a portion of low dose implant has been removed, creating a step discontinuity in the deep p-well corner (fig. 4.3); the second solution proposed[MOUSTAKAS THESY, PAG 58] consists in adding an extra deep p-well near the pixel edge. A side effect of the alteration in the low dose implant is that the separation between the deep p-well and the p-substrate becomes weak to the point that they cannot be biased separately to prevent the punchthrough.

Moreover, to investigate the charge collection properties, pixels within the matrix are split between bottom top half and bottom half and feature a variation in the coverage of the deep p-well: the electronics area can be fully covered or not. In particular the pixels

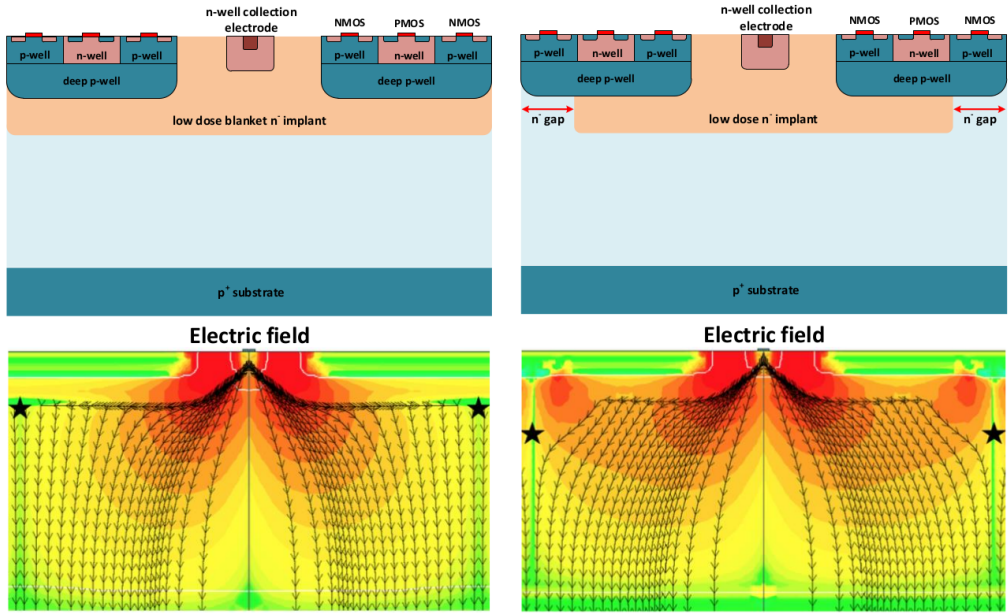


Figure 4.3: (a) The cross-section of a monolithic pixel in the TJ-Monopix with modified process; additionally in (b) a gap in the low dose implant is created to improve the collection of charge due to a bigger lateral component of the electric field. this point in figure is indicated by a star . transversal component of the electric field drops at the pixel corner

790 belonging to rows from 0 to 111 are fully covered (FDPW) and pixels belonging to rows  
 791 from 112 to 223 have a reduced p-well (RDPW), resulting in a enhancement of the lateral  
 792 component of the electric field.

## 793 4.2 Front end

794 One of the main advantage of this chip is the small collection electrode, which results in a  
 795 small capacitance ( $C_{in}=3\text{ fF}$ ) allowing for high input signal amplitude and single stage of  
 796 amplification, which obviously improves the signal to noise ratio performance of the FE.  
 797 Assuming a fully depleted epitaxial layer of  $25\text{ }\mu\text{m}$ , which corresponds approximately to  
 798 a  $20\text{ }\mu\text{m}$  of deep sensing volume, a MIP should produce  $\sim 1600\text{ e}^-$ , then:

$$V_{in} = \frac{1600\text{ e}^- \times 1.6 \cdot 10^{-19}\text{ C}}{3\text{ fF}} = 85\text{ mV} \quad (4.1)$$

799 Secondly, a reset mechanism which slowly discharges the detector capacitance must be  
 800 included in the circuit:

$$V_{in} = \frac{Q_s}{C_{in}} e^{-t/R_b C_{in}} \quad (4.2)$$

801 where  $R_b$  is the equivalent reset element. The general constraint which must be satisfied  
 802 is that the discharge time  $\tau = R_b C_{in}$  must be slower than the characteristic time of  
 803 the amplifier, otherwise a signal loss could occurs. Traditionally the reset can be  
 804 implemented in two different way: with a forward biased diode, that might be implemented  
 805 by a simple p+ diffusion inside the well of the collection electrode n, or with a PMOS  
 806 transistor. Despite of the semplicity of the diode reset, since it is a non-linear element,  
 807 the discharge would depend on the quantity of charge Q generated on the n electrode,

808 prejudicing the linearity of the analog output (Q-ToT). To solve the issue, a PMOS reset  
 809 is the method preferred in design such TJ-Monopix1 with analog output; the PMOS  
 810 transistor, indeed, can acts as a constant current source and then used to discharge the  
 811 sensor. Although the PMOS reset is capable of providing a constant current, it has to be  
 812 manually re-tuned every time in order to restore the input DC baseline voltage; to do that  
 813 a low-frequency feedback is used.

814 The matrix is split in four sections, each one corresponding to a different flavor of the  
 FE, implemented in order to test more options.

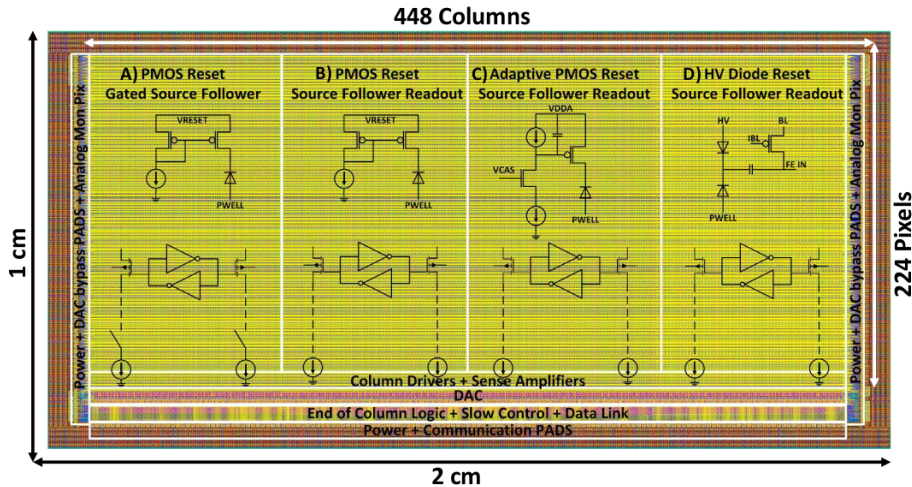


Figure 4.4: TJ-Monopix1 has been developed in four different flavor. The flavor PMOS reset (B) is considered as the reference one.

815  
 816 All the flavors implement a source-follower double-column bus readout: the standard  
 817 variation is the flavor B, that features a PMOS input reset (refered as "PMOS reset").  
 818 Flavor A is identical to flavor B except for the realization of the source follower (it is a  
 819 gated one): in the circuit of the gated versione there is a transistor more that operates on  
 820 the baseline and on the feedback mechanism; this aim to reduce the power consumption  
 821 and results in a higher signal baseline, and then in a lower effective threshold. C instead  
 822 implements a novel leakage compensation circuit, with a PMOS reset configuration. More-  
 823 over the collection electrode can be either DC-coupled to the readout electronics, as in  
 824 flavors A, B, C, or AC-coupled through a metal-oxide-metal (MOM) capacitor, as in D  
 825 is AC-coupled. The latter one allows applying a high bias voltage to the electrode n and  
 826 for this reason the flavor D is also called "HV flavor". Unfortunately the "HV" suffer  
 827 from a signal loss, which can achieve even the 50%, due to the additional parasitic capac-  
 828 ity introduced at the input node. The HV voltage above which the breakdown begins is  
 829  $\sim 50$  V; however at values bigger than 20 V, the gain does not increase anymore, since the  
 830 depletion zone is already fully depleted.

#### 831 4.2.1 ALPIDE-like

832 ALPIDE chips, developed by the ALICE collaboration, implemented a standard FE to the  
 833 point that many CMOS MAPS detectors used a similar FE and are called "ALIPDE-like".  
 834 Considering that both TJ-Monopix1 and ARCADIA-MD1 have an ALPIDE-like FE, I am  
 835 going to explain the broad principles of the early FE stage. The general idea is of the  
 836 amplification to transfer the charge from a bigger capacity[15],  $C_{source}$ , to a smaller one,

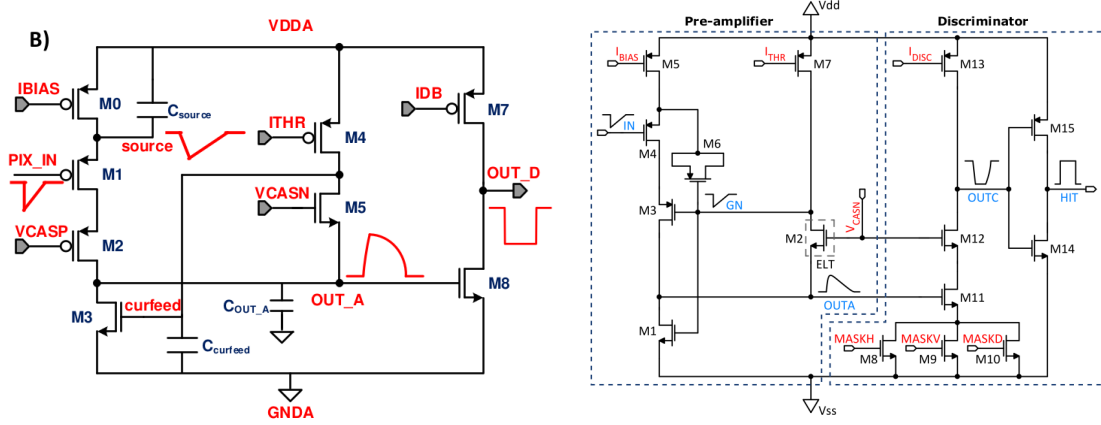


Figure 4.5

837  $C_{out}$ : the input transistor M1 with current source IBIAS acts as a source follower and this  
 838 forces the source of M1 to be equal to the gate input  $\Delta V_{PIX\_IN} = Q_{IN}/C_{IN}$ .

$$Q_{source} = C_{source} \Delta V_{PIX\_IN} \quad (4.3)$$

839 The current in M2 and the charge accumulates on  $C_{out}$  is fixed by the one on  $C_{source}$ :

$$\Delta V_{OUT\_A} = \frac{Q_{source}}{C_{OUT\_A}} = \frac{C_{source} \Delta V_{PIX\_IN}}{C_{OUT\_A}} = \frac{C_{Source}}{C_{OUT\_A}} \frac{Q_{IN}}{C_{IN}} \quad (4.4)$$

840 A second branch (M4, M5) is used to generate a low frequency feedback, where VCASN  
 841 and ITHR set the baseline value of the signal on  $C_{OUT\_A}$  and the velocity to goes down  
 842 to the baseline. **IL RUOLO DI CURVFEED NON L'HO CAPITO.** Finally IDB defines  
 843 the charge threshold with which the signal  $OUT\_A$  must be compared: depending on if  
 844 the signal is higher than the threshold or not, the  $OUT\_D$  is high or low respectively.

845 The actual circuit implemented in TJ-Monopix1 is shown in figure 4.5: the principal  
 846 difference lays in the addition of disableing pixels' readout. This possibility is uttermost  
 847 important in order to reduce the hit rate and to avoid saturating the bandwidth due to the  
 848 noisy pixels, which typically are those with manufacturing defects. In the circuit transis-  
 849 tors M8, M9 and M10 have the function of disabling registers with coordinates MASKH,  
 850 MASKV and MASKD (respectively vertical, orizontal and diagonal) from readout: if all  
 851 three transistors-signals are low, the pixel's discriminator is disabled. Compared with a  
 852 configurable masking register which would allow disableing pixels individually, to use a  
 853 triple redundancy reduces the sensistivity to SEU but also gives amount of intentionally  
 854 masked ("ghost") pixels. This approach is suitable only for extremely small number N of  
 855 pixel has to be masked: if two coordinate projection scheme had been implemented, the  
 856 number of ghost pixels would have scale with  $N^2$ , if instead three coordinates are used,  
 857 the N's exponential is lower than 2 (fig. 4.6)

858 Foto dell'oscilloscopio per far vedere cosa fanno i parametri

### 859 4.3 Readout logic

860 TJ-Monopix1 has a triggerless, fast and with ToT capability R/O which is based on a  
 861 column-drain architecture. On the pixel are located two Random Access Memory (RAM)  
 862 cells to store the 6-bit LE and 6-bit TE of the pulse, and a Read-Only Memory (ROM)

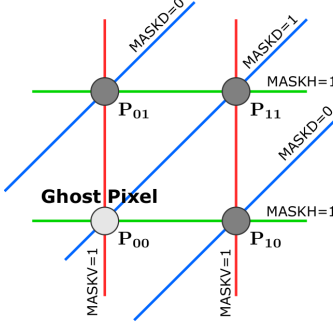


Figure 4.6

Parameter	Meaning	
IBIAS	mainly controls the rise time	yes
IDB	sets the discriminator threshold	yes
ITHR	sets the velocity of the return to the baseline	yes
ICASN	sets the baseline of the signal	yes
VRESET	sets the gain of the preamplifier	yes
IRESET	sets the gain of the preamplifier	no

Table 4.3: FE parameters which must be setted through the DAQ. "Function" means that higher parameter implies higher value

863 containing the 9-bit pixel address. Excluded these memories, TJ-Monopix1 hasn't any  
 864 other buffer: if a hit arrives while the pixel is already storing a previous one, the new  
 865 data get lost. After being read, the data packet is sent to the EoC periphery of the  
 866 matrix, where a serializer transfers it off-chip to an FPGA (4.7). There a FIFO is used  
 867 to temporarily stored the data, which is transmitted to a computer through an ethernet  
 868 cable in a later time.

869 The access to the pixels' memory and the transmission of the data to the EoC, following  
 870 a priority chain, is managed by control signals and is based on a Finite State Machine  
 871 (FSM) composed by four state: no-operation (NOP), freeze (FRZ), read (RD) and data  
 872 transfer (DTA). The readout sequence (??) starts with the TE of a pulse: the pixel  
 873 immediately tries to grab the column-bus turning up a hit flag signal called *token*. The  
 874 token is used to control the priority chain and propagates across the column indicating  
 875 what pixel that must be read. To start the readout and avoid that the arrival of new hits  
 876 disrupt the priority logic, a *freeze* signal is activated, and then a *read* signal controls the  
 877 readout and the access to memory. During the freeze, the state of the token for all pixels  
 878 on the matrix remains settled: this does not forbid new hits on other pixels from being  
 879 recorded, but forbids pixels hit from turning on the token until the freeze is ended. The  
 880 freeze stays on until the token covers the whole priority chain and gets the EoC: during  
 881 that time new token cannot be turned on, and all hits arrived during a freeze will turn  
 882 on their token at the end of the previous freeze. Since the start of the token is used to  
 883 assign a timestamp to the hit, the token time has a direct impact on the time resolution  
 884 measurement; this could be a problem coping with high hits rate.

885 The analog FE circuit and the pixel control logic are connected by an edge detector  
 886 which is used to determine the LE and the TE of the hit pulse(fig. 4.9): when the TE

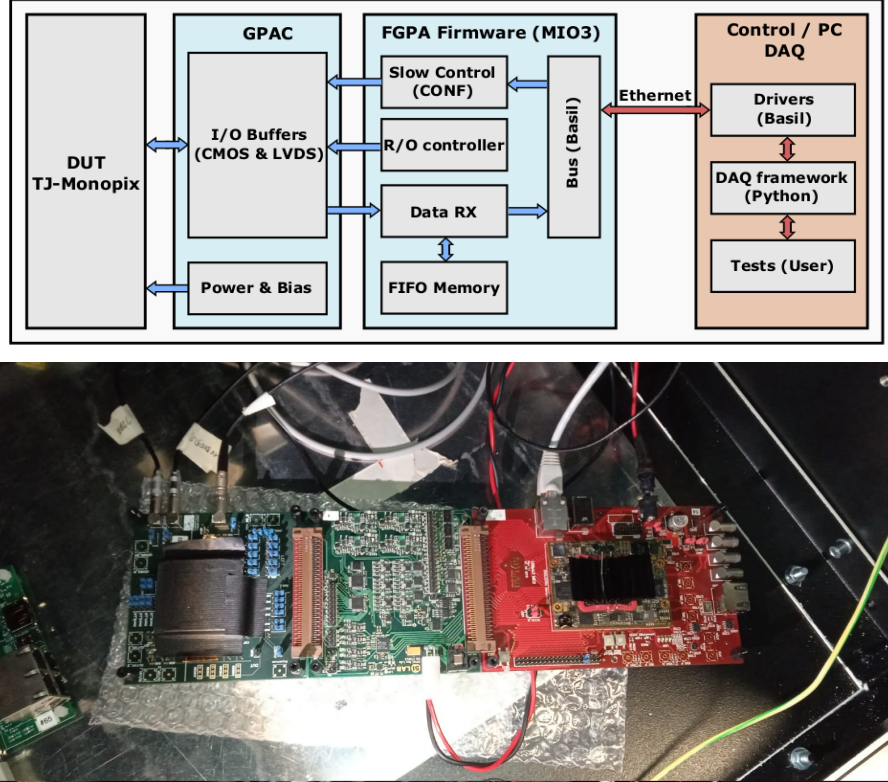


Figure 4.7: Main caption

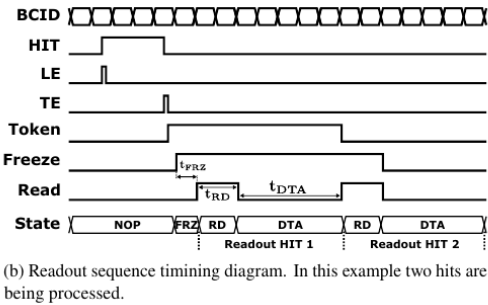


Figure 4.8: Readout timing diagram: in this example two hits are being processed

887 is stored in the first latch the edge detector is disabled and, if the **FREEZE** signal is not  
 888 set yet, the readout starts. At this point the **HIT** flag is set in a second latch and a **Token**  
 889 signal is produced and depending on the value of **Token** in the pixel can be read or must  
 890 wait until the **Token in** is off. In figure an OR is used to manage the token propagation, but  
 891 since a native OR logic port cannot be implemented with CMOS logic, a sum of a NOR  
 892 and of an inverter is actually used; this construct significantly increases the propagation  
 893 delay (the timing dispersion along a column of 0.1-0.2 ns) of the token and to speed up  
 894 the circuit optimized solution are often implemented. When the pixel become the next to  
 895 be read in the queue, and at the rising edge of the **READ** signal, the state of the pixel is  
 896 stored in a D-latch and the pixel is allowed to use the data bus; the **TE** and the **HIT** flag  
 897 latches are reset and a **READINT** signal that enable access of the RAM and ROM cells  
 898 is produced.

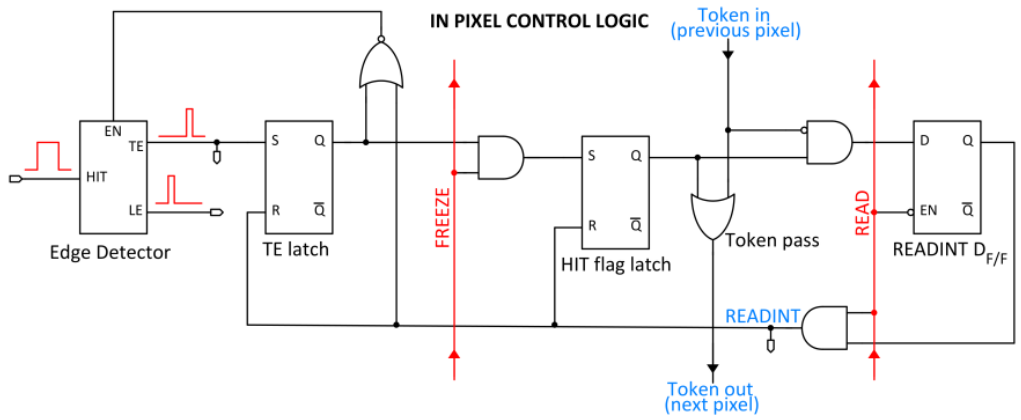


Figure 4.9

899        The final data must provide all the hits' information: the pixel address, the ToT and  
 900        the timestamp. All those parts are assigned and appended at different time during the  
 901        R/O chain:

- 902        • **Pixel address:** while the double column address (6-bit) is appended by the EoC  
 903        circuit, the row address (8-bits for each flavor) and the physical column in the doublet  
 904        (1-bit) are assigned by the in-pixel logic
- 905        • **ToT:** is obtained offline from the difference of 6-bits TE and 6-bits LE, stored by  
 906        the edge detector in-pixel; since a 40 MHz BCID is distributed across the matrix,  
 907        the ToT value is range 0-64 clock cycle which corresponds to 0-1.6  $\mu$ s
- 908        • **Timestamp:** The timestamp of the hit correspond to the time when the pixel set  
 909        up the token; it is assigned by the FPGA, that uses the LE, TE and a 640 MHz  
 910        clock to derive it. For all those hits which arrived while the matrix is frozen, the  
 911        timestamp is no more correlated with the time of arrival of the particle

912        When the bits are joined up together the complete hit data packet is 27-bit.

913 **Chapter 5**

914 **Arcadia-MD1**

915 [16] [17]

916 Breve introduzione analoga a Monopix1 in cui descrivo brevemente la "timeline" da  
917 SEED Matisse a Md1 e Md2

918 Tutti i minid, siano essi v1 o v2, sono Alpide like. Prima SEED si occupa di stu-  
919 diare le prestazioni: concept study with small-scale test structure (SEED), dopo arcadia:  
920 technology demonstration with large area sensors Small scale demo SEED(sensor with em-  
921 bedded electronic developement) Quanto spazio dato all'elettronica sopra il pwell e quanto  
922 al diodo. ..

923 **5.1 The sensor**

924 ARCADIA-MD1 is an LFoundry chip which implements the technology 110 nm CMOS  
925 node with six metal layer ??. The standard p-type substrate was replaced with an n-type  
926 floating zone material, that is a tecnique to produce purified silicon crystal. (pag 299  
927 K.W.).

928 Tra i wafer fabbricati finora ci sono 3 valori di spessore attivo nominale (lo spessore  
929 effettivo può variare di qualche micron ripetto a quello nominale): 48um, 100um e 200um.  
930 In allegato un'immagine con le cross section.

931 Wafer thinning and backside lithography were necessary to introduce a junction at the  
932 bottom surface, used to bias the substrate to full depletion while maintaining a low voltage  
933 at the front side.

934 C'è un deep pwell per - priority chain separare l'elettronica dal sensore; per controllare il  
935 punchthought è stato aggiunto un n doped epitaxial layer having a resistivity lower than  
936 the substrate. It is part of the cathegory of DMAPS Small electrode to enhance the signal

Parameter	Value
Matrix size	$\times \text{ cm}^2$
Pixel size	$25 \times 25 \mu\text{m}^2$
Depth	? $\mu\text{m}$
Electrode size	$9 \times 9 \mu\text{m}^2$
Power consumption	$\sim \text{ mW/cm}^2$

Table 5.1

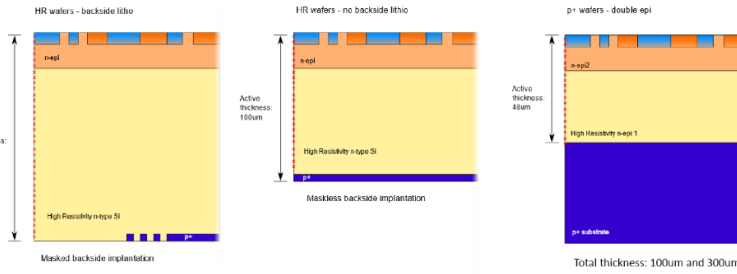


Figure 5.1

937 to noise ratio. It is operated in full depletion with fast charge collection by drift.

### 938 5.1.1 Two different FE flavor

939 Le differenze tra Alpide e bulk driven sono un po' più complesse di quanto hai scritto.  
 940 Si tratta proprio di due architetture diverse. Il primo amplifica il segnale attraverso il  
 941 trasferimento di carica tra due capacità. Nel bulk driven invece il guadagno è dato dal  
 942 rapporto tra due transconduttanze. Inoltre ci sono altre differenze, il bulk driven è più  
 943 sensibile alle cadute di tensione sul ground (che ahimè è esattamente ciò che accade nei  
 944 dimostratori che abbiamo ora, a causa dell'anomalo consumo di corrente dal digitale,  
 945 altro baco che abbiamo corretto nella terza sottomissione). Anche i livelli di tensione nei  
 946 nodi interni dei due front-end differiscono e il meccanismo di clipping che funzionava per  
 947 l'Alpide non è applicabile al bulk driven. Di conseguenza abbiamo un bias in più (ICLIP)  
 948 nel secondo flavour per controllare il clipping. Nell'Alpide il clipping c'è, ma l'architettura  
 949 usata permette di non aver bisogno di un bias esterno, anche se in una versione di Alpide  
 950 di ALICE hanno scelto di controllare comunque la corrente di clip esternamente, per una  
 951 maggiore flessibilità. Infine alcuni bias che hanno lo stesso nome nei due flavour, perché  
 952 svolgono la stessa funzione, differiscono nel valore di configurazione didefault.

## 953 5.2 Readout logic and data structure

954 In order to achieve the lowest possible power consumption, the matrix is clockless, no  
 955 free-running clock, and to save as much area as possible, it will not buffer any hits, and  
 956 its readout will thus be triggerless.

957 The Periphery has both an analog part, segmented per Section, and a digital part,  
 958 which is instead shared. The analog part hosts the bias cells for the AFE dei pixel, mentre  
 959 la parte digitale che è unica per tutti riprocesso le hit che vengono dalle sezioni e 8b10b  
 960 encode le parole per data transmission.

### 961 5.2.1 Matrix division and data-packets

962 The matrix is divided into an internal physical and logical hierarchy: The 512 columns are  
 963 divided in 16 section:  $512 \times 32$  pixels, each section has different voltage-bias + serializzatori.  
 964 Each section is devided  $512 \times 2$  column, and in  $32 \times 2$  core: in modo che in ogni doppia  
 965 colonna ci siano 1Pacchetto dei dati 6 cores. ricordati dei serializzatori: sono 16 ma  
 966 possono essere ridotti ad uno in modalità spazio Ed infine regioni da  $4 \times 2$ . The readout  
 967 design must be capable of addressing the following matters Enough bus bandwidth for a

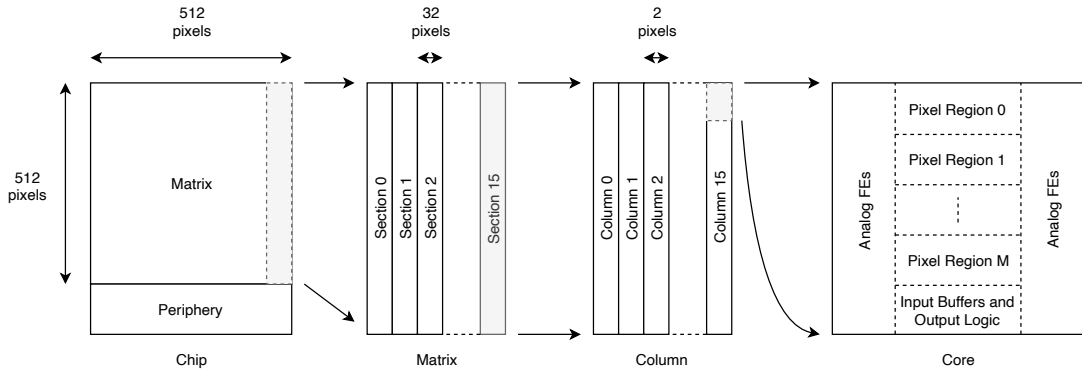


Figure 5.2

hit rate of 100 MHz/cm<sup>2</sup>. Design decisions: Try and send as much data as possible to the periphery (bandwidth) Lowest amount of logic possible (more routability)

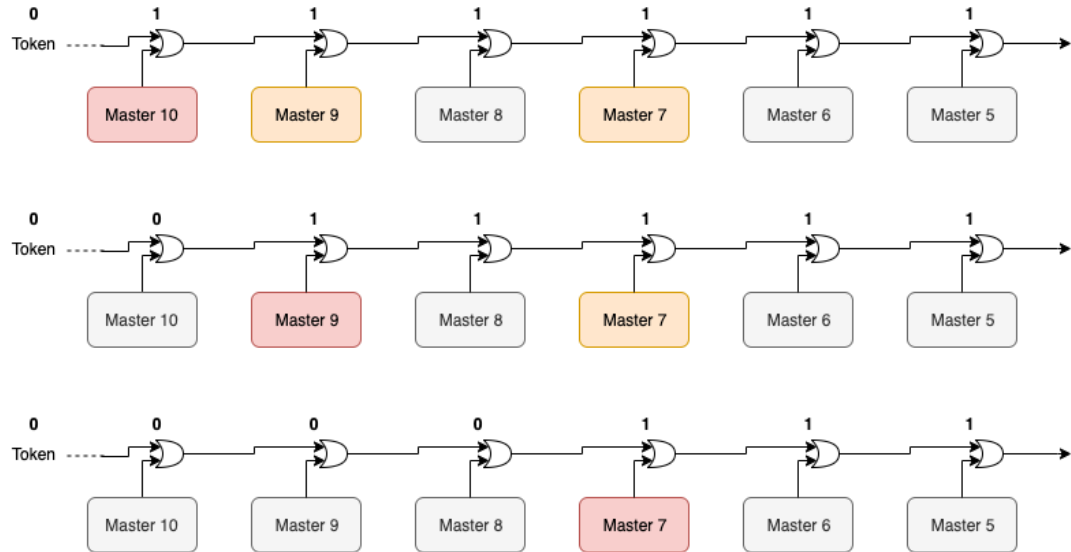


Figure 5.3

Questo divisione si rispecchia in come sono fatti i dati: scrivi da quanti bit un dato è fatto e le varie coordinate che ci si trovano dentro; devi dire che c'è un pixel hot e spieghi dopo a cosa serve, e devi accennare al timestamp

"A core is simply the smallest stepped and repeated instance of digital circuitry. A relatively large core allows one to take full advantage of digital synthesis tools to implement complex functionality in the pixel matrix, sharing resources among many pixels as needed.". pagina 28 della review.

977

978 TABELLA: con la gerarchia del chip Matrix (512x512 pixels) Section (512x32 pixels)  
979 Column (512x2) Core (32x2) Region (4x2)

980 Nel chip trovi diverse padframe: cosa c'è nelle padframe e End of section.

981 "DC-balance avoids low frequencies by guaranteeing at least one transition every n  
982 bits; for example 8b10b encoding n =5"

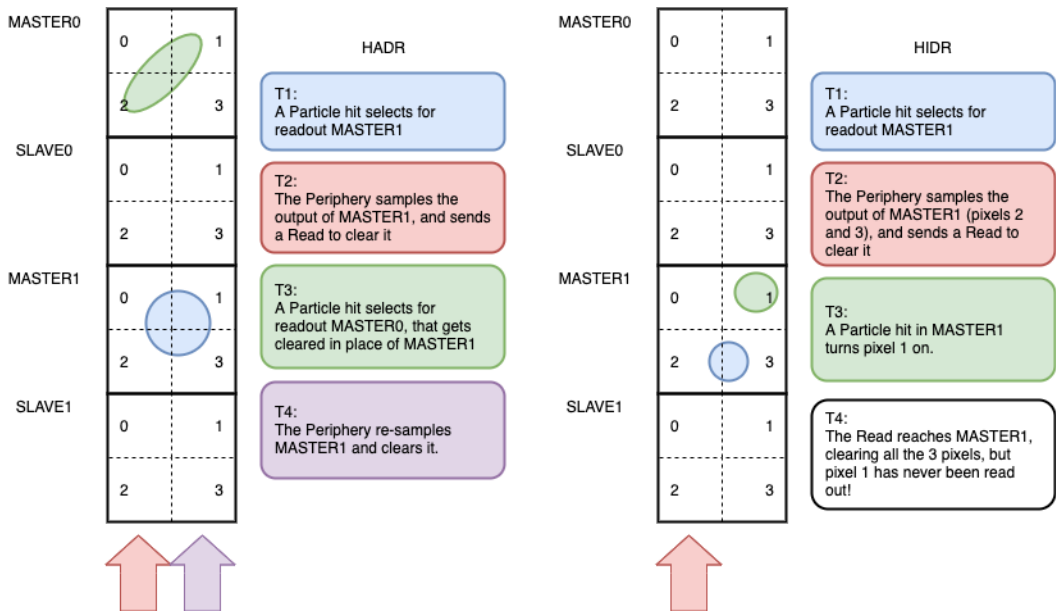


Figure 5.4

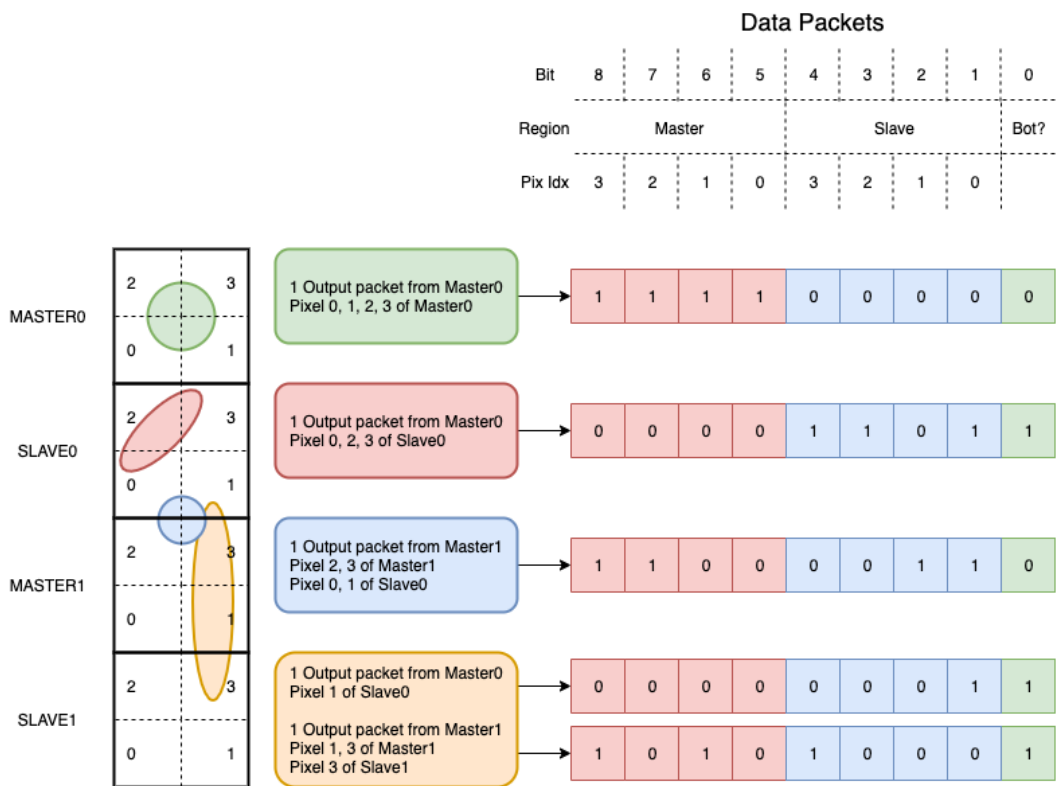


Figure 5.5

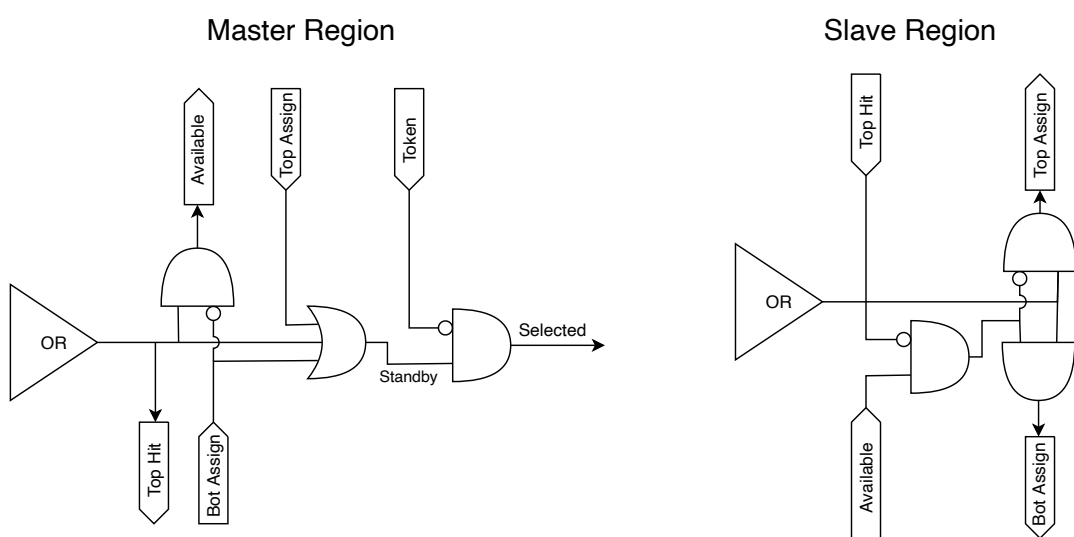


Figure 5.6

983    **Chapter 6**

984    **Characterization**

985

- 986    • rifai il conto della lunghezza di attenuazione. Ho trovato (presentazione Luciano  
987    Mus) 29 um per ka e 37 um per kb.
- 988    • Con il PMOS la configurazione del FE di default è: e richiama i significati delle  
989    variabili.
- 990    • parla dell HV

991    **6.1 TJ-Monopix1 characterization**

992    **6.1.1 Threshold and noise: figure of merit for pixel detectors**

993    A characterization of threshold and noise is typically necessary since these values have an  
994    impact on the operating conditions and on the performance of the chips, so much that  
995    the signal to threshold ratio may be considered as the figure of merit for pixel detectors  
996    rather than the signal to noise ratio. The mean minimum stable threshold evolved through  
997    different generation of chips: in the 1st generation it was around  $2500 \text{ e}^-$  while in the 3rd  
998    (corresponding to nowadays chips) is less than  $500 \text{ e}^-$ . This allows in thinner sensors with  
999    smaller signals: from  $16\,000 \text{ e}^-$  produced in  $200 \mu\text{m}$ , the signal expected moved down to  
1000     $2000 \text{ e}^-$  produced in  $25 \mu\text{m}$ . According with this, the threshold of TJ-Monopix1 is around  
1001     $500 \text{ e}^-$ .

1002    Obviously the threshold has to be located between the noise peak around the baseline  
1003    and the signal distribution, in particular it has to be low enough to mantain a high signal  
1004    efficiency, but also high enough to cut the noise: for a low threshold many pixels can fire  
1005    at the same time and a positive feedback can set off a chain reaction eventually, causing  
1006    all the other pixels to fire. Thus, the noise sets a lower bound to the threshold: if an  
1007    occupancy  $\leq 10^{-4}$  is required, for example, this correspond to the Gaussian 1-sided tail  
1008    fraction for  $3.7\sigma$ . In this case, if the noise is  $100 \text{ e}^-$  (resonable), the threshold must be  
1009    higher than  $3.7 \times 100 \text{ e}^-$ . Typically this argument sets only a minimal bound to the  
1010    threshold since the variation with time and from pixel to pixel have to be taken into  
1011    account: the temperature, the annealing (for example, the radiation damages in the oxide  
1012    layer causes shift of MOSFET threshold voltage) and the process parameters variation  
1013    across the wafer (as for example process mismatch between transistors).

Given that the first stage of amplification is the most crucial, since in the following stages the signal amplitude is high compared to additional noise, the noise is valued at the preamplifier input node. Then, the noise is parameterized as Equivalent Noise Charge (ENC), which is defined as the ratio between the noise N at the output expressed in Volt and the out voltage signal S produced by 1 e<sup>-</sup> entering in the preamplifier:

$$ENC = \frac{N_{out}[V]}{S_{out}[V/e^-]} = \frac{V_{noise}^{RMS}}{G} \quad (6.1)$$

with G expressed in V/e<sup>-</sup>; as the gain increases, the noise reduces . **Servirebbe una misura**  
Considering the threshold dispersion a requirement for the ENC is:

$$ENC < \sqrt{(T/3.7)^2 - T_{RMS}^2(x) - T_{RMS}^2(t)} \quad (6.2)$$

where the T is the threshold setted,  $T_{RMS}$  is the threshold variation during time (t) and across the matrix (x); a typical reasonable value often chosen is 5 ENC.

Because of the changing of the 'real' threshold, the possibility of changing and adapting the setting parameters of the FE, both in time and in space is desiderable: these parameters are usually set by Digital to Analog Converter (DAC) with a number of bit in a typical range of 3-7. Unfortunately DAC elements require a lot of space that may be not enough on the pixel area; therefore, the FE parameters are typically global, which means that they are assigned for the whole chip, or they can be assigned for regions the matrix is divided into. The former case corresponds to TJ-Monopix1's design in which 7 bits are used for a total 127-DAC possible values, while the latter corresponds to the ARCADIA-MD1's one, **where quanti bit??**. An other possibility, for example implemented in TJ-Monopix2, is allocate the space on each pixel for a subset of bits, then combinig the global threshold with a fine tuning. If so, the threshold dispersion after tuning is expected to be inversely proportional to the tuning DAC number of bits and thus be improved a lot:

$$\sigma_{THR,tuned} = \frac{\sigma_{THR}}{2^{nbit}} \quad (6.3)$$

where  $\sigma_{thr}$  is the RMS of the threshold spread before tuning.

To measure the threshold and noise of pixels a possible way is to make a scan with different known injected charge: the threshold corresponds to the value where the efficiency of the signal exceeds the 50%, and the ENC is determined from the width of this edge. Following this path, I have used the injection circuit available on the chip to inject 100 pulses for each input charge for a fixed threshold. The injection comes on a capacity at the input of the FE circuit, whose mean value is 230 aF and from which the conversion factor from DAC units to electrons can be obtained: for the PMOS flavor, for example, since the DAC are biased at 1.8 V, the Least significant Bit (LSB) corresponds to a voltage of 14.7 mV from which the charge for LSB 1.43 e<sup>-</sup>/mV and the conversion factor therefore is 20.3 e<sup>-</sup>/DAC. While this value is equivalent for all the PMOS flavor, the HV flavor is expected to have a different conversion factor,  $\sim 33$  e<sup>-</sup>/DAC, beacuse of the different input capacity.

Besides the charge, also the duration and the period of the injection pulse can be set; it is important to make the duration short enough to have the falling edge during the dead time of the pixel (in particular during the FREEZE signal) in order to avoid the undershoot, coming at high input charge, triggering the readout and reading spurious hits. Since the injection circuit is coupled in AC to the FE, if the falling edge of the pulse is sharp enought to produce ad undershoot, this can be seen as a signal.

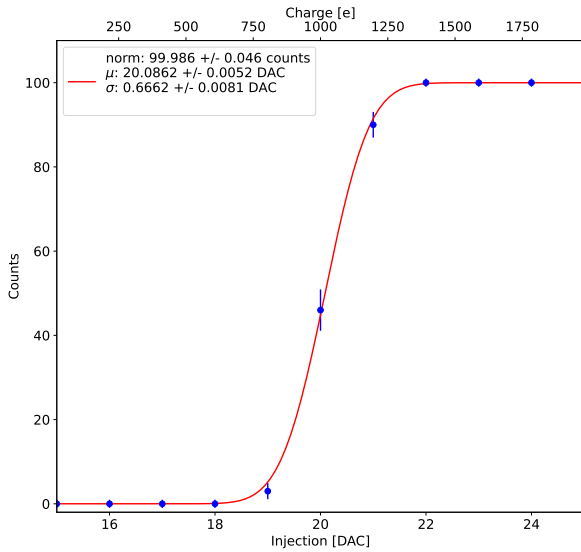


Figure 6.1: S-curve for pixel (10, 10) of the PMOS flavor (flavor 1) with IDB fixed at 40 DAC. The conversion of charge injected from DAC to electrons has been done assuming a conversion factor of 20 e-/DAC.

	PMOS A	PMOS B	PMOS C	HV
Threshold [e-]	$401.70 \pm 0.15$	$511.0 \pm 1.0$	$539.66 \pm 0.58$	$403.87 \pm 0.19$
Threshold dispersion [e-]	$32.90 \pm 0.11$	$36.96 \pm 0.66$	$55.54 \pm 0.42$	$44.67 \pm 0.15$
Noise [e-]	$13.006 \pm 0.064$	$16.444 \pm 0.086$	$13.88 \pm 0.11$	$11.68 \pm 0.10$
Noise dispersion [e-]	$1.608 \pm 0.044$	$1.95 \pm 0.06$	$1.906 \pm 0.072$	$1.580 \pm 0.068$

Table 6.1: Mean threshold and noise parameters for all flavor and their dispersion on the matrix.

Assuming a gaussian noise, the efficiency of detecting the signal can be described through a modification of the error function:

$$f(x, \mu, \sigma) = \frac{1}{2} \left( 1 + \operatorname{erf} \left( \frac{x - \mu}{\sigma \sqrt{2}} \right) \right) \quad (6.4)$$

with: where the threshold and the ENC corresponds to the  $\mu$  and  $\sigma$ . Therefore I perform a fit of the counts detected using the function in equation 6.4. In figure 6.1 there is an example with IDB equal to 40 DAC of fit for a pixel belonging to the flavor B, while in table ?? and figure ?? there are the histograms and the maps of the parameters of the scurve-fit. As expected, the flavor PMOS reset gated (A), thanks to the transistor which change the baseline value, has a lower threshold and noise

Small threshold variations has been observed in the first biasing section (columns from 0 to 14) with IDB=40 DAC; the same structure appears more evident at other different IDBs, as for example 100 DAC Plot of the average threshold per column al variare di IDB. The systematic threshold variation across the biasing group has not a known motivation, but one could certainly be the transistor mismatch of the biasing DAC registers IDB and ICASN, which both adjust the effective threshold (I recall that ICASN regulate the baseline, and in this measurements it was set to the minimin possible value).

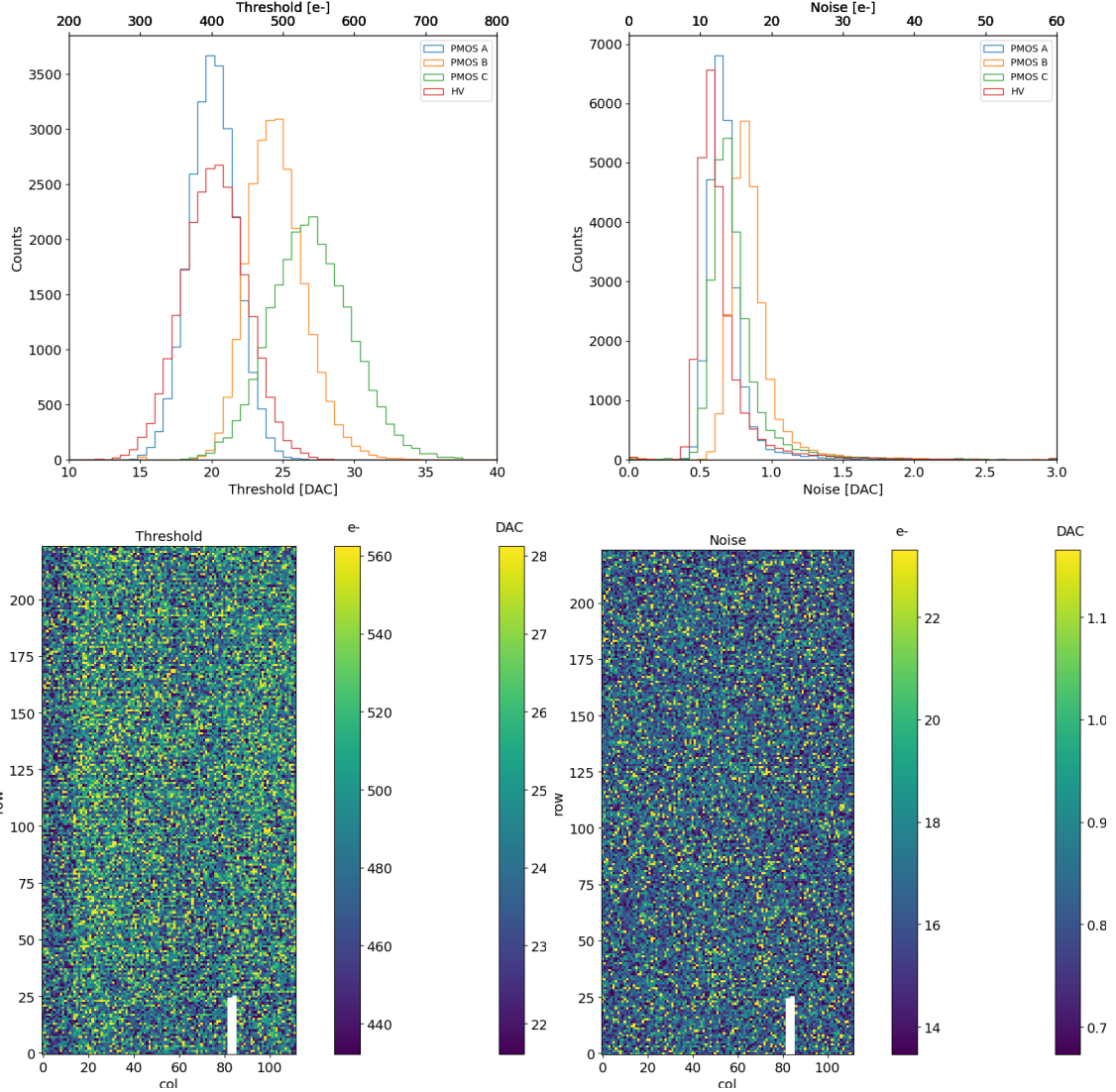


Figure 6.2: Histograms of the threshold (a) and the noise (b) found fitting the s-curve of all flavor with IDB fixed at 40 DAC. Below there are the maps of the threshold (a) and the noise (b), respectively, found fitting the s-curve with IDB fixed at 40 DAC for the PMOS flavor (B). The white pixels have the injection circuit broken.

1069 To verified the trend of the threshold as a function of the front end parameter IDB and  
 1070 find its dynamic range, I have permormed different scans changing the IDB: I have injected  
 1071 the whole matrix and found the means and the standard deviation of the distributions. The  
 1072 results are shown in figure 6.3: the blue points are the mean threhsold found whithin the  
 1073 matrix, while in green is shown the width of the threshold distribution, aka the threshold  
 1074 dispersion. While the threshold increases, the ENC decreases of  $\sim 4 \text{ e-}$ ,which is  $\sim 1/3$  of  
 1075 the noise at IDB=40 DAC.

1076 Then, to evaluet the operation and the occupancy of the chip at different threshold  
 1077 I have made long acquisitions of noise at different IDB and check how the number of  
 1078 pixel masked changes with the threshold. The masking algorithm I have used search for  
 1079 pixels with rate  $> 10 \text{ Hz}$  and mask them. With such algorithm, in our standard condition,  
 1080 IDB=40 DAC, a very low noise hit rate is intentionally achieved masking only dozen of

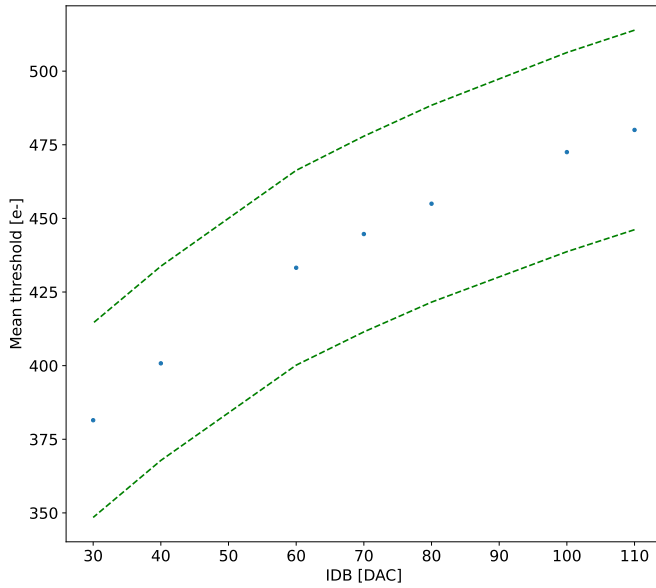


Figure 6.3: Flavor PMOS (B) with Psub-Pwell biased at -6 V. Threshold measured in electrons vs the register which sets the threshold, IDB.

1081 pixels? of the whole flavor, and other quanti are unintentionally masked.

### 1082 6.1.2 Linearity of the ToT

1083 I have already said in chapter 4 that TJ-Monopix1 returns an output signal proportional to  
1084 the charge released by a particle in the epitaxial layer, which is the Time over Threshold;  
1085 the ToT is saved as a 6-bit variable and then has a dynamic range equal to 0-64, which  
1086 corresponds to 0  $\mu$ s to 1.6  $\mu$ s assuming a clock frequency of 40 MHz. When a pulse is longer  
1087 than 1.6  $\mu$ s the counter rolls back to zero and there is no way to distinguish that charge  
1088 from a lower one with the same ToT: that is the rollover of the ToT (??(a)).

1089 In order to associate the ToT (in range 0-64) to the charge, a calibration of the signal  
1090 is necessary. Assuming the linearity between ToT and the charge, Q can be found:

$$Q [DAC] = \frac{(ToT [au] - q [au])}{m [au/DAC]} \quad (6.5)$$

1091 where m and q are the fitted parameters of the calibration. It is important to keep in mind  
1092 that the main application target of TJ-Monopix1 is in the inner tracker detector of HEP  
1093 experiments, then the main feature is the efficiency, then a rough calibration of the signal  
1094 to charge is fine. The ToT information can be used both to better reconstruct the charge  
1095 deposition in cluster in order to improve the track resolution, and for particle identification,  
1096 especially for low momentum particles which do not reach the proper detectors.

1097 The study of the output signal is made possible via the injection: since the pulses are  
1098 triangular, the ToT is expected to be almost linear depending on the injection charge value.  
1099 To verify this statement and study the deviations from linearity I've fit the ToT versus the  
1100 charge injected for all pixel within the matrix. In figure ??(b) there is an example of fit  
1101 for a pixel belonging to the flavor B, while in figure 6.5 there are the histograms and the

maps of the parameters of the line-fit for all flavors with IDB fixed at 40 DAC. Here again a difference between biasing section appears: since the slope of the ToT is related with the gain of the preamplifier (increasing the gain also increases the ToT), the mismatch is probably due to the transistor contributing to the amplification stage.

Before performing the fit I have calculated the mean value of the ToT of the pulses recorded for each pulse amplitude and I used the mean ToT as value for the fit. The aim of the calibration obviously is finding a relation only in the range 0-64 without taking into account the rolling over hits: therefore, to prevent the rollover data from reducing the mean ToT introducing a bias in the mean value, I cut and I did not consider them. If a signal bigger than the 1.6  $\mu$ s is expected in the usage of the detector, the threshold must be raised or the gain reduced, making the expected output signal in range 0-64. In figure ?? (b) are shown both the fits with a line (red) and with a second order polynomial (green): at the bounds of the ToT range values deviate from the line model. Since the deviation is low than 1% and it only interest the region near the 0 and the 64, in first approximation it is negligible.

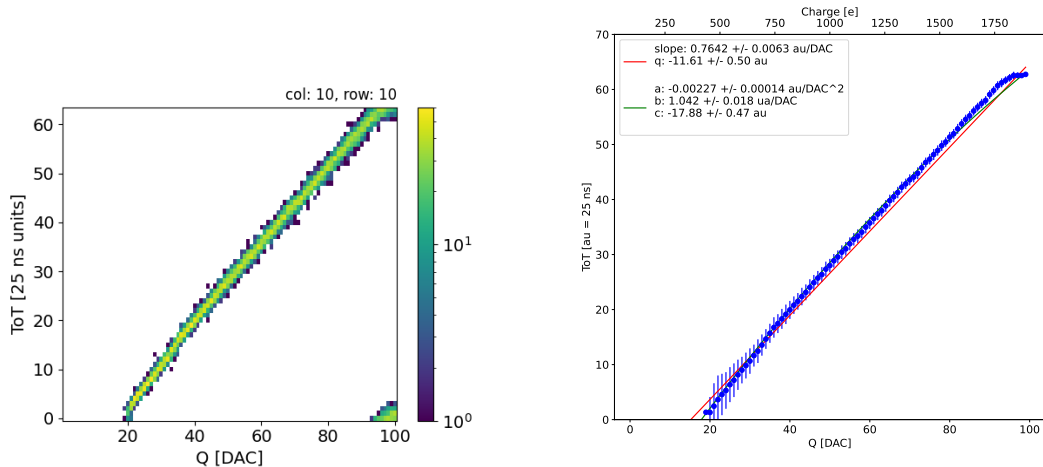


Figure 6.4: The figures refer to pixel (10,10) of the PMOS-reset flavor (1) with IDB fixed at 40 DAC for the PMOS flavor (B). (a) Histogram of the injection pulses: the ToT is in range 0-64 since it is represented by 6 bit, so when achieving the 64 it rolls over back to the zero. (b) Mean ToT vs the the charge: the mean has been calculated cutted the rolling hits.

### 6.1.3 Calibration of the ToT

Considering that the charge injected in the FE goes to fill capacitor which is different from pixel to pixel, the true charge injected does not correspond to what expected assuming C equal to 230 aF, the nominal value. Accordingly to that, a verification of the value provided and an absolute calibration of this capacity and of the conversion factor F is needed to have a correspondence of the signal in electrons; assuming C 230 aF, F is expected to be 20 e-/DAC, and is defined as:

$$F [e^- / DAC] = \frac{1616 e^-}{Q [DAC]} \quad (6.6)$$

For this purpose a Fe55 radioactive source has been employed; the Fe55 is an extremely important radionuclide in the calibration of X-ray spectrometers, proportional counter

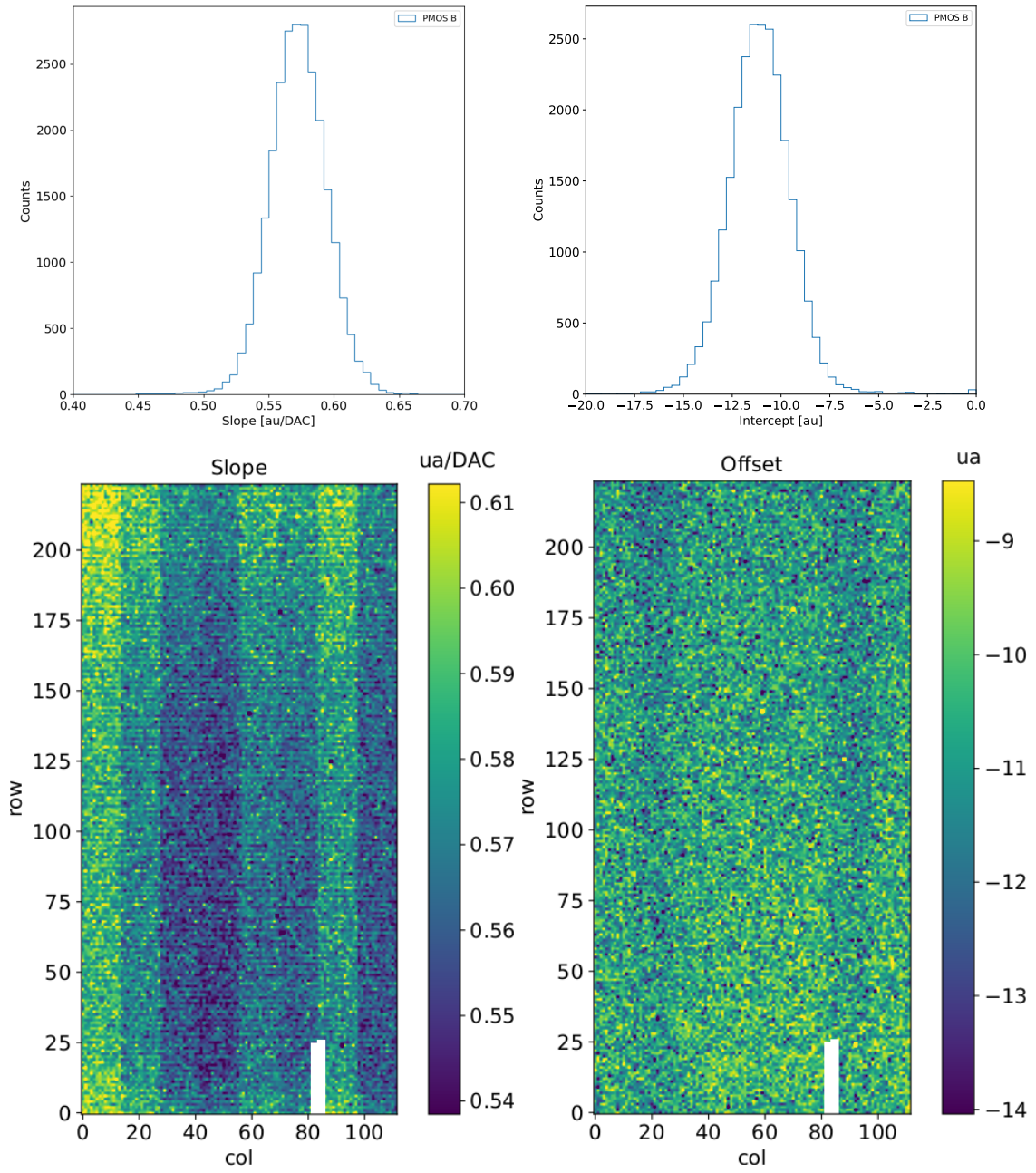


Figure 6.5: Histograms of the calibration parameters, slope (a) and offset (b), found fitting the ToT with a line, for all flavor and with IDB fixed at 40 DAC. Maps of the calibration parameters, slope (a) and offset (b), found fitting the ToT with a line, with IDB fixed at 40 DAC

and scintillator detector since it emits two X-photons during the electron capture decay: the first one ( $K_{\alpha}$ ) at 5.9 keV and the second one ( $K_{\beta}$ ) at 6.5 keV. The  $K_{\alpha}$  photon, which does photoelectric effect in the silicium, has an absorption length  $\lambda=7 \mu\text{m}$  to  $8 \mu\text{m}$ , and the probability of being absorbed in the 25  $\mu\text{m}$  thick epitaxial layer is  $\sim 0.95$ . The electron emitted has an energy equal to the photon one, so recalling that the mean energy needed to produce a couple electron-vacuum is 3.65 eV, the signal produced by the Fe55 source is expected to be  $1616 e^-$ . In figures ?? and ?? are shown two histograms of the

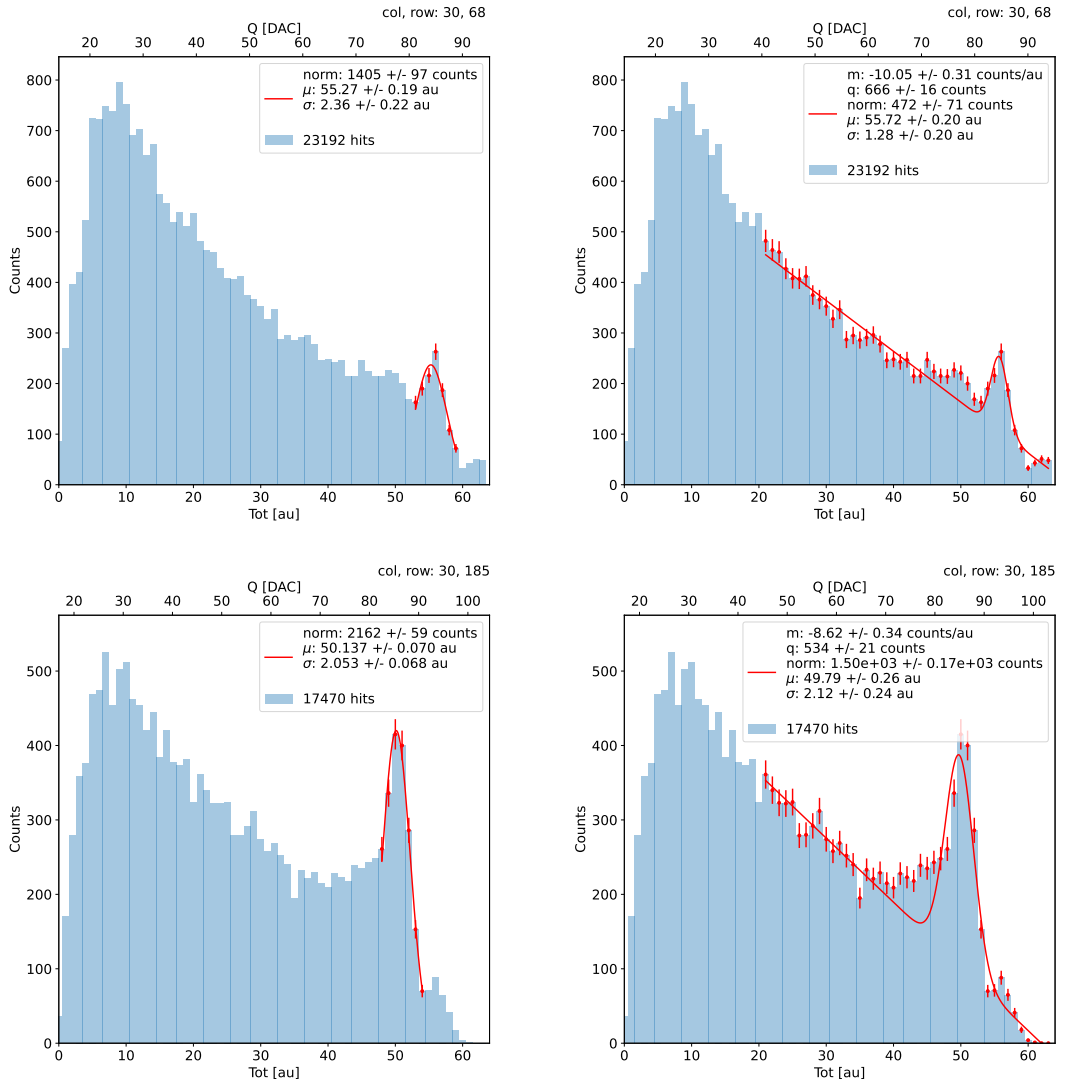


Figure 6.6: due pixel per far vedere la differenza tra i fit. Sottolinea che in rosso ci sono i bin fittati. La doppia scala utilizza le info trovate nel paragrafo precedente per il dato pixel in questione. Per avere una corrispondenza grezza in elettroni basta moltiplicare per 20 e- / dac.

1133 ToT spectrum of the Fe55 source for two different pixels. The peak corresponds to the  
 1134 events with completely absorption of the charge produced in the depleted region, while  
 1135 the long tail on the left to all the events with partial absorption due to charge sharing  
 1136 among neighbors pixels. In order to reduce the charge sharing, the pixel dimension in  
 1137 TJ-Monopix2 has been reduced down to  $30 \times 30 \mu\text{m}^2$ . The events on the right side of the  
 1138 peak, instead, corresponds to the  $K_\beta$  photons. Looking at the histograms for pixel (30,  
 1139 185) and (30,69) a significant difference in the peak to tail ratio leaps out. This difference  
 1140 in the efficiency of detecting the signal can be related with the position of the pixel in  
 1141 the matrix: in particular pixels in the upper part of the matrix (rows 112-224) have a  
 1142 more prominent peak, while in pixels in the lower part (rows 0-111) there is a higher  
 1143 partial absorption. I recall now that there is a slightly difference in the structure of the  
 1144 low dose-epi layer (??) among the rows in the matrix, in particular pixels in rows 112-224  
 1145 are supposed to have a higher efficiency in the pixel corner.

1146 For the calibration I have need to establish the peak position; to do that I perform a  
 1147 fit of the ToT histogram of each pixels. As fit functions I test both the solutions below:

$$f(x, N, \mu, \sigma) = \frac{N}{\sigma\sqrt{2\pi}} e^{-\frac{1}{2}(\frac{(x-\mu)}{\sigma})^2} \quad (6.7)$$

$$f(x, m, q, N, \mu, \sigma) = m x + q + \frac{N}{\sigma\sqrt{2\pi}} e^{-\frac{1}{2}(\frac{(x-\mu)}{\sigma})^2} \quad (6.8)$$

Nel primo caso ho fissato pochi pixel attorno a picco: il range è stato determinato ..

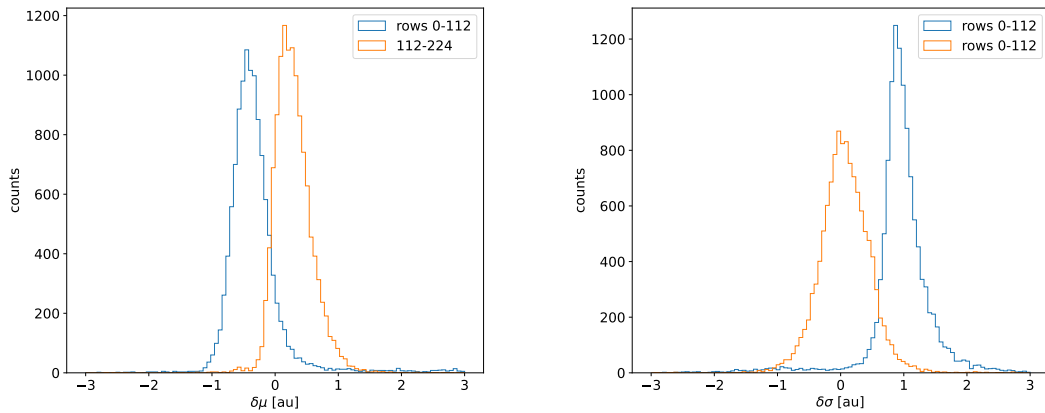


Figure 6.7: Here there are shown the defference between the parameters  $\mu$  and  $\sigma$  fitted with only a gaussian and with a gaussia plus a line. When  $\mu < 0$  the fit function 6.7 has given a worst peak (shifted on the left); when  $\sigma < 0$ , 6.8 has given a worst peak width (larger sigma)

1148  
 1149 **controlla. Nel secondo caso invece il range è.. Controlla sullo script** Even if the difference  
 1150 in the peak position between the two cases is not really relevant (6.7) being of the order  
 1151 of 0.8-1.5 %, it still introduces a systematic effect moving the peak on the left because of  
 1152 the contribution of the tail. Indeed, we know that the sharp edge on the right corresponds  
 1153 to the complete absorption of the photon, so excluding the little bump on the right, the  
 1154 more the fitted parameter is on the right, the better the fit is. Moreover, there is also  
 1155 systematic effect on the peak width, infact the worst fit also gives an overestimation of  
 1156 the peak width. Even looking at the  $\chi^2$ , the fit function 6.7 seems so be the better choise,  
 1157 except for a sample of pixels on the lower part of the matrix, the one with lower efficiency.

1158 Mappa del ferro da cui, come descritto nell'equazione si ricava la capacity. La struttura  
 1159 a bande della capacità ha origine nel plot... e quindi nella calibrazione. Andando a vedere  
 1160 gli istogrammi di queste due variabili si vedono dei picchi. C'è qualche struttura nella  
 1161 matrice che condiziona il funzionamento delle righe? Larghezza della gaussiana: fai il  
 1162 discorso a cosa contribuisce ad un picco così largo. è compatibile con quanto ti aspetti?  
 1163 The voltage fluctuation around the peak is caused by the number fluctuation of generated  
 1164 carriers (Fano noise) and the noise introduced by the detector (sensor and front-end pre-  
 1165 amplifier). The ENC can be estimated from the standard deviation of the Kalpha voltage  
 1166 distribution.  $ENC = \text{sqrt}(\sigma_{\text{misurata}} - \sigma_{\text{aspetti}})$  quella che ti aspetti dal fattore di Fano). E  
 1167 è compatibile con quanto trovato? se non fosse compatibile rimaneggia questa frase: tra noise  
 1168 is added from the system (test setup) at the analog monitoring pixel output.

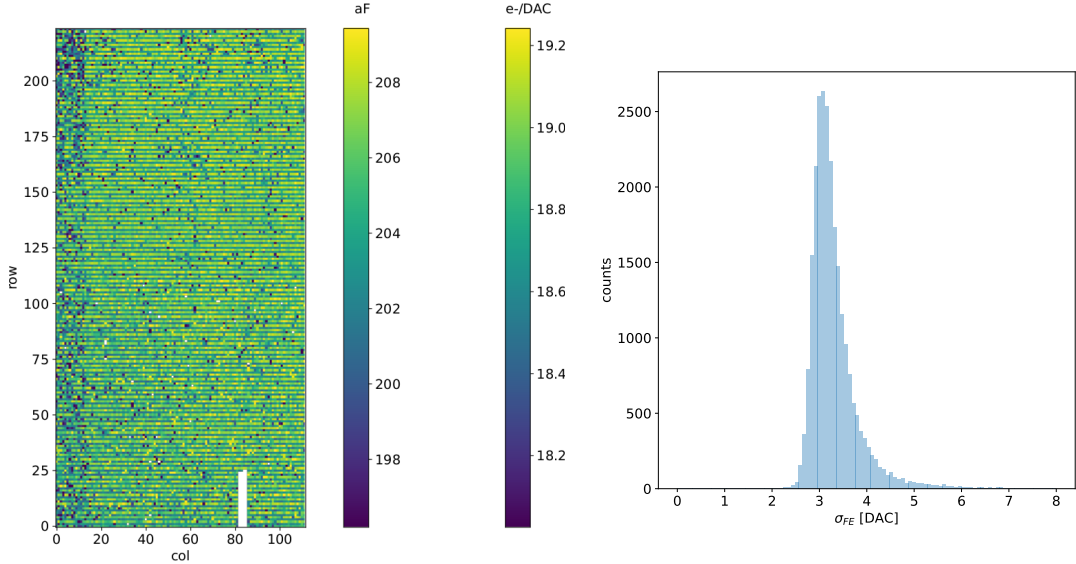


Figure 6.8

#### 1169 6.1.4 Changing the bias

1170 In order to study the behavior of the sensor changing the bias, I perform some injection  
 1171 scans in different configurations. The thickness of the depletion has to be considered  
 1172 indeed an important parameters for the efficiency of the signal, and in particular it affects  
 1173 the charge released by a particle which cross the sensor (since the signal is proportional to  
 1174 the thickness of the epitaxial layer). Given that the chip under examination has a gap in  
 1175 the low dose epi-layer (look at chapter 4.1) we were not able to change independently the  
 1176 bias of the substrate (PSUB) and of the p-well (PWELL), but they must be kept at the  
 1177 same value, differently from other chips, where on which some test has been performed, as  
 1178 reported in figure 6.9. A 2D map of the measured output voltage amplitude and resulting  
 gain in the case of the PMOS and HV are reported.

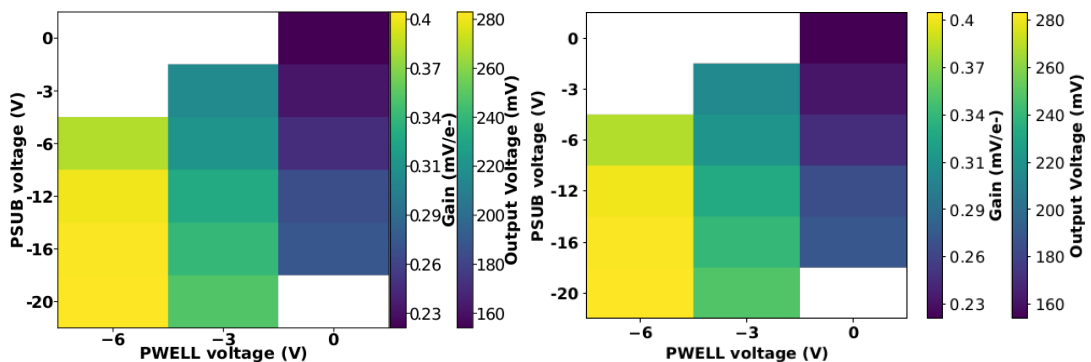


Figure 6.9: 2D map of the output voltage amplitude and gain with respect to the p-well and p-substrate in the case of the PMOS reset front-end (B)

1179  
 1180 In order to test the behavior of the chip when not completely depleted, I have performed  
 1181 an injection scan with PSUB/PWELL bias at 0 V, -3 V and -6 V, and some acquisitions  
 1182 with the Fe55 source. The results of the measurements are reported in table 6.2 and in  
 1183 figure ???. Turning down the bias, the depletion region narrows and the efficiency reduces,  
 1184 in particular in the pixel corner; in particular the threshold increases of  $\sim 1/4$ , the noise

	-6 V	-3 V	0 V
Threshold [DAC]	$20.04 \pm 1.6$	$21.0 \pm 1.6$	$24.5 \pm 1.8$
Noise [DAC]	$0.613 \pm 0.075$	$0.625 \pm 0.078$	$0.822 \pm 0.098$
Slope [au/DAC]	$0.726 \pm 0.027$	$0.707 \pm 0.028$	$0.573 \pm 0.021$
Offset [au]	$-10.8 \pm 1.9$	$-11.2 \pm 1.8$	$-11.1 \pm 1.5$

Table 6.2: The errors are the standard deviations of the corresponding distributions. The conversion factor from DAC to electrons is  $\sim 20 \text{ e}^-/\text{DAC}$ .

of  $\sim 1/3$  and the slope, which parameterizes the linearity of the analog output and strictly depends on the gain, decreases of  $\sim 1/4$ . In figure 6.10(b) are reported the values of the  $K_\alpha$  peak position, the normalization of the events above the peak and the rate, everything has been normalized to the value at the reference condition, which is with PSUB/PWELL at -6 V. In order to evaluate the peak position and the normalization I have fit the spectrum in the region on the right with a gaussian. Looking at the spectrum, an other characteristics seems to appear: at lower bias the peak width is bigger than in a full depletion mode. This could be due at a bigger capacity, which influence the noise.

### 6.1.5 Measurements with radioactive sources

In order to completely validate the operation of the whole sensor<sup>1</sup>, I have made some acquisitions with radioactive source, in particular I have used Fe55, Sr90, which is a  $\beta^-$  emettitor with electron endpoint at 0.546 MeV, and cosmic rays, which are supposed to be mostly MIP. In the acquisitions with Sr90 and cosmic rays, I specifically focused on the events whith charge sharing and with more hits than one per events, that are clusters.

The definition of cluster I chose is built only on the time of arrival of hit, in particular I established that all particles with the same timestamp belong to the same cluster. This obviously is a coarse requirement but it gave me the opportunity of using a simple and fast clustering algorithm, which is fine when the random coincidence probability is negligible. Defining  $R_1$  and  $R_2$  as the two events rate, and  $\tau$  as the dead time of the detector, the random coincidence rate can be found:

$$R_{coinc} = R_1 \times R_2 \times \tau \quad (6.9)$$

As I am going to prove in the next section, the dead time strictly depends on the occupancy of the matrix, even through we can assume a dead time of  $\sim 1 \mu\text{m}$ , which corresponds to the mean dead time per pixel. However, if in an event a particle hit two different pixels producing a cluster, the total dead time simply doubles. Then, assuming a rate of noise of  $\sim \text{Hz}$  on the whole matrix and being the mean rate of the , the random coincidence of two hits coming from Fe-noise, Sr-noise, CR-noise and noise-noise are respectively

In figure ?? I report the histograms of the number of pixels in the cluster and of the dimension of clusters, defined in terms of the max and min coordinates on the matrix as:

$$d = \sqrt{(y_{max} - y_{min})^2 + (x_{max} - x_{min})^2} \quad (6.10)$$

---

<sup>1</sup>As I will explained in chapter ?? these measurements are foundamental also to be compared with the spectrum seen at the testbeam

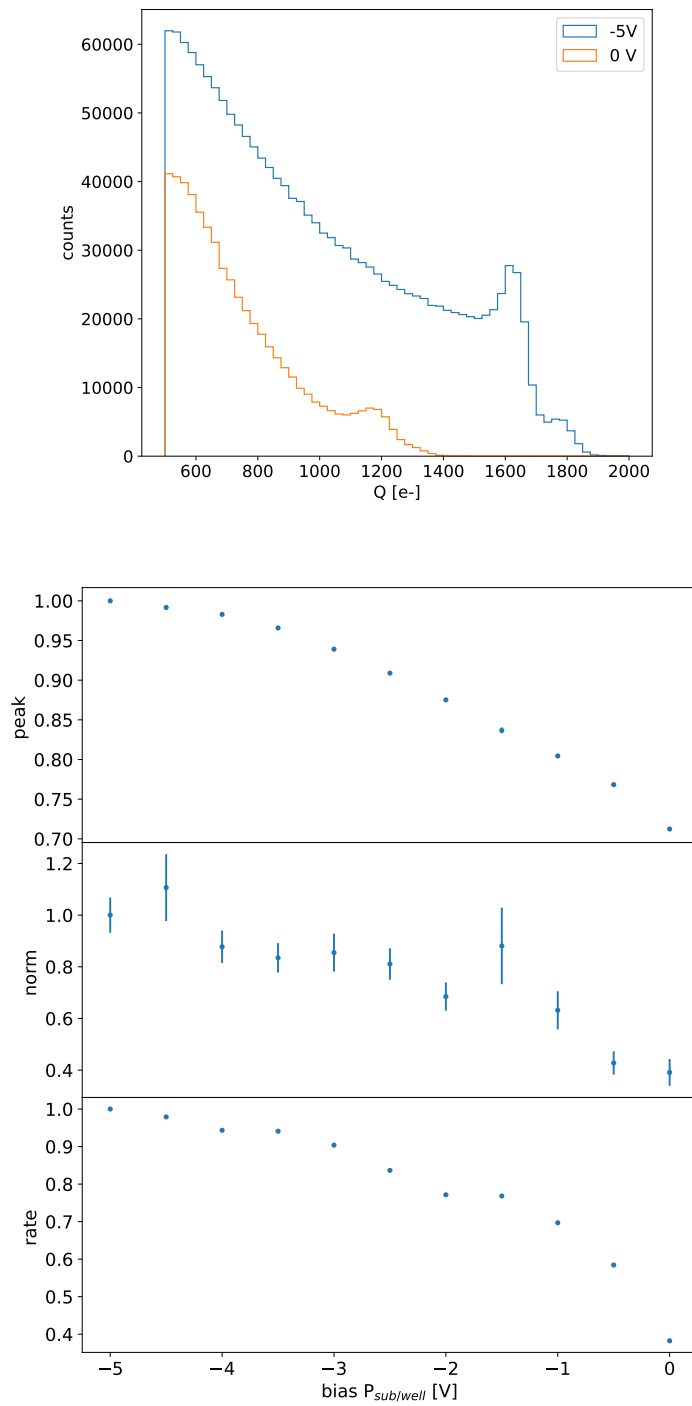


Figure 6.10: Two acquisition with the Fe55 source at different bias.

1213 quello che si nota è che lo Sr fa cluster più grandi mediamente, che arrivano anche a 22  
 1214 hit.

1215 Below I have also attached a sample of hitmap of events produced by the three different  
 1216 sources.

1217 • PLOT delle hit per cluster

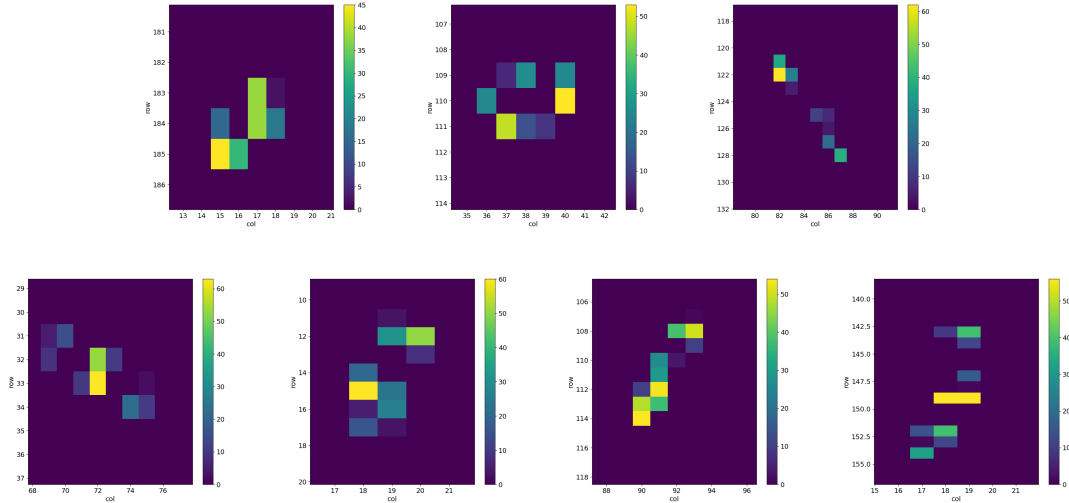


Figure 6.11

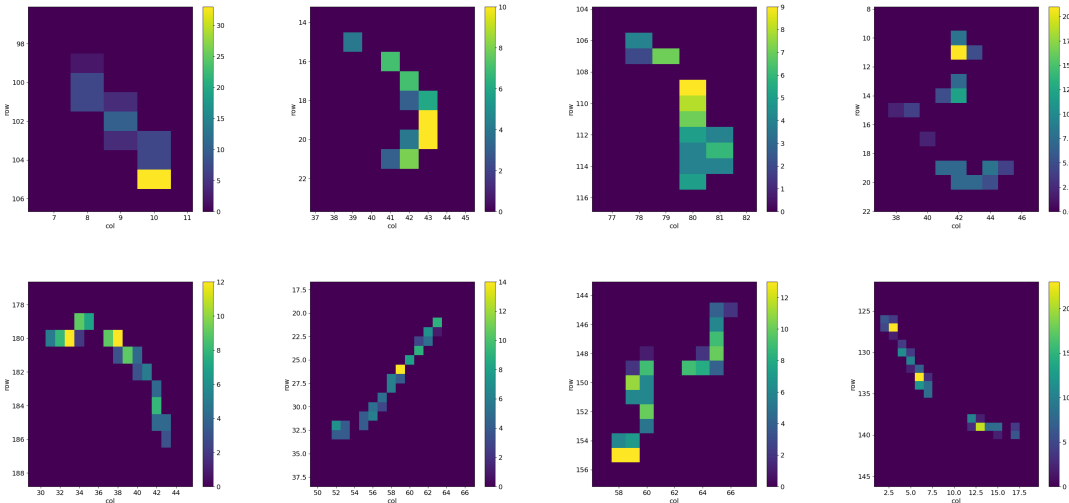


Figure 6.12

- 1218 • esempio di heatmap di cluster
- 1219 • sostituisci in carica in un file del ferro, guarda somma dei cluster, stessa cosa per Sr  
1220 e MIP
- 1221 • Spiega che con il flavor HV abbiamo una perdita di segnale, fai vedere uno spettro  
1222 di delle misure dell'8 marzo.
- 1223 The signal generated by electrons is similar to the one generated by minimum ionizing  
1224 particle (MIPS) **dovrei mettere qualche conto per giustificare questa affermazione**, and the  
1225 spectrum is expected to follow a Langau-Gauss distribution. **nelle acquisizioni dei CR ho**  
1226 **selezionato solo i cluster, per tagliare via il rumore.**
- 1227 , looking at the cluster dimension and the cluster charge.

1228    **6.1.6 Dead time measurements**

1229    The hit loss is due to analog and digital pile up: the first one occurs when a new hit  
1230    arrives during the pre-amplifier response, the second instead when the hit arrives while  
1231    the information of the previous hit has not yet been transferred to the periphery. Since  
1232    the pre-amplifier response has a characteristic time  $\sim$ ToT, the dead time  $\tau_a$  introduced  
1233    by it will be at most 1.6  $\mu$ s; using the IRESET and VRESET FE parameters the reset  
1234    time can be lowered down, but a **IRESET**, puoi diminuire il tempo di scarica ma deve  
1235    comunque Regarding the latter contribution instead, since only one hit at a time can  
1236    be stored on the pixel's RAM, until the data have completed the path to get out, the  
1237    pixel is paralyzed. Moreover since there is no storage memory included on TJ-Monopix1  
1238    prototypes, the digital dead time  $\tau_d$  almost corresponds to the time needed to transmit the  
1239    data-packets off-chip.

1240    The exportation of data from pixel to the EoC occurs via a 21-bits data bus, therefore  
1241    only one clock cycle is needed and the dead time bottleneck is rather given by the  
1242    bandwidth of the serializer which transmits data off-chip from the EoC. In our setup the  
1243    serializer operates at 40 MHz, thus to transmit a data packet (27-bit considering the ad-  
1244    dition of 6 bits to identify the double-column at the EoC) at least 675 ns are needed. For  
1245    what we have said so far, the R/O is completely sequential and therefore is expected a  
1246    linear dependence of the reading time on the number of pixels to read:

$$\tau = 25 \text{ ns} \times (\alpha N + \beta) \quad (6.11)$$

1247    where  $\alpha$  and  $\beta$  are parameters dependent on the readout chain setting.

1248    To test the linearity of the reading time with the number of pixels firing and to measure  
1249    it, I have used the injection circuit which allows me choosing a specific hit rate: I made  
1250    a scan injecting a fix number of pulses and each time changing the number of pixels  
1251    injected. Indeed the injection mode allows fixing not only the amplitude of the pulse,  
1252    which corresponds to the charge in DAC units, but also the time between two consecutive  
1253    pulses (DELAY). The hit rate then corresponds to 25 ns/DELAY.

1254    Unfortunately a high random hit rate on the matrix cannot be simulated by the in-  
1255    jection because of the long time ( $\sim$ ms) needed to set the pixel registers of the injection;  
1256    then I was forced to specify at the start of the acquisition the pixels to inject on, and for  
1257    convenience I chose those on a same column. In figure 6.13 is shown the dependence of  
1258    the efficiency on the DELAY parameter in two different cases. For the 5 pixels example  
1259    the efficiency goes down the 90% at a DELAY of  $\sim$ 185 clock counts, which corresponds  
1260    to 4.625  $\mu$ s and to a rate of 216 kHz, while in the 10 pixels example, the efficiency goes  
1261    under the 100% at  $\sim$ 380 clock counts, which corresponds to 9.5  $\mu$ s and to a rate of 105 kHz.  
1262    **COME MAI SONO DIVERSE LE CURVE?** From the efficiency curves I have then looked  
1263    for the time when the efficiency decreases. In figure 6.14(a) is shown the dead time per  
1264    pixels as a function of N with different R/O parameters configuration, the meaning of  
1265    which is explained in chapter 4.3. The default value suggested by the designer of the chip  
1266    are reported in table 6.3; moving too much the readout parameters from the default ones,  
1267    the readout does not work properly, and no hits can be read at all. The problem probably  
1268    stays in the firmware setting of the readout which are specially fixed for our chip **Sul**  
1269    **repositorio, nei commenti ci sono altri valori possibili per il FREEZE, ma avevamo detto**  
1270    **che probabilmente sono relativi ai setting di altri chip.** Despite the single pixel reading  
1271    time does not depend on the position on the pixel matrix, within a clock count which

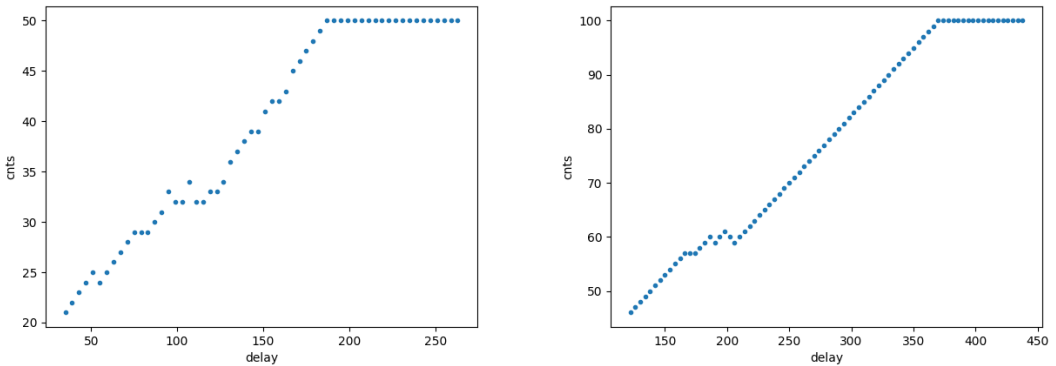


Figure 6.13: Efficiency vs the DELAY parameters. (a) I made a scan injecting 5 pixels with 50 pulses for each DELAY configuration and (b) 10 pixels with 100 pulses for each DELAY

Parameter	Value [DAC]	Value [ $\mu$ s]
START_FREEZE	64	1.6
STOP_FREEZE	100	2.5
START_READ	66	1.65
STOP_READ	68	1.7

Table 6.3: Default configuration of the R/O parameters

is  $\sim 25$  ns, and it is equal to 106 clock counts, since the  $\tau_d$  critically depends on the pixel position on the matrix: in particular the reading sequence goes from row 224 to row 0, and from column 0 to column 112, making the pixel on the bottom right corner the one with the longest dead time.

Furthermore to test that there is no dependence of the digital readout time from the charge of the pulse, I have tried to change the amplitude of the pulse injected, but the parameters found were consistent with the default configuration ones. No difference in the  $\alpha$  and  $\beta$  coefficients has been observed between the two cases. Referring to eq.6.11, the factor  $\alpha$  is proportional to the difference (STOP\_FREEZE - START\_READ), while the offset  $\beta$  lies between 5 and 15 clock counts.

Per avere una misura veritiera del tempo morto e del hit loss si dovrebbe iniettare casualmente input events are produced by a random hit generator with a specified hit rate, hence following a Poisson distribution. Inoltre faccio notare che il tempo morto è così lungo perché c'è parallelizzazione e neppure un buffer (cosa tipicamente prevista quando li si inserisce nei rivaltori). Ad esempio Obelix, per l'upgrade di Belle2 avrà un buffer a fine matrice.

## 6.2 ARCADIA-MD1 characterization

Unfortunatly we have found out that the chip we received was not completely functional, then we have been able to make on it only a few electrical and software test. We have then verified the communication of the chip with the DAQ, testing the operations of the FPGA and the breakout board (BB). The problem occurs when the chip is biased, in

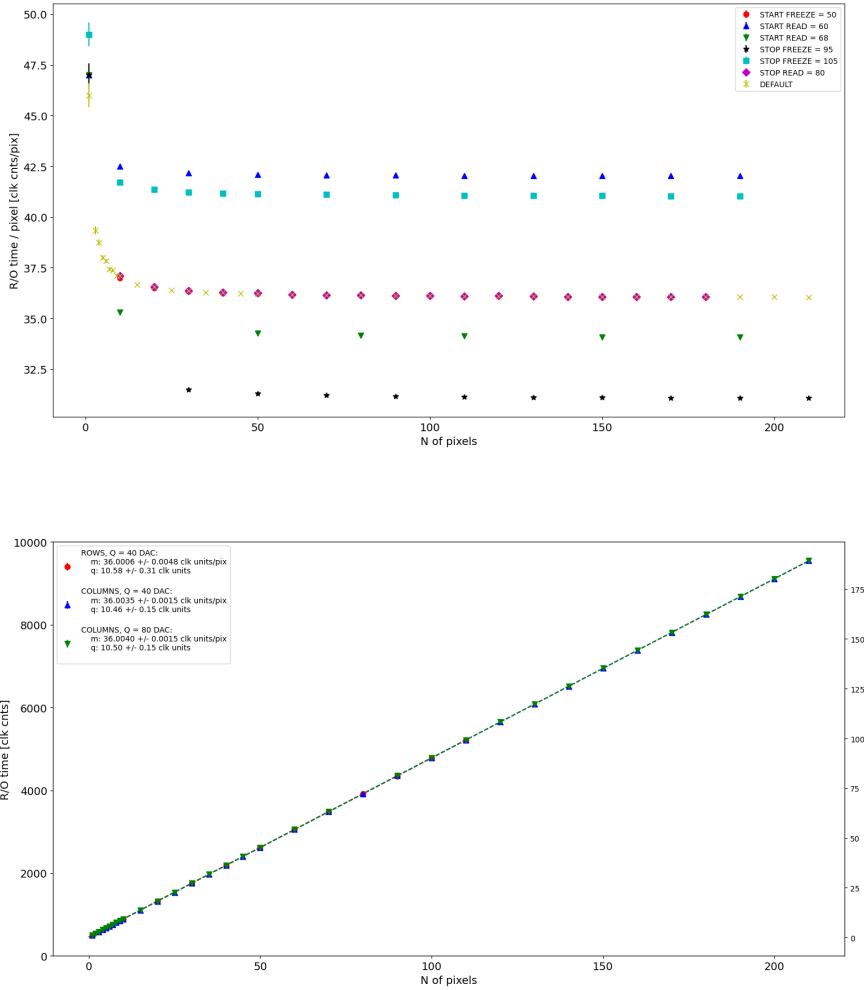


Figure 6.14: (a) Readout time per pixel as a function of the number of pixel injected obtained with different FE setup. (b) Readout time as a function of the number of pixels injected obtained injecting pulses with amplitude of 80 DAC (green), of 40 DAC on the same row (red) and on the same column (blue).

particular, when the HV voltage is lowered down 0 V, the sensor requires too much power and a too high current draw sets. We have discussed the problem with the designers of the chip whose helped us indentifying the motivation of the break: the chip has been glued using too much conductive tape and hence have a short-circuit between the sides and the back, which makes impossible the biasing. Unfortunately, since both the sensor and the FE require at least -10 V to work properly, no measurement was possible except the acquisition of the noise in the FE circuit.

We received then another chip, a minid2, that is a "mini demonstrator" from the second submission. The two chips have the same charateristics but the minid2 is smaller than the MD1, in particular it only have  $32 \times 512$  pixels, instead of  $512 \times 512$ . **scrivi il problema della prima sottomissione.**

An exhaustive characterization and testing of the new chip have been going on in the clean room on the INFN, and I am going to show here only some preliminary results. Up to now we used the injection circuit in order to make a threshold scan on a few pixels:

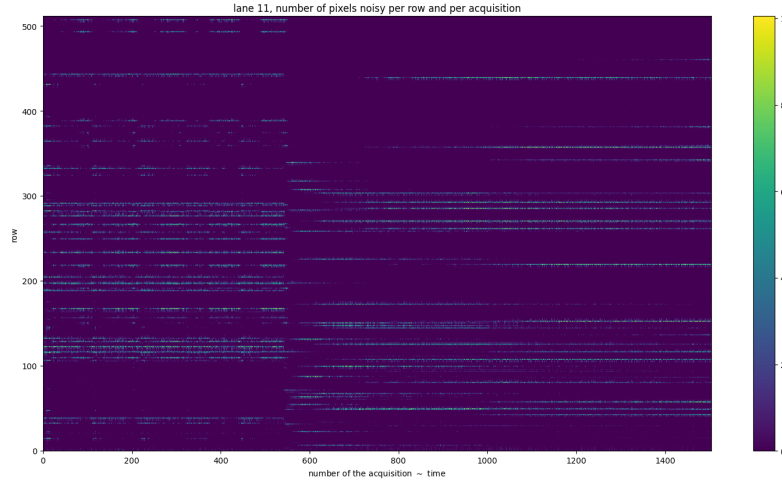


Figure 6.15: Noise in the front end circuit depending on the bias road across the matrix was recorded.

1307 differently from the TJ-Monopix1's characterization where we performed a scan changing  
 1308 the injection charge of the pulse, with the minid2 we have instead changed the threshold  
 1309 (whose register is VCASN) keeping the charge of the pulse fixed. For each threshold we  
 1310 inject 100 pulses of amplitude 10  $\mu$ s. The dependence of the efficiency on the threshold for  
 two pixels is shown in figure 6.16.

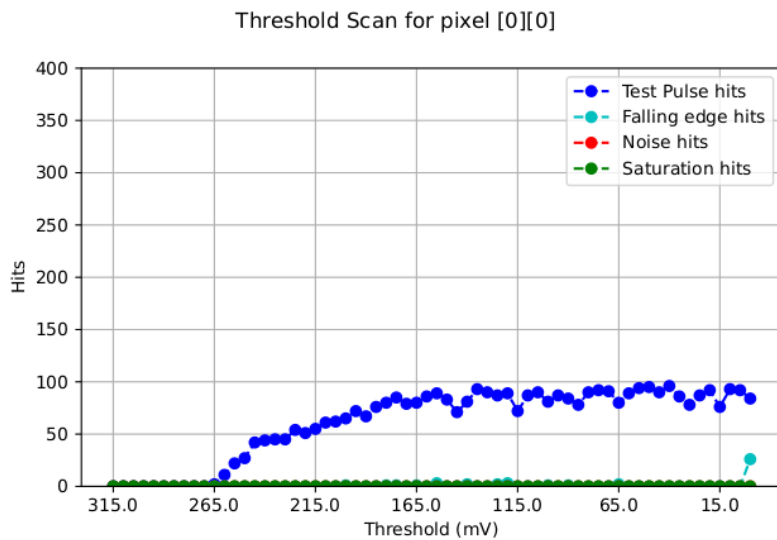


Figure 6.16

1311  
 1312 Anche se il comportamento è globalmente ragionevole, con l'efficienza che sale quando  
 1313 si abbassa la soglia, viene il sospetto che non stiamo polarizzando bene il sensore e il  
 1314 FE dato che anche raggiunto i centi conteggi, si hanno delle fluttuazioni intorno a questo  
 1315 valore. Inoltre notiamo che abbassando ulteriormente la soglia si osserva un aumento delle  
 1316 hit, dovuto al fatto che si inizia a triggerare sul rumore.

1317 commenta sul fatto che non è stabile anche molto sopra la soglia. Forse è dovuto al  
 1318 bias? oppure l'impulso ha qualche problema (non abbiamo settato la durata ecc..)? Che

1319 valore ha in elettroni?

1320 Substantial differences have been observed in both the efficiency and the threshold  
1321 among the sections, with VCASN=40 DAC; this suggests that with this particular FE  
1322 configuration there is a big threshold dispersion on the matrix. The hitmap of an ac-  
1323 quisition with the Fe55 source is shown in figure 6.17: the whole MD1 matrix with only  
1324 the bottom region (32 rows) working is represented in (a), while in (b) there is a zoomed  
1325 bitmap. The rate seen within the region 8 (green region in the figure (a)) is compatible  
1326 with the rate of the same radioactive source measured with TJ-Monopix1, that it  $\sim$ 3.3 kHz.  
Looking to the Sr90 acquisitions (fig.6.18) many clusters and tracks can be immidiately

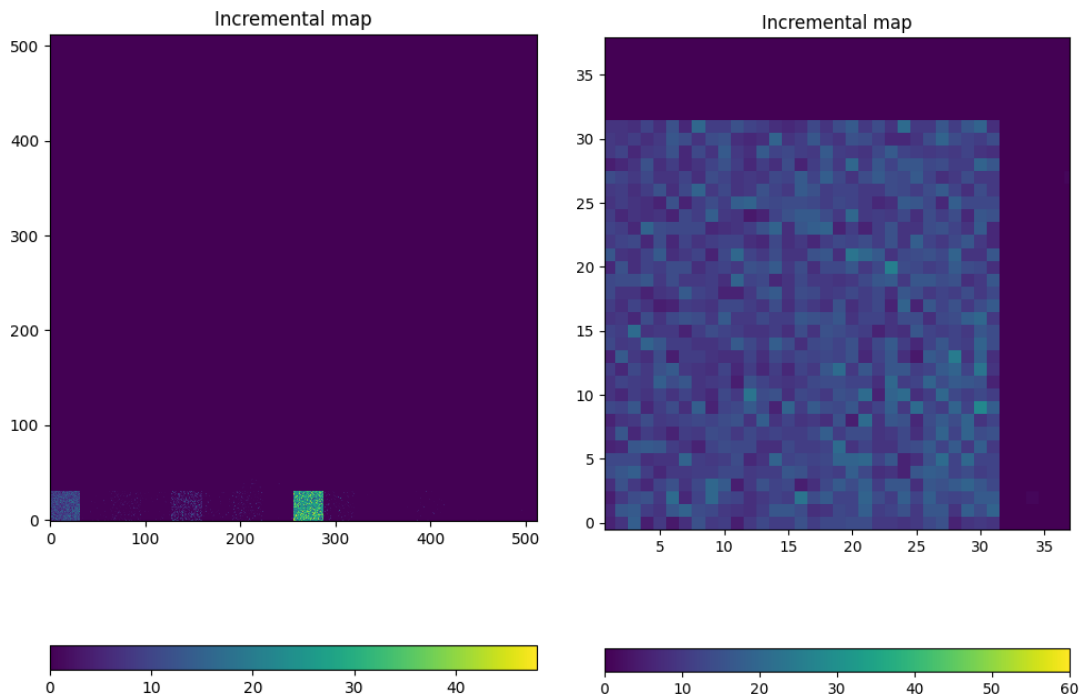


Figure 6.17: Fe55 acquisition with VCASN=40 DAC. (a) All the matrix  $512 \times 512$  is plotted even if the minid2 has only the rows in range 0-32. (b) A zoom on the first section (col 0-32).

1327

1328 distinguished, confirming what observed with TJ-Monopix1.

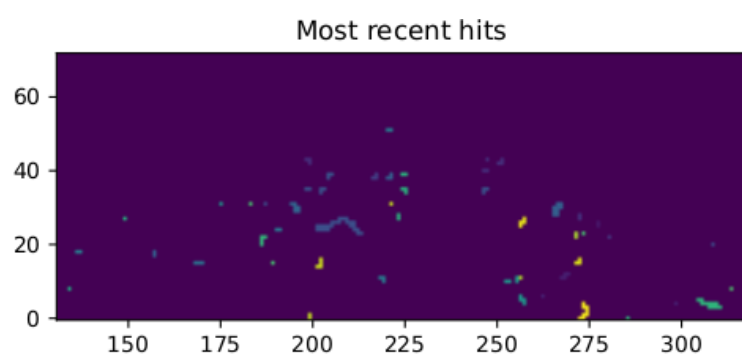


Figure 6.18: Sr90 acquisition with VCASN=40 DAC. The different colours are related with the time of arrival of the hits: in yellow the most recent hits, while in blue the old ones.

<sub>1329</sub> **Chapter 7**

<sub>1330</sub> **Test beam measurements**

<sub>1331</sub> At PRF smaller than 100 Hz, all the dosimeters analyzed have a shorter signal collection  
<sub>1332</sub> time with respect to the repetition time of the pulses (maggiore uguale 10 ms), and,  
<sub>1333</sub> consequently, the saturation is influenced only by the dose-per-pulse (duration of the  
<sub>1334</sub> pulse is around 2.5 us)

<sub>1335</sub> During August 2022 a testbeam took place in Santa Chiara hospital in Pisa, where a  
<sub>1336</sub> new accelerator designed for both medical research and R&D in FLASH-RT, and for this  
<sub>1337</sub> reason called "ElectronFlash", have been installed a few months ago.

<sub>1338</sub> The motivation of the testbeam measurements were testing TJ-Mopopix1 in condition  
<sub>1339</sub> different from the one foreseen during the design and also testing the mechanical and the  
<sub>1340</sub> DAQ setup for other future measurement. TJ-Monopix1 is supposed to be employed for  
<sub>1341</sub> tracking in HEP experiments while our goal was testing the possibility of integrating the  
<sub>1342</sub> charge released by more particles at ultra high hit rate achievable with the accelerator.  
<sub>1343</sub> **Una frase di disclaimer sul fatto che non siamo riusciti a testare quello che volevamo.**

<sub>1344</sub> In medical physics the dose is indeed the standard parameter to characterize the beam  
<sub>1345</sub> because of its obvious relation with the damage caused in the patient: firstly the oncolo-  
<sub>1346</sub> gists prescribe a certain dose taking into account the efficacy of the treatment and then  
<sub>1347</sub> the medical physicists, on the basis of simulations, decide the energy and the intensity of  
<sub>1348</sub> the beams to dispense the prescribed dose amount. By the point of view of the instrumen-  
<sub>1349</sub> tation and the testing on it, a more common and useful parameter is instead the rate or  
<sub>1350</sub> the fluence of particles. The conversion between the two quantity can be found thinking to  
<sub>1351</sub> the definition of dose: it is the concentration of energy deposited in tissue as a result of an  
<sub>1352</sub> exposure to ionizing radiation. Assuming total absorption of electrons in water, defined  
<sub>1353</sub> by law as the ordinary reference medium, the dose can be expressed as:

$$D[Gy] = \frac{NE[eV]}{\rho[g/cm^3]A[cm^2]x[cm]} \quad (7.1)$$

<sub>1354</sub> After having applied the conversion of the energy from eV to J and noticed that  $E/\rho x$   
<sub>1355</sub> roughly corresponds to the stopping power S of electrons in water, a simple estimation of  
<sub>1356</sub> the dose released in water is:

$$D[Gy] = 1.602 \cdot 10^{-10} N[cm^{-2}] S[MeV cm^2/g] \quad (7.2)$$

<sub>1357</sub> **7.1 Apparatus description**

<sub>1358</sub> The accelerator is placed in a bunker inside the hospital: to shield the outdoor from  
<sub>1359</sub> ionizing radiation the bunker has very thick walls of cementum and both the control units

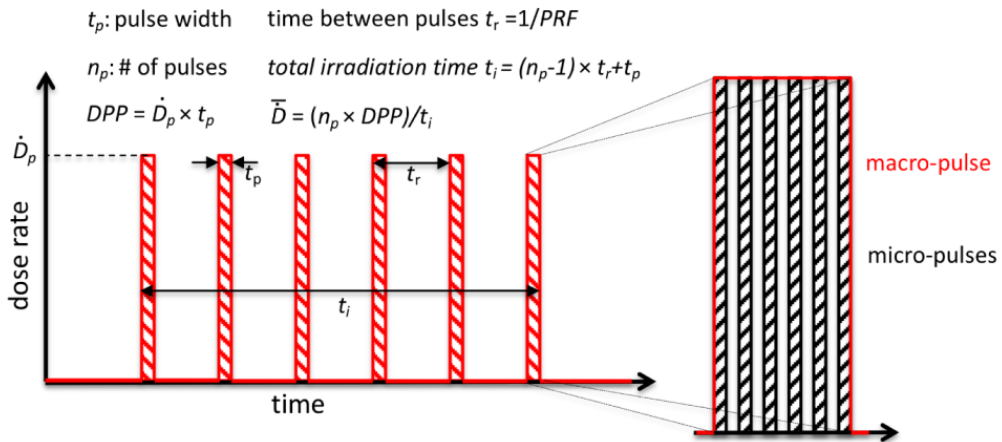


Figure 7.1: Typical beam structure of a beam with the standard characteristic quantity

$\bar{D}$	Dose rate (mean dose rate for a multi-pulse delivery)	0.005-10000 Gy/s
$\dot{D}$	Intra pulse dose rate (dose rate in a single pulse)	0.01-1 $10^6$ Gy/s
DDP	Dose in a single pulse	0.04-40 Gy
PRF	Pulse repetition frequency (number of pulses delivered per unit of time)	1-350 Hz
$t_p$	Pulse width	0.2-4 $\mu$ s
n	Number of pulses	single/pulse train

Table 7.1: The parameters that can actually be set by the control unit are the PRF, DDP,  $t_p$  and n (in particular singular irradiation or pulse train), while the other changes consequently.

1360 of the accelerator and of the detector were placed outside the bunker. For practicability  
 1361 reasons the power supply were the only device to be placed inside the bunker.

### 1362 7.1.1 Accelerator

1363 The ElectronFlash accelerator is an electron Linear Accelerator (LINAC) with two energy  
 1364 configurations, at 7 MeV and 9 MeV, and it can reach ultra high intensity (40 Gy/pulse)  
 1365 keeping the possibility of accessing many different beam parameters and changing them  
 1366 independently from each other. This characteristic is fundamental for research in FLASH-  
 1367 RT, both for the medical aspects and for the studies on detectors; for example is not really  
 1368 clear the dependence of the efficacy of the FLASH effect on the whole dose parameters.  
 1369 ElectronFlash is **almost the only one** in the world having this characteristic, **ricontrolla sulla**  
 1370 **review, c'era qualcosa che puoi dire.** The accelerator implements a standard beam struc-  
 1371 ture for RT with electrons (fig. 7.1), that is a macro pulse divided in many micropulses;  
 1372 the parameters used to set the dose and their range of values settable by the control unit  
 1373 is reported in table 7.1.

1374 The accelerator is provided of a set of triod cannons  $\sim$ 1.2 m long and with diameters  
 1375 from 1 cm to 12 cm and a collimator that can be used as beam shaper to produce a  
 1376 squircle shape. The triode, which is made by plexiglass, must be fix to the gun during the  
 1377 irradiation and is needed for producing an uniform dose profile (fig.7.2) which is desired  
 1378 for medical purpose via the scattering of electrons with the plexiglass.

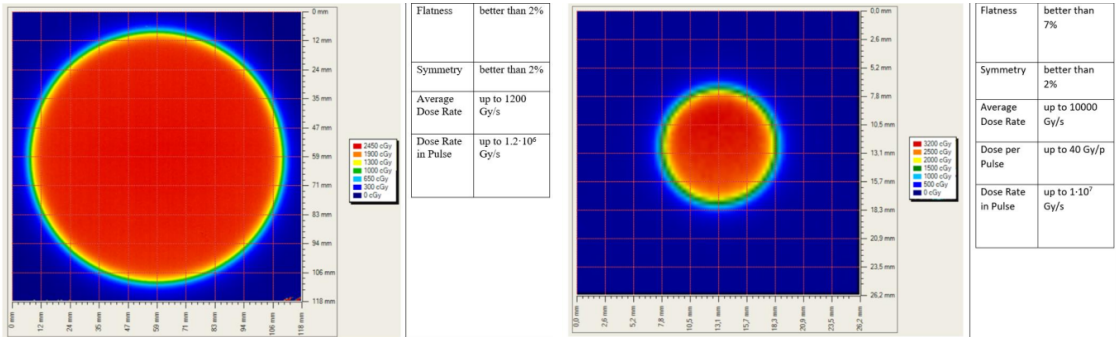


Figure 7.2: Two example of x-y isodose curves for two different triodes, 10 cm and 1 cm respectively, reported by the producer in the manual with the specific of the accelerator (S.I.T. - Sordina IORT Technologies S.p.A.). With the smaller collimator the dose rate in pulse is comparatively higher.

### 1379 7.1.2 Mechanical carriers

1380 The tested detector consists in one chip, the Device Under Test (DUT), mounted on a  
 1381 board and connected to FPGA with same arrangement of figure 7.7. These have been  
 1382 positioned vertically in front of the triode on a table specifically built for the testbeam.  
 1383 The tree board have been enclosed in a box of alluminium with a window on the DUT  
 1384 and with the required holes at the side to enable the biasing via cables and the connection  
 1385 with the DAQ provided via ethernet cable. A trigger signal coming from the control unity  
 1386 and syncronize with the pulses emitted from the beam has been also sent to the FPGA.  
 1387 This signal cannot be considered a trigger signal, since being a prototypes TJ-Monopix1  
 1388 has been designed to be triggerless, but the time of arrival of this signal, which is saved  
 1389 by the FPGA, can allow the reconstruction of the of the arrival of the bunch during the  
 1390 analysis.

1391 In order to shield the sensor from the whole particles emitted from the gun, two  
 1392 alluminium collimators have been fabricated: one has been positioned at the triode exit  
 1393 while the other in front of the DUT. The collimators are  $t=32$  mm thick and have a  
 1394 diameter  $d$  equal to 1 mm: assuming a beam divergence bigger than  $d/t=1/32 = 1.8^\circ$ ,  
 1395 which is the case, the collimator at the triode output was supposed to work as a point  
 1396 source and to reduce the rate on the DUT of a factor at least  $4 \cdot 10^{-4}$ . The second one,  
 1397 being near the DUT, was instead supposed to shield the sensor from the electrons which  
 1398 have passed the first one, except for a region of  $1 \text{ mm}^2$  configurable using *come si chiamano*  
 1399 *quei cacciavitini per settare la posizione?*.

## 1400 7.2 Measurements

1401 Because of the dead time of TJ-Monopix1 it is not possible resolving the bunch sub-  
 1402 structure and almost no one pixel can read more than a hit per bunch. I recall, indeed,  
 1403 that the dead time per pixel depends on the location on the priority chain for the readout  
 1404 and for each pixel  $\lesssim 1 \mu\text{s}$  (fig. 7.7) are needed; therefore only a few pixels at the top of  
 1405 the priority chain (at the upper left of the matrix) can fire a second time, since they in  
 1406 principle can be read the first time before the end of the pulse (assuming a pulse duration  
 1407 in  $2 \mu\text{s}-4 \mu\text{s}$ ) and then can be hit again.

1408 Since resolving the single electron track is impossible, a way this sensor could be used

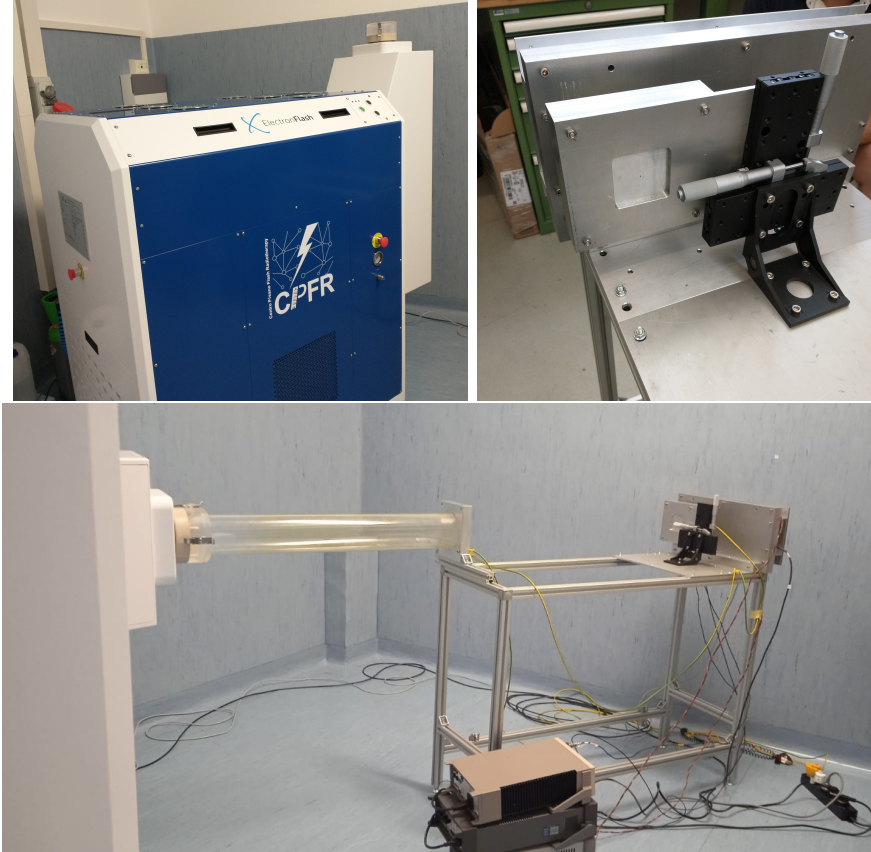


Figure 7.3: Experimental set up. (a) Electron flash accelerator: gantry rotante che consente un orientamento del fascio da 0° 90° (orizzontale / verticale) in tempo reale monitorato da un inclinometro integrato. the gun can be rotated from 90° to 0° (vertical/orizontal). (b) Collimator and DUT box. (c) Whole structure: we used the 10 cm diameter and 1.2 m long triode; the DUT which is in the box behind the two collimators is connected to the power supply units.

in such context is reducing its efficiency and taking advantage of the analog pile up and of the linearity of the analog output (ToT), in order to see a signal produced not by the single particle but by more electrons. Reducing the efficiency and the sensibility of the sensor is essential in order to decrease the high charge signal produced in the epitaxial layer: if the sensor is completely depleted the collection efficiency is closer to 1% and if the whole charges produced by a MIP,  $80 \text{ e}^-/\mu\text{m}$  about, are collected, the saturation limit is soon reach. Then a condition where there is a partial recombination of the center electron-hole created in the bulk is desiderable. On the other hand, the smaller the output signal value and the higher the rate the detector can cope with: indeed, the rollover constitutes a limit for the usage of the analog output. With the standard configuration of the FE parameters and the epitaxial layer completely depleted, a MIP produces a ToT out of range of representation of 6-bit; so as to obtain smaller output signals one can operate on the reduction of the gain of the preamplifier or on the pulse velocity of returnig to the baseline. Recalling the results in section 6.1.4, I have shown that concerning the PMOS flavor 1, reducing the bias from -6 V to 0 V brings a reduction of efficiency down to 40 %, and a reduction in the gain of a factor  $\sim 1/3$ , while the reduction of the gain of the preamplifier allows a reduction of **circa 10, ma da controllare**.

1426 In order to taking advantage of the analog pile up and integrating the charge, for  
 1427 semplicity assume of two electrons, the second one must hit the pixel before the ToT goes  
 1428 under the threshold. The general condition is then  $\overline{\Delta T} < \overline{ToT}$ , but if a high  $P_\mu(n \geq 1)$  is  
 1429 required, a lower  $\overline{\Delta T}$  may be desired:

$$P(n \geq 1) = \sum_{n=1}^{\infty} \frac{e^{-\mu} \mu^n}{n!} = 1 - P(0) = 1 - e^{-\mu} \quad (7.3)$$

1430

$$\mu = \frac{\overline{ToT}}{\overline{\Delta T}} \quad (7.4)$$

1431 If a  $P_\mu(n \geq 1) = 99\%$  then the  $\overline{\Delta T}$  must be  $\sim 0.22 \overline{ToT}$ . The ToT is in range [0,64] but  
 1432 since the rollover must be avoided, the  $\overline{ToT}$  must be lower than 32, and then the minimum  
 1433 rate on the pixel must be 1.25 MHz.

1434 During the testbeam many runs have been performed, spanning the energy, the dose  
 1435 per pulse and the four possible configurations with/without the collimators. We have used  
 1436 the PMOS flavor 1 in the standard configuration: we have biased the PWELL and PSUB  
 1437 at -6 V and set the standard default FE parameters reported in table ???. During all the  
 1438 acquisitions we have used pulses with  $t_p$  of 4  $\mu\text{m}$  and with the smallest PRF settable, which  
 1439 is 1 Hz, in order to start in the most conservative working point exluding the digital pile  
 1440 up of events from different bunch: even if the whole matrix turns on and there are 25000  
 1441 hits, the total readout time corresponding to 25 ms is still lower than the time between two  
 1442 consecutive pulses. The readout starts with the trailing edge of the first pulse going down  
 1443 the threshold,  $\sim 50$  clk = 1.25  $\mu\text{s}$  after this moment the FREEZE signal is sent to the whole  
 1444 matrix, and the trasmittion of the data to the EoC begins. The hits read are the ones  
 1445 whose TE occurred during the 50 clk counts; the ones, instead, whose TE occur during the  
 1446 FREEZE are stored in the pixel memory and read during a second readout. Obviously  
 1447 since the readout of the fist sub-pulse finishes much later than the bunch ends up, each  
 1448 pixel can be store only one hit. An example of the two sub-pulses is shown in figure ???:  
 1449 in the acquisition we injected 5 pulses with both the collimators mounted on the table.  
 1450 Looking at the spectrum **si vede che lo spettro del secondo pulse ha una coda più lunga a  
 1451 destra: questo è dovuto al fatto che le hit con tot lungo hanno il TE che cade durante il  
 1452 FREEZE e quindi vengono lette durante il secondo impulso.** On the other hand the 2D  
 1453 histograms, being uniform and not showing disomogenities, suggest that the collimators  
 1454 do not shield all the particles: this was due to a photon background higher than expected.  
 1455 When we have put aside the collimators, instead, the fluence was too high that **the whole  
 1456 matrix turns on in 50 clk counts; then the 2 pulses substructure no more appears (fig. 7.6).**  
 1457 **CONTROLLA PERCHÈ PORTEBBE ESSERE UNA CAZZATA**

1458 After the testbeam a simulation of the emission of electrons from the accelerator and  
 1459 their path across the triode and the collimators has been developed via Geant-4 **come si  
 1460 ringrazia il lavoro di qualcuno in maniera formale?**. The high background we saw although  
 1461 the collimators were mainly produced by electrons Bremsstrahlung during the transition  
 1462 through the alluminium collimators. **dalla simulazione si è visto che nessun elettrone  
 1463 arriva sul chip quando ci sono montati i collimatori, mentre nel caso senza collimatori gli  
 1464 eventi sono sostanzialmente tutti elettronni (frazione di fotoni prodotti in aria è?).** The  
 1465 photons' simulated spectrum in the three configurations are shown in figure ???. **confronto  
 1466 con quello che vedo nello spettro sopra: dati.**

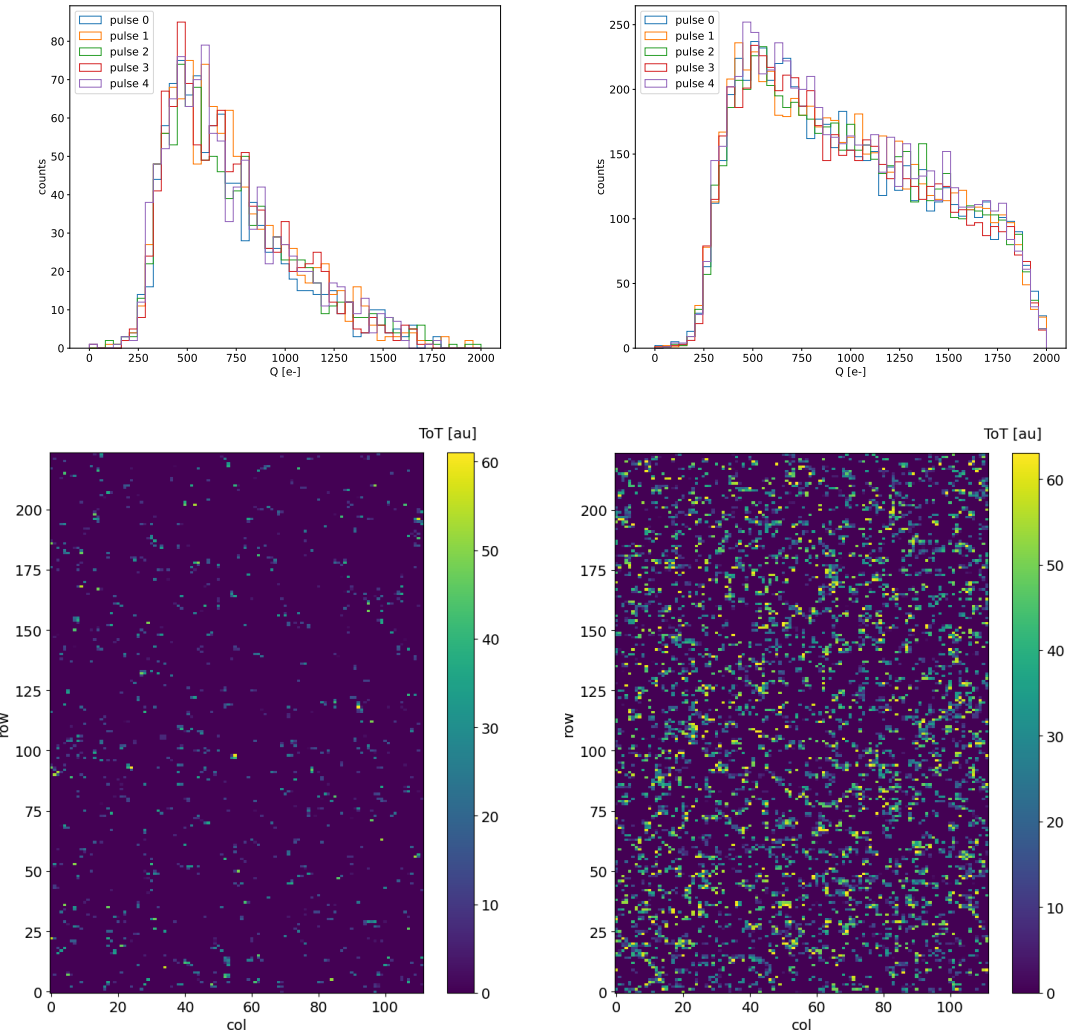


Figure 7.4: Acquisition with both the collimators: 5 pulses at  $DDP=0.07$  Gy. (a) Spectrum of the charge released in the sensor: to apply the conversion I used the information found in the previous chapter. (b) 2D histogram of the ToT of the hits arrived in the sub-pulses.

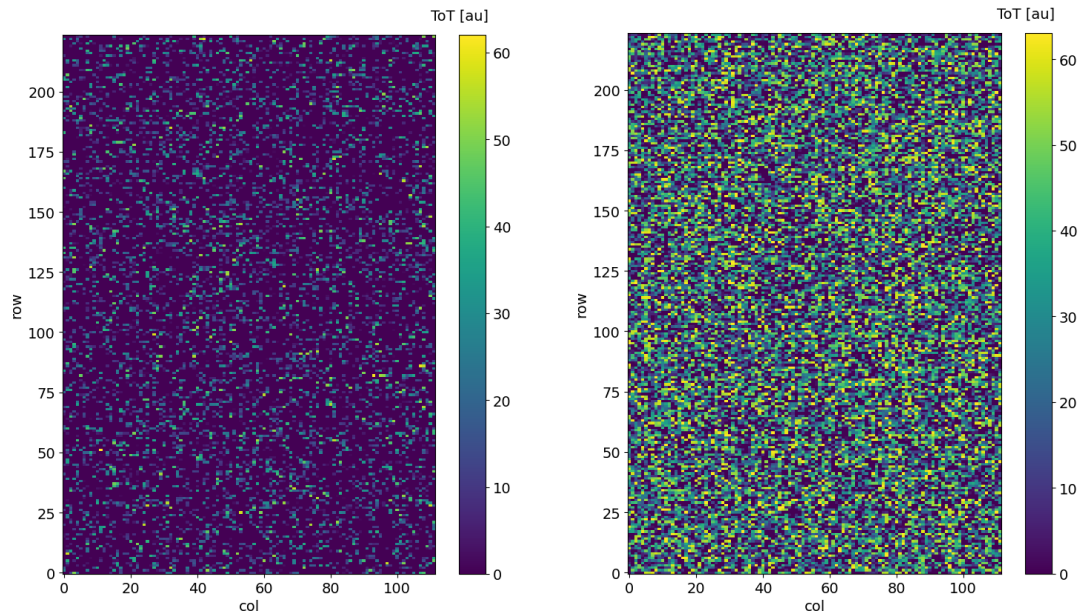


Figure 7.5: Acquisition with both the collimators: 5 pulses at DDP=0.6 Gy. 2D histogram of the ToT of the hits arrived in the sub-pulses. Compared with the previous maps, since the DDP is much higher, more pixels turn on.

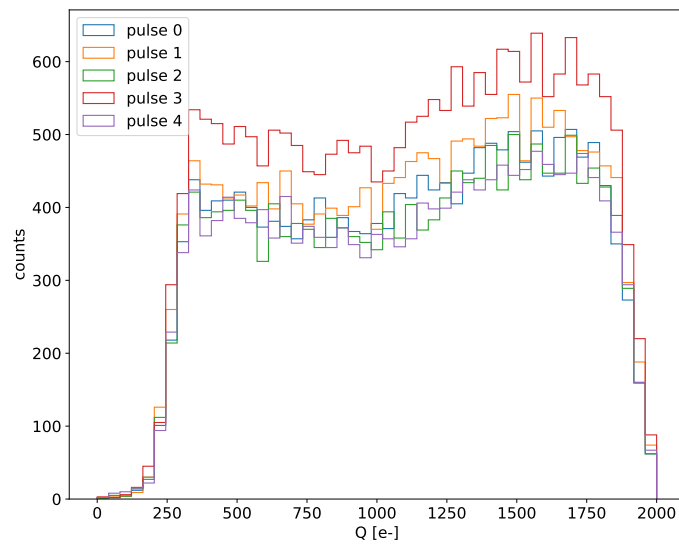


Figure 7.6: Acquisition without any collimator: 5 pulses at DDP=0.04 Gy.

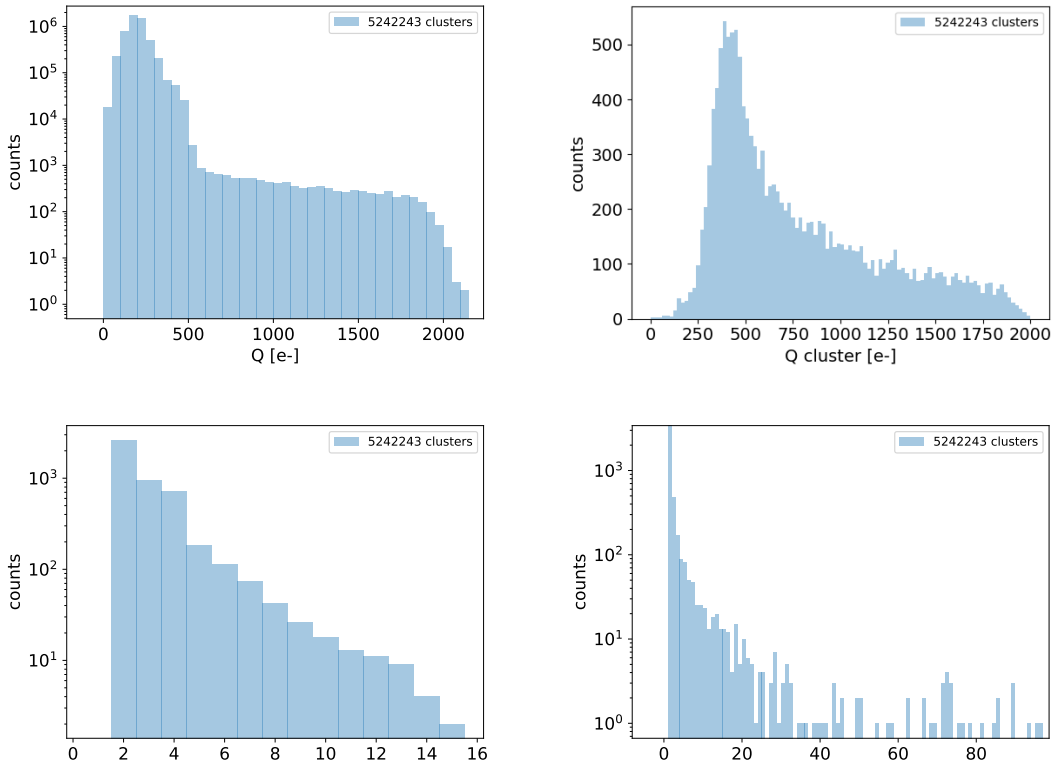


Figure 7.7: plot dei raggi cosmici da rigenerare

- 1468 • plot n di eventi che vedo con le diverse configurazioni
- 1469 • simulazione surya
- 1470 • confronta con misure dello spettro che vediamo senza e con collimatori.

### 1471 7.2.1 MIP spectrum using cosmic rays as source

1472 Since a MIP should produce about  $2\text{ ke-}$  in the epitaxial layer, it should provide a signal  
 1473 that in our conditions (full depletion and high gain) rolls over: in this situation making  
 1474 prediction on the spectrum expected for MIPs becomes hard. Therefore, in order to  
 1475 compare the spectrum observed at the testbeam with one certainly produced by MIP I  
 1476 have made some acquisitions without any radioactive source, in order to look at the cosmic  
 1477 ray events. To be confident with having selected MIPs from cosmic rays and cut the noise, I  
 1478 have selected only the events with multiple hits: these events are mainly clusters produced  
 1479 by the same impinging particle since the random coincidence probability is very low. In  
 1480 fact the cosmic rays and noise rates on the whole matrix are respectively  $0.02\text{ Hz}$  and  
 1481  $\sim\text{Hz}$ , the dead time in such a low occupancy condition can be always approximated with  
 1482  $1\text{ }\mu\text{m}$  (this is not completely true for multiple hits events for which the priority chain  
 1483 should be considered), the random coincidence rate is  $10^{-8}\text{ Hz}$ . Come mai lo spettro in  
 1484 lab è diverso da quello visto con gli elettroni da 9 MeV al santa chiara? Chiedi a Surya il  
 1485 rate visto sul detector senza collimatori.

1486 **Appendix A**

1487 **Pixels detector: a brief overview**

1488 **A.1 Radiation damages**

1489 Radiation hardness is a fundamental requirement for pixels detector especially in HEP  
1490 since they are almost always installed near the interaction point where there is a high  
1491 energy level of radiation. At LHC the  $\phi_{eq}$  per year in the innermost pixel detector is  
1492  $10^{14} n_{eq}/cm^2$ ; this number reduces by an order passing to the outer tracker layer [2] pag  
1493 341 Wermes. Here the high fluence of particles can cause a damage both in the substrate  
1494 of the detector and in the superficial electronics.

1495 The first one has a principal non ionizing nature, due to a non ionizing energy loss  
1496 (NIEL), but it is related with the dislocation of the lattice caused by the collision with  
1497 nuclei; by this fact the NIEL hypothesis states that the substrate damage is normalized to  
1498 the damage caused by 1 MeV neutrons. Differently, surface damages are principally due  
1499 to ionizing energy loss.

1500 **DUE PAROLE IN PIÙ SUL SURFACE DAMAGE** A charge accumulation in oxide  
1501 ( $SiO_2$ ) can cause the generation of parasitic current with an obvious increase of the 1/f  
1502 noise. Surface damages are mostly less relevant than the previous one, since with the de-  
1503 velopment of microelectronics and with the miniaturization of components (in electronic  
1504 industry 6-7 nm transistors are already used, while for MAPS the dimensions of compo-  
1505 nents is around 180 nm) the quantity of oxide in circuit is reduced.

1506 Let's spend instead two more other words on the more-relevant substrate damages:  
1507 the general result of high radiation level is the creation of new energy levels within the  
1508 silicon band gap and depending on their energy-location their effect can be different, as  
1509 described in the Shockley-Read-Hall (SRH) statistical model. The three main consequence  
1510 of radiation damages are the changing of the effect doping concentration, the leakage  
1511 current and the increasing of trapping probability.

1512 **Changing of the effective doping concentration:** is associated with the cre-  
1513 ation/removal of donors and acceptors center which trap respectively electrons/holes from  
1514 the conduction band and cause a change in effective space charge density. Even an in-  
1515 version (p-type becomes n-type<sup>1</sup>) can happen: indeed it is quite common at not too high  
1516 fluences ( $\phi_{eq} 10^{12-13} n_{eq} cm^{-2}$ ). A changing in the doping concentration requires an adjust-  
1517 ment of the biasing of the sensor during its lifetime (eq.2.2) and sometimes can be difficult  
1518 keeping to fully deplete the bulk.

1519 **Leakage current:** is associated with the generation-recombination centers. It has

---

1L'INVERSIONE OPPOSTA NON CE L'HAI PERCHÈ?

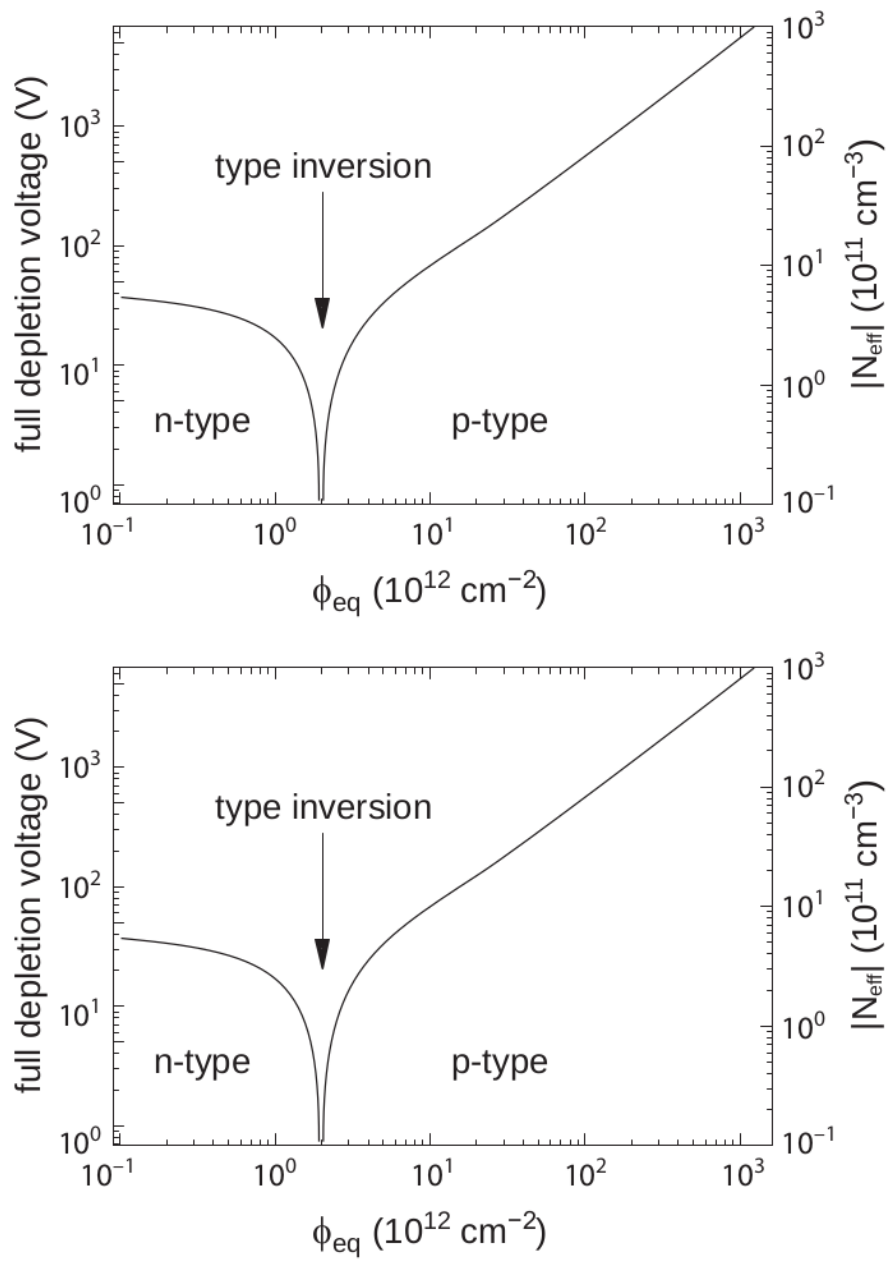


Figure A.1: 1b

1520 a strong dependence with the temperature ( $I_{leak} \propto T^2$ ), whose solution is therefore to  
1521 operate at lower temperature.

1522 **Increase of trapping probability:** since the trapping probability is constant in the  
1523 depleted region, the collected charge decreases exponentially with the drift path. The  
1524 exponential coefficient, that is the mean trapping path, decreases after irradiation and  
1525 typical values are 125-250  $\mu m$  and must be compared with the thickness of the depleted  
1526 region which () corresponds to the mean drift path.

1527 Different choices for substrate resistivity, for junctions type and for detector design are  
1528 typically made to fight radiation issues. Some material with high oxygen concentration  
1529 (as crystal produced using Czochralki (Cz) or float-zone (Fz) process (**CONTROLLA**  
1530 **LA DIFFERENZA TRA I DUE**)) for example, show a compensation effect for radiation  
1531 damage; another example is the usage of n+ -in-p/n sensors (even if p+ -in-n sensors are  
1532 easier and cheaper to obtain) to get advantage of inversion/to have not the inversion (since  
1533 they are already p-type). After inversion the n+p boundary, coming from n+ in-n, but to  
1534 keep using the sensor the depletion zone still must be placed near the diode.

1535 Single Event Upset, in sostanza è quando un bit ti cambia valore (da 0 a 1 o viceversa)  
1536 perché una particella deposita carica nell'elettronica che fa da memoria registro/RAM/....  
1537 Questo tipo di elettronica ha bisogno di un sacco di carica prima che il bit si "fippi"  
1538 (cambi valore), infatti tipicamente per avere un SEU non basta una MIP che attraversa  
1539 esattamente quel pezzo di chip in cui è implementata la memoria, ma un adrone che faccia  
1540 interazione nucleare producendo più carica di quanto farebbe una MIP. Questo metodo pur  
1541 essendo più comodo richiede less amount of area ha però come drawback che il registro può  
1542 essere soggetto a SEU problema non trascurabile in acceleratori come HL-LHC adronici

1543

# Bibliography

- 1544 [1] W. Snoeys et al. “A process modification for CMOS monolithic active pixel sensors  
1545 for enhanced depletion, timing performance and radiation tolerance”. In: (2017).  
1546 DOI: <https://doi.org/10.1016/j.nima.2017.07.046>.
- 1547 [2] H. Kolanoski and N. Wermes. *Particle Detectors: Fundamentals and Applications*.  
1548 OXFORD University Press, 2020. ISBN: 9780198520115.
- 1549 [3] E. Mandelli. “Digital Column Readout Architecture for 10.1109/NSSMIC.2009.5402399  
1550 the ATLAS Pixel 0.25 um Front End IC”. In: (2002).
- 1551 [4] M. Garcia-Sciveres and N. Wermes. “A review of advances in pixel detectors for  
1552 experiments with high rate and radiation”. In: (2018). DOI: <https://doi.org/10.1088/1361-6633/aab064>.
- 1554 [5] C. Marinas. “The Belle-II DEPFET pixel detector: A step forward in vertexing in the  
1555 superKEKB flavour factory”. In: (2011). DOI: [doi:10.1016/j.nima.2010.12.116](https://doi.org/10.1016/j.nima.2010.12.116).
- 1556 [6] J. Baudot. “First Test Results Of MIMOSA-26, A Fast CMOS Sensor With Inte-  
1557 grated Zero Suppression And Digitized Output”. In: (2010). DOI: [doi:10.1109/NSSMIC.2009.5402399](https://doi.org/10.1109/NSSMIC.2009.5402399).
- 1559 [7] A. Dorokhov. “High resistivity CMOS pixel sensors and their application to the  
1560 STAR PXL detector”. In: (2011). DOI: [doi:10.1016/j.nima.2010.12.112](https://doi.org/10.1016/j.nima.2010.12.112).
- 1561 [8] Giacomo Contin. “The STAR MAPS-based PiXeL detector”. In: (2018). DOI: <https://doi.org/10.1016/j.nima.2018.03.003>.
- 1563 [9] Nolan Espplen. “Physics and biology of ultrahigh dose-rate (FLASH) radiotherapy:  
1564 a topical review”. In: (2020). DOI: <https://doi.org/10.1088/1361-6560/abaa28>.
- 1565 [10] Fabio Di Martino et al. “FLASH Radiotherapy With Electrons: Issues Related to  
1566 the Production, Monitoring, and Dosimetric Characterization of the Beam”. In:  
1567 *Frontiers in Physics* 8 (2020). ISSN: 2296-424X. DOI: [10.3389/fphy.2020.570697](https://doi.org/10.3389/fphy.2020.570697).  
1568 URL: <https://www.frontiersin.org/articles/10.3389/fphy.2020.570697>.
- 1569 [11] M. Dyndal et al. “Mini-MALTA: Radiation hard pixel designs for small-electrode  
1570 monolithic CMOS sensors for the High Luminosity LHC”. In: (2019). DOI: <https://doi.org/10.1088/1748-0221/15/02/p02005>.
- 1572 [12] M. Barbero. “Radiation hard DMAPS pixel sensors in 150 nm CMOS technology  
1573 for operation at LHC”. In: (2020). DOI: <https://doi.org/10.1088/1748-0221/15/05/p05013>.
- 1575 [13] K. Moustakas et al. “CMOS Monolithic Pixel Sensors based on the Column-Drain  
1576 Architecture for the HL-LHC Upgrade”. In: (2018). DOI: <https://doi.org/10.1016/j.nima.2018.09.100>.

- 1578 [14] I. Caicedo et al. “The Monopix chips: depleted monolithic active pixel sensors with  
1579 a column-drain read-out architecture for the ATLAS Inner Tracker upgrade”. In:  
1580 (2019). DOI: <https://doi.org/10.1088/1748-0221/14/06/C06006>.
- 1581 [15] D. Kim et al. “Front end optimization for the monolithic active pixel sensor of the  
1582 ALICE Inner Tracking System upgrade”. In: *JINST* (2016). DOI: doi:10.1088/  
1583 1748-0221/11/02/C02042.
- 1584 [16] L. Pancheri et al. “A 110 nm CMOS process for fully-depleted pixel sensors”. In:  
1585 (2019). DOI: <https://doi.org/10.1088/1748-0221/14/06/c06016>.
- 1586 [17] L. Pancheri et al. “Fully Depleted MAPS in 110-nm CMOS Process With 100–300-  
1587 um Active Substrate”. In: (2020). DOI: 10.1109/TED.2020.2985639.